Alma Mater Studiorum · University of Bologna

Department of Physics and Astronomy
Master Degree Programme in Astrophysics and Cosmology

Numerical relativity simulations of compact binaries composed of a black hole and a neutron star

Master's thesis

Submitted by:
Francesco Brandoli

Supervisor:
Prof. Carlo Nipoti
Co-supervisors:
Prof. Sebastiano Bernuzzi
M.Sc. Alejandra Gonzalez

IV Session
Academic year 2022/2023

For Ilaria,
from Francesco who always sat
beside her.

Contents

Abstract

In this master thesis we conducted extensive simulations in the framework of numerical relativity, involving black hole-neutron star binary systems and investigating the parameter space for different mass-ratio's and spin's configurations.

While existing data predominantly involve binary black holes or binary neutron stars, the analysis of hybrid systems, observed tentatively and acknowledged to exist, remains incomplete. Mixed binary systems represent compelling candidates for the study of ultra-dense matter, offering valuable insights into constraining the equation of state for neutron stars which are today not exactly known. Additionally, they are also expected to produce highly relativistic dynamical ejecta, that can produce heavy elements via rapid neutron capture and whose exact origin is still today a matter of debate. Of particular interest is the potential for kilonovae events, arising from the radioactive decay of the aforementioned heavy nuclei. This subsequent electromagnetic emission positions black hole-neutron star binaries as promising candidates for multimessenger astronomy observations.

We started by producing initial data employing the `Elliptica` code (Rashti et al., 2022). The data produced in this phase are characterized by irrotational neutron stars, with fixed mass and equation of state. The effects of different mass-ratios and spins are included in the configuration of the black holes, which we simulated with three different values both for mass and spin. The initial data are systematically compared to the effective-one-body model `TEOBResumS` (Nagar et al., 2018), and to post-Newtonian models, constructing quasi-equilibrium sequences to analyze tidal and spin-orbit effects that can influence the dynamical evolution. Subsequently, nonspinning initial data are evolved using the `BAM` code (Brügmann et al., 2004) with a specific focus on the finite mass-ratios effects and their impact on the dynamics of the system. An in-depth analysis of the accuracy of the data is then performed, focused on gravitational waveforms, merger remnant, and dynamical ejecta.

1 Introduction

The physics behind compact binary coalescence is one of today's most interesting and multidisciplinary fields of research. This general relativistic framework can in fact cover diverse topics such as hydrodynamics, magnetic field physics, micro-physics, gravitational waves physics, numerical relativity as well as many others. To point out which are the most important things to present our results, it is therefore crucial to select carefully the information for the reader. Consequently, the thesis is organized into five main chapters. Chapter 1 introduces the main concepts behind black hole-neutron star binaries, analyzing the available results from the literature and providing an overview of those parameters that regulate the subsequent evolution. In Chapter 2 we recall the main equations and formalism behind gravitational waves' physics including post-Newtonian theories and effective-one body models. It also delves into the main concepts related to the theory of black holes (BHs) and neutron stars (NSs). Chapters 3 and 4 provide an insight into the numerical relativity framework and introduce the numerical methods used during the project. Finally, in Chapter 5, we articulate and discuss our obtained results.

1.1 Why are we interested in the black hole–neutron star binary merger?

Starting from the last decade, the research for compact binary coalescence has completely changed, rapidly becoming a fertile ground for different kinds of studies. Starting from the gravitational-wave (GW) event GW150914 detected by LIGO and Virgo Collaboration (Abbott et al., 2016a), strong evidence for the existence of black hole binary (BBH) mergers within the Hubble time were gathered, producing results consistent with the scenario predicted by General Relativity (GR), e.g. (Abbott et al., 2016b) and (Yunes et al., 2016). After that, the first binary-neutron-star (BNS) merger GW170817 was detected, not only via GW observations (Abbott et al., 2017a) but also exploiting multiband electromagnetic (EM) signals (Abbott et al., 2017c). These astrophysical phenomena are today considered as one of the most likely sources of short gamma-ray-burst (Abbott et al., 2017c), as well as a possible site of r-process nucleosynthesis (Watson et al., 2019) discoveries that open the way for a new era of multimessenger astronomy with gravitational and EM signals. This kind of observation allowed the possibility of using GW170817 as a standard siren (Abbott et al., 2017b) to measure for the first time the Hubble constant using gravitational signatures.

More recently (January 2020), the LIGO-Virgo detector network observed the first GW signals consistent with black hole-neutron star (BHNS) binaries (GW200105 and GW200115 reported in (Abbott et al., 2021)). The rate at which these mergers occur is currently inferred to be around $7.8 - 140$ $\mathrm{Gpc}^{-3}\mathrm{yr}^{-1}$, largely consistent with the available theoretical estimations (Santoliquido et al., 2021), positioning BHNS between BNS,

whose merger rate is 10-1700 $\mathrm{Gpc}^{-3}\mathrm{yr}^{-1}$, and BBH with 17.9-44 $\mathrm{Gpc}^{-3}\mathrm{yr}^{-1}$ (Abbott et al., 2023). Given the commonly large mass ratio (defined as $Q = M_{BH}/M_{NS}$, and as high as 4-5) and the weak BH spin (likely to be zero or retrograde), these systems are typically not expected to produce a bright EM radiation, hence, the lack of detection for this kind of signal should not come as a surprise. In fact, being tidal disruption unlikely to happen in this region of the parameter space, mass ejection and its associated EM emission are not expected to occur in most of the cases. However, for both of these detections, it was possible to constrain the orbiting masses using the information contained in the GW signal alone to $8.9^{+1.2}_{-1.5}M_\odot$ and $1.9^{+0.3}_{-0.2}M_\odot$ for GW200105 and to $5.7^{+1.8}_{-2.1}M_\odot$ and $1.5^{+0.7}_{-0.3}M_\odot$ for GW200115 at the 90% credible level for the BHs' and NSs' masses, respectively. This happens to be a crucial point since, in the absence of an EM counterpart, the classification of these systems as BHNS binary is purely based on the expected mass of the two bodies, labeling as NS those objects with a mass smaller than the theoretical upper limit of $3M_\odot$.

The merging scenarios are today widely studied by means of numerical relativity (NR) simulations whose outputs seem to point to the existence of two main scenarios: the NS could be tidally disrupted before merging, or it could plunge directly into the BH (this time, without tidal disruption). Among these two kinds of mergers, the former are typically considered as the most valuable for physics and astrophysics, in particular the tidal disruption is required to happen at a sufficiently large distance from the BH's innermost stable circular orbit (ISCO) to produce the most interesting outcomes. As a matter of fact, in the case the NS is not disrupted, or the tidal disruption takes place in a region too close to the ISCO, it will have the very same behavior of a point-like particle throughout the coalescence, and the final merging will show no major differences with respect to a highly asymmetric BBH coalescence scenario with the only possible exception of EM emission related to crust shattering (Tsang et al., 2012), magnetospheric activities (Carrasco et al., 2021) or charged BHs (Zhang, 2019). Referring to the possibility of having the NS tidally disrupted, researchers have focused their efforts on three major aspects of this phenomenon:

- **Gravitational waves**. GWs can be used to infer finite-size properties of the NS including its equation of state (EOS). In particular, the tidal deformability Λ can be extracted from the phase evolution of the inspiral (Flanagan and Hinderer, 2008) together with masses and spins of the astrophysical objects (Poisson and Will, 1995). With these quantities is then possible to gather an estimate of the NS radius, a quantity strongly but not entirely connected to Λ (De et al., 2018), together with invaluable information on supra nuclear-density matter (Harada, 2001). It is therefore crucial to have a better understanding of the gravitational waveform and to develop a model able to reproduce those observable features connected to tidal disruption and to possible theoretical EOS.

- **The remnant**. The accretion disk formed by the disrupted NS material could

be a promising source of short-hard gamma-ray burst (Mochkovitch et al., 1993). The mechanism of production could be related to the neutrino pair annihilation process (Rees and Mészáros, 1992), in presence of a sufficiently hot and dense disk that could generate a so-called neutrino-dominated accretion flow. A different hypothesis for this engine to work is related to the rotational energy of a spinning BH extracted by magnetic fields (a process known as Blandford–Znajek mechanism (Blandford and Znajek, 1977)). An additional topic of investigation is today the possibility of successfully simulating the launch of ultrarelativistic jets starting from the merger remnant.

- **Ejecta**. The merger of BHNS binaries is shown to produce tidal mass ejection with parameters dependent on the mass ratio, the BH's spin, and the NS's EOS. In particular we expect to have a more energetic and massive ejection in the case of smaller mass ratios, larger BH's spin, and stiffer EOS[1]. During the merger, a large amount of neutron-rich matter will be ejected and will synthesize, via rapid neutron capture, elements heavier the iron. This source of metals is of primary importance being their galactic abundances still today not completely understood. Their subsequent radioactive decay will heat up the ejecta producing a quasithermal emission in the UV-optical-IR bands called kilonova and it is today considered as the most promising EM counterpart to GWs. These ejecta are then interacting with the surrounding interstellar medium (ISM), contributing to the chemical evolution of galaxies and producing a subsequent synchrotron radiation. This second part of their life is very similar to the one found in supernova remnants: the ejecta expand freely, then start to blend with the ISM and to decelerate when their mass is compatible with the one of the entangled ISM entering the Sedov-Taylor phase. However, the evolution of this remnant is significantly shorter than the one found in supernovae due to their smaller masses and higher velocities. Since the particles are accelerated in a strongly magnetized medium, the presence of relativistic electrons will generate a synchrotron emission in the radio band and can also emit X and γ rays in the framework of a synchrotron self-Compton model (Takami et al., 2014). From the point of view of stellar astrophysics, this kind of ejecta could also be the origin of exceptionally r-process enhanced metalpoor stars, so-called actinide-boost stars (Mashonkina, L. et al., 2014).

The analysis of these points can be done today only by means of NR, which has the possibility to produce high-accuracy waveforms currently beyond the reach of approximated[2] analytical models. However, the computational costs associated with these simulations are extremely elevated, making NR by itself an inefficient way to proceed.

[1]EOS denoted as "stiff" characterize a kind of matter more difficult to compress. Conversely, "soft" EOS are associated with compact and massive NSs.

[2]See section 2.3.

Therefore the field has evolved to include numerical-relativity informed models, which rely on the information coming from these simulated data to produce accurate templates in a cost-effective way. The latter serve as invaluable tools for the gravitational waves community, enabling the analysis of detected waveforms by the LIGO-Virgo-KAGRA collaboration. The simulations generated in this project can be utilized within a broader framework for developing this kind of template.

1.2 Black hole-neutron star binaries

Just to provide a qualitative overview of the topic we are going to face, let me start by describing the evolution of these peculiar binary objects from their formation until their final merging. First of all, it is interesting to notice how the origin of these systems is still a matter of debate. For the time being, the most likely scenario is the one describing two massive stars, born in a binary, and sufficiently distant from one another to have a fully isolated evolution.[3] Nevertheless, many different formation channels can not be a priori ruled out, including dynamical interaction in globular cluster (Zwart and McMillan, 1999), population III stars mergers (Belczynski et al., 2017), formation in active galactic nuclei discs (O'Leary et al., 2009) or more exotic channels such as formation from primordial BHs (Capela et al., 2013) or mirror dark matter particles (Beradze et al., 2020). The typical mass ranges covered by our binary objects space between $1.2 - 1.6 M_\odot$ (Özel et al., 2012) for NSs while the BHs are considered to be as massive as $5 - 15 M_\odot$ (Özel et al., 2010) with poorly known spins magnitude and orientation. The binary system we can describe in this way is typically characterized by low level of eccentricity (Peters and Mathews, 1963) even though the existence of eccentric binaries can not be excluded and would have a profoundly different GW and EM observables in respect to the one described for circular binaries: this would be the case for dense stellar cluster where the NS could be dynamically attracted by the gravitational field of a BH, performing a few very eccentric orbits and eventually merge (East et al., 2012). It is interesting to point out the fact that the lifetime of BHNS binary in circular orbit scales like (Kyutoku et al., 2021)

$$t_{gw} \propto 1.01 \cdot 10^{10} \text{ yr} \left(\frac{r}{6 \times 10^6 \text{ km}} \right)^4 \tag{1}$$

for a given orbital separation r and assuming the adiabatic approximation (which is appropriate when the radiation reaction's time scale is much longer than the orbital period). A condition to a have BHNS binary merger within the Hubble time (needed to explain short-hard gamma-ray burst and r-process elements) is to have the initial

[3]Sometime this could include the temporary formation of a common envelope able to push the objects a little bit closer during the inspiral (Smarr and Blandford, 1976).

semimajor axis smaller[4] then 10^7 km. One important remark regarding long-term evolution is that orbital eccentricity decreases rapidly as a function of the semimajor axis a in an asymptotically circular regime thanks to the emission of gravitational radiation, specifically (Peters, 1964)

$$a(e) \propto e^{12/19}/(1-e^2) \tag{2}$$

shows how the eccentricity tends to zero, reaching a circular configuration as the semimajor axis decreases. Consistently with that, BHNS binaries that start their inspiral in an eccentric regime may safely be approximated as circular right before the merger when the GWs are observed by ground-based detectors. The evolution of BHNS binary systems can be summarized into three main stages: a million-of-years long inspiral during which the objects lose their energy and angular momentum via GW emission; a millisecond-long merger phase that can result in NS tidal disruption or to its plunge into the BH; for those disrupted systems, see Fig. 1, a post-merger phase can also occur (lasting a few seconds) during which matter could be ejected or accreted onto the BH (Foucart, 2020).

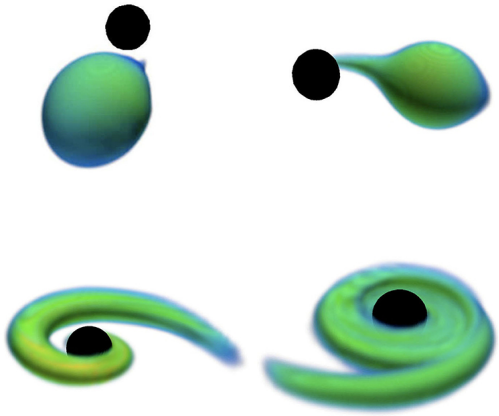

Figure 1: Evolution of a tidally disrupted BHNS binary. Onset of mass accretion (top left), unstable mass transfer (top right), evolution into a tidal tail (bottom left), circularization into an accretion disk (bottom right). Image from (Foucart, 2020).

An additional note on the NS, to guide the reader through some of the choices made during this project: detectable BHNS binaries are unlikely to host recycled pulsars, being the NS expected to lose its residual birth-spin long before entering the band of interest for ground-based gravitational wave observatories, via gravitational radiation from r-modes or magnetic braking (Staff et al., 2012). For this reason, it is a typical choice to consider the NS as nonspinning, with the only exception arising from the dynamical formation scenario in galactic centers or globular clusters (Ye et al., 2019) where NSs can be spun up in a process called "recycling", where matter is accreted from a donor star.

[4]The precise value depends on the masses of the two bodies and the initial eccentricity of the system.

1.3 The merger

An appropriate description of the merger provides an ensemble of processes including the NS tidal disruption, ejection of stellar material, and formation of a disk. During these phenomena, a significant role is played by the presence of magnetic fields and neutrino transport but only after the disrupted NS particles have formed a circularized disk. Therefore, the properties of the NS are only related to its EOS. As we saw, the separation between the two objects during the inspiral decreases with time, thanks to the dissipation of energy and angular momentum which happens via GW emission, a fundamental process that will be further described in the following chapter. In the previous section, we briefly discussed the possible ending points of BHNS systems: to understand which of those will happen, we have to study the location of the ISCO and the orbital separation associated with the NS's tidal disruption. The latter happens when a critical mass is subtracted from the NS's surface, but in order to properly describe it, it is mandatory to understand the position at which the BH's tidal force overcomes the NS's self-gravity at the inner edge of the stellar surface. We call the orbit at which this happens the **mass shedding limit**. This quantity, which is connected to the mass-ratio of the binary and to the radius of the NS, can be estimated by

$$r_{ms} = 2^{1/3} c_R \left(\frac{M_{BH}}{M_{NS}}\right)^{1/3} \cdot R_{NS} \tag{3}$$

where the factor $c_R > 1$ stands for the degree of tidal elongation of the NS's radius, and has values depending on the NS properties and the orbital separation. The exact location at which the tidal disruption will occur is connected to the NS EOS and to the speed at which the radius of the star expands following the mass loss. If this happens inside the ISCO, then matter is just rapidly captured by BH's gravitational field without the possibility to generate a remnant disk or to produce ejecta. Therefore, the observable astrophysical consequences are significantly more difficult to detect. The position of the ISCO is extremely dependent on how the BH is spinning: for instance, considering an orbit on the BH equatorial plane it is possible to estimate[5] (Bardeen et al., 1972)

$$r_{ISCO} = \hat{r}_{ISCO}(\chi) \frac{GM_{BH}}{c^2} \tag{4}$$

with $\hat{r}_{ISCO}(\chi)$ being a decreasing function of the dimensionless spin parameter of the BH χ. This is connected to the so-called spin-orbit interaction, in particular for a retrograde orbit ($\chi = -1$) we have a value of $\hat{r}_{ISCO} = 9$, for a nonspinning BH $\hat{r}_{ISCO} = 6$ and for a prograde orbit ($\chi = +1$), $\hat{r}_{ISCO} = 1$. A representation of this effect is visible in Fig. 2.

In case the BH's spin is not aligned with the orbital angular momentum, the spin-orbit interactions are determined only by the component parallel to the orbital angular

[5]Being the considered BH spinning, Eq. (4) is formally derived describing the motion of a particle inside a Kerr geometry, see section 2.2.3.

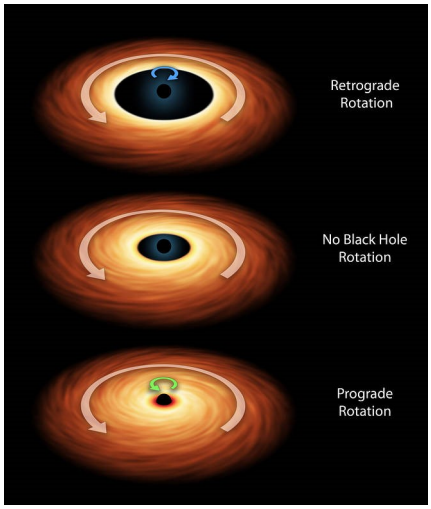

Figure 2: Different location of the ISCO as function of the BH's rotation. Image from: NASA/JPL-Caltech.

momentum. Since we lose a direct dependence on the spin magnitude, the effects of a rapidly spinning BH could be negligible in this condition. Taking the ratio of Eqs. (3) and (4) we can obtain an estimate of the condition for which an observable tidal disruption occurs

$$\frac{r_{ms}}{r_{ISCO}} = 2^{1/3}\frac{c_R}{\hat{r}(\chi)_{ISCO}}\left(\frac{M_{BH}}{M_{NS}}\right)^{-2/3}\left(\frac{GM_{NS}}{c^2R_{NS}}\right)^{-1} > 1 \tag{5}$$

Suggesting that the probability for these events to occur will depend on the mass ratio being small ($M_{BH}/M_{NS} \ll 1$), the neutron star having small compactness ($\mathcal{C} := GM_{NS}/c^2R_{NS} \ll 1$), and the dimensionless BH's spin being large ($\chi \gg 0$).

To provide the reader with a graphical idea of this process, it is possible to have a look at Fig. 3 and 4, from (Kyutoku et al., 2021), representing the evolution of two BHNS systems. In Fig. 3 we can see the evolution of a system with $M_{BH} = 4.05M_\odot$, $\chi = 0$, $M_{NS} = 1.35M_\odot$, and $R_{NS} = 11.1$km ($Q = 3$, $\mathcal{C} = 0.180$) modeled by a piecewise-polytropic approximation of the APR4 EOS (Akmal et al., 1998). In this system the tidal disruption of the NS happens inside the ISCO: the production of dynamical ejecta and accretion disk is negligible ($M \ll 0.01M_\odot$) as most of the NS material falls directly onto the BH. In Fig. 4 we have the same binary system, this time with a spinning black hole with $\chi = 0.75$. The NS is here tidally disrupted outside the ISCO: this leads to the spreading of the NS particles around the BH and to the formation of a one-armed spiral structure in differential rotation called tidal tail (left middle panel). Since the outer parts of this tail are slowly moving around the BH, the tidal tail collides with itself (right middle panel), producing an axisymmetric disk surrounding the BH remnant.

During this phase the small one-arm structure still remains, slowly transporting angular momentum toward the outside: this sets the conditions for having mass accretion even if magnetohydrodynamical processes are still not efficient. Moreover, since the accretion time scale is considered to be significantly smaller than the rotational period, we assume the disk to be in a quasi-steady state on a time scale of 10 ms.

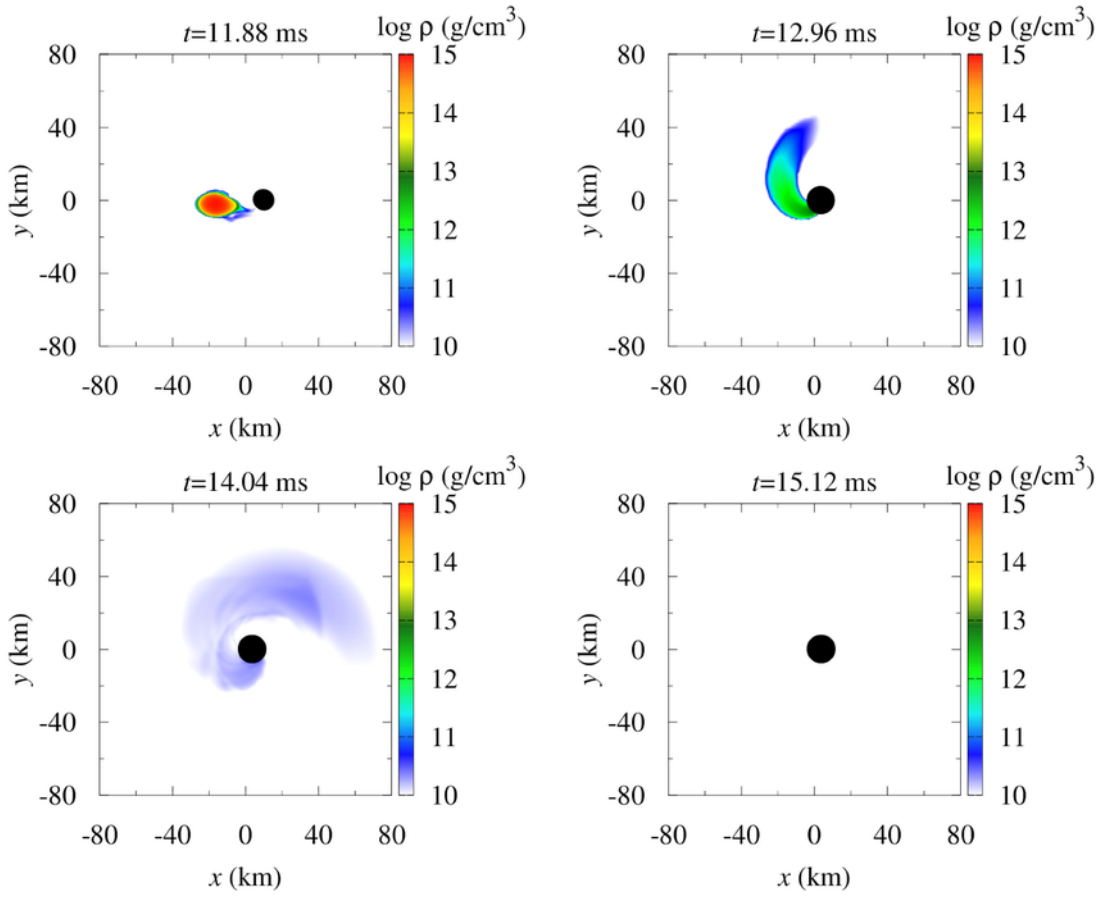

Figure 3: Example of the time evolution of the rest-mass density profile for a NS poorly tidally disrupted: the mass shedding limit is reached in an orbit too close to the BH. $M_{BH} = 4.05 M_\odot, \chi = 0, M_{NS} = 1.35 M_\odot$ and $R_{NS} = 11.1$km ($Q = 3$, $\mathcal{C} = 0.180$) modeled by a piecewise-polytropic approximation of the APR4 EOS. Image from: Kyutoku et al. (2021).

Eventually, the outermost particles of the tail obtain energy sufficient to leave the gravitational potential of the remnant leading to dynamical ejection. This process happens in two phases: initially the tidal torque increases their energy and the angular velocity and subsequently impulsive outward radial force (probably associated with the infall of a significant fraction of the NS onto the BH) pushes them further away. If

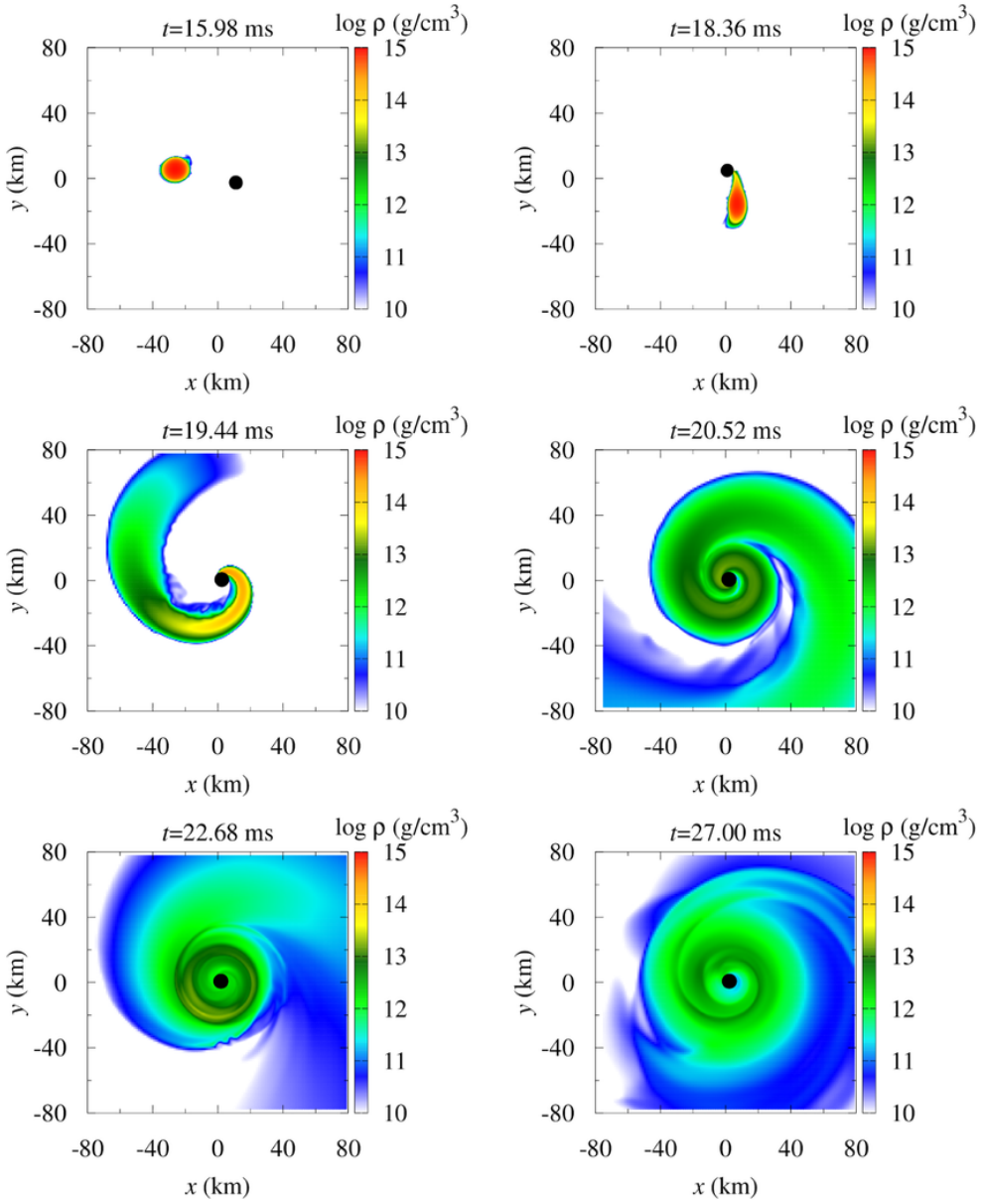

Figure 4: Example of the time evolution of the rest-mass density profile for a NS tidally disrupted outside the ISCO. $M_{BH} = 4.05M_{\odot}$, $\chi = 0.75$, $M_{NS} = 1.35M_{\odot}$ and $R_{NS} = 11.1$km ($Q = 3$, $\mathcal{C} = 0.180$) modeled by a piecewise-polytropic approximation of the APR4 EOS. Image from: Kyutoku et al. (2021).

the gravitational binding energy is won by the fluid particle's kinetic energy, then that element is free to escape the system. Some material in the middle and inner part of the disk can also acquire some energy, which is however insufficient for it to be expelled from

the system, and will eventually fall back on the disk.
The evolution described for tidal disruption outside the ISCO is qualitatively typical for binaries characterized by large NS' radii, small BH's masses, and small BH's spins; however, how this process occurs is directly dependent on some parameters of the binary and can be quantitatively different in each case.

1.4 Parameters of the binary

1.4.1 Equation of state

As discussed in section 1.3, the NS compactness $\mathcal{C}$ plays a fundamental role in terms of tidal disruption and is therefore connected to the final evolution of the BHNS system. This parameter is conveyed by the NS's EOS, which describes the density distribution and that can be exploited to determine a value for the NS's mass as function of its radius. With this in mind, it should not come as a surprise the fact that the gravitational waveform, the properties of the disk, and those of the dynamical ejecta happen to be controlled by this equation. However, formulating an equation able to describe supranuclear density matter (and so the structure of NSs) is still today one of modern physics' open issues. A possible solution for this issue comes from GW analysis: for this reason a vast variety of theoretical gravitational waveforms have been produced, performing simulations over the whole parameter space of BHNS binaries, considering as many different EOS as possible. As of today, a typical practice has become performing studies using piecewise-polytropic EOS where pressure and density are connected by a broken power-law in the form

$$P = \begin{cases} K_0 \rho_0^{\Gamma_0} & \text{if } \rho_0 \leq \rho_1 \\ K_1 \rho_0^{\Gamma_1} & \text{if } \rho_1 \leq \rho_0 \leq \rho_2 \\ \vdots & \\ K_{n-1} \rho_0^{\Gamma_{n-1}} & \text{if } \rho_{n-1} \leq \rho_0 \leq \rho_n \end{cases} \tag{6}$$

where Γ_i denotes a polytropic exponent and K_i a polytropic constant. During this project, we choose to explore the possibility offered by **ALF2** (Alford et al., 2005). This hybrid EOS is characterized by mixed APR nuclear matter (Akmal et al., 1998) and colour-flavor-locked quark matter, and it is sufficiently stiff to produce relevant dynamical ejecta. The NR simulations of BHNS systems have been focusing on nonspinning NSs, with masses within the typical values observed for our galaxy $M_{NS} \approx 1.2 - 1.5 M_\odot$. Consistently with that, a gravitational mass of $1.44 M_\odot$ was considered for this project associated with a baryon rest mass of $1.6 M_\odot$ (see section 4.1 for a further description of this parameter). For this choice, the NS radius is $R_{NS} = 12.40$km. Fig. 5 shows the mass vs radius plot for NSs with different EOS, together with a blue point representing our simulated NS. As for today, the maximal mass detected for massive pulsars

is accepted to be beyond $2M_{\odot}$, therefore NR simulations rarely adopt EOS incompatible with these objects. However, for the purpose of instructing a model, it can be useful to explore the parameter space properly, considering regimes not fully compatible with the observations as to uncover physical properties that may be hidden by the presence of parameter degeneracy. In Table 1 some peculiar quantities related to various EOS are reported from the website of the collaborative research group CORE (`http://www.computational-relativity.org`), including the maximum mass achievable for irrotational TOV model (see section 2.2.1) and the same value obtained for a body in rigid rotation, where slightly higher equilibrium masses can be reached. If we now consider two identical NSs with the same mass and compactness but with different EOS, it could be interesting to study how the density profile changes. What was found by Kyutoku et al. (2010) is that NSs with a more centrally condensed density profile are more easily subjected to tidal disruption, this relation is settled by the value of the adiabatic index Γ: a NS with a certain compactness will be more centrally condensed (and consequently less affected by tidal disruption) if the value of Γ in the core region is smaller.

1.4.2 Mass ratio

We briefly discussed how small mass ratios set the ideal conditions for having tidal disruption outside the ISCO. This statement happens to be particularly true in the case of nonspinning BHs, being more prone to have tidal disruption effects only in the case of low-mass ratios, while in the case of prograde spinning BHs, also more massive

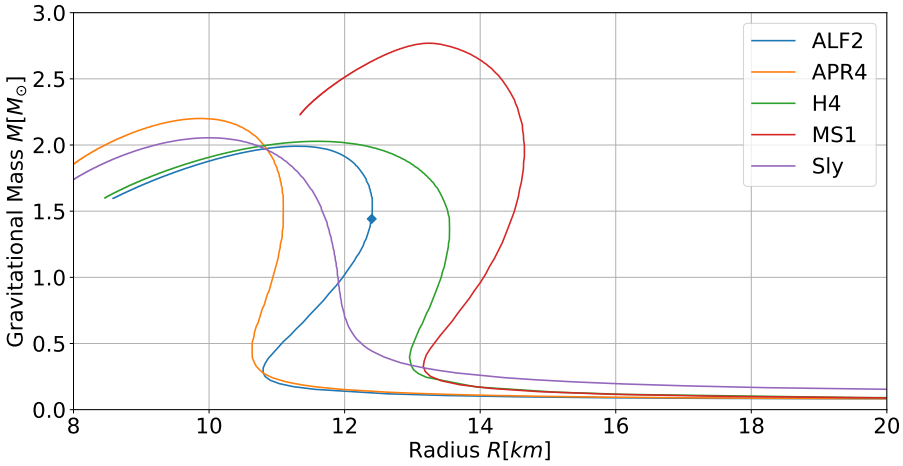

Figure 5: Mass-Radius sequences for different EOS. The blue point on top of the ALF2 curve represents the NS simulated in this project.

Name	M_{max} (TOV)	M_{max} (rr)	$M_{b,max}$(TOV)	$M_{b,max}$(rr)
2B	1.78	2.16	2.13	2.58
2H	2.83	3.46	3.41	4.14
ALF2	1.99	2.51	2.32	2.93
ENG	2.25	2.76	2.73	3.33
H4	2.03	2.48	2.33	2.85
MPA1	2.47	3.06	3.03	3.74
MS1	2.77	3.43	3.35	4.13
MS1b	2.76	3.44	3.35	4.16
SLy	2.06	2.51	2.46	2.98

Table 1: Maximum masses available for different EOS. The notation $M_{b,max}$ refers to the maximum baryonic mass. The notation (rr) refers to values estimated for objects in rigid rotation. All the masses reported here are shown in unit of $M_{\odot}$. Data from Read et al. (2009).

objects and so larger mass ratios could lead to tidal disruption. It is therefore possible to investigate more deeply what will happen for different initial masses, starting by providing a way to find the critical mass ratio Q_c that defines which BHNS binaries will encounter the ISCO before reaching the mass-shedding limit as a function of the NS's compactness, (Kyutoku et al., 2021)

$$0.270\mathcal{C}^{3/2}(1+Q_c)\left(1+\frac{1}{Q_c}\right)^{1/2} = 0.0680\left[1-\frac{0.444}{Q_c^{0.25}}\left(1-3.54\mathcal{C}^{1/3}\right)\right] \tag{7}$$

For a given value of $\mathcal{C}$, Eq. (7) provides a way to identify Q_c. In this way, if a given BHNS binary has a mass ratio $Q > Q_c$, the NS will plunge onto the BH, thus avoiding tidal disruption. As mentioned, this critical mass ratio is strongly related to the BH spin's value: for high, prograde, and spin-aligned BHs, the region in which the mass shedding limit can be reached is significantly enlarged, being the location of the ISCO much closer to the singularity. NR simulations have covered in the last ten years the range $1 < Q < 8.3$. Large mass ratios are today considered as the most realistic BHNS system, with observed stellar-mass BH with typical masses $M_{BH} \geq 5 - 7M_{\odot}$, while low mass ratios are now studied with a renewed interest after the discovery of BNS gravitational waves. The reasons for that are manifold: first, BHNS with low mass ratio could be very similar to BNS making GWs sources ambiguous; second being able to discriminate between very-low mass BHNS binary and BNSs could be a crucial step in determining the maximum mass for NSs, the mass gap between BHs and NSs and further detail on the formation mechanism of compact objects.

1.4.3 Black hole spin

The BH's spin has probably all the rights to be considered the most significant parameter in this description, since it has the ability to modify the orbital evolution in the late inspiral together with the properties of the merger. Since during this project we only considered spin-aligned orbits, the majority of this discussion will be focused on its features. Let's consider a system characterized by common parameters, with the only exception of the BH's spin. As seen in Fig. 6 the systems with different spin ($\chi = 0$ on the left panel and $\chi = 0.6$ on the right panel) have different coalescence times. This difference can be imputed to the possibility of having spin-orbit interaction which behaves as a repulsive force for prograde spins and as an attractive force for retrograde spin. In this way, the gravitational pull between the two bodies is partially compensated, leading to a reduction of the orbital angular velocity and to a longer quasi-circular inspiral.

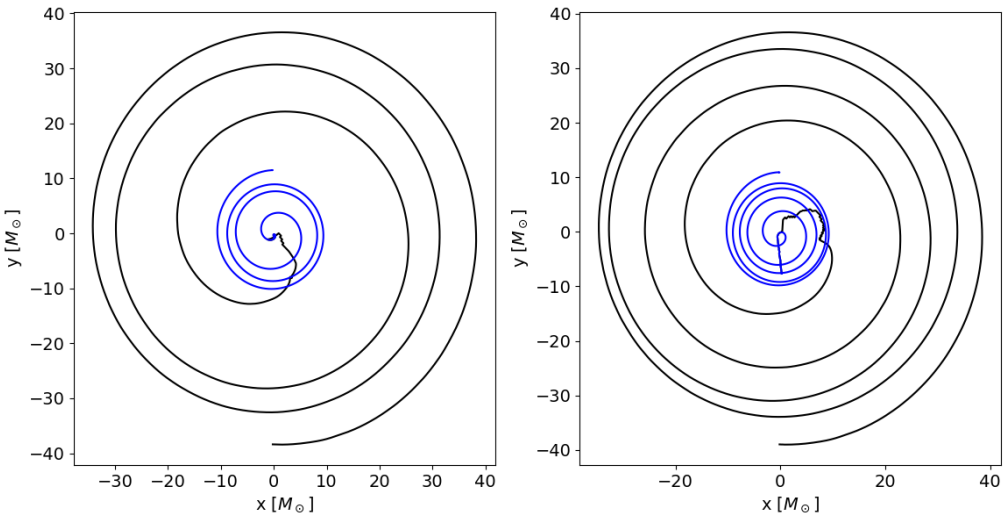

Figure 6: Orbit trajectory of the BH (blue line) and the NS (black line). The parameters used to create this plot are $Q = 3$, $\mathcal{C}$=0.17 modeled by the ALF2 EOS. The spin values are respectively $\chi = 0$ (left panel) and $\chi = 0.6$ (right panel). Plot produced using data from `BAM`.

We already mentioned how the location of the ISCO is connected to the value of BH's spin: the spin-orbit repulsion can move its location toward the innermost region of the BH gravitational field, increasing therefore the merging time of a BHNS binary with a positive spin and requiring the emission of a significant amount of energy to reach it. All of these effects, lead to the increasing number of orbits visible in Fig. 6. The probability of a NS being disrupted is therefore significantly higher in the case of prograde BH's spin. This can affect some properties of the dynamics of the merging, leading to the formation

of more massive disks and ejecta.[6] Going back to Fig. 3 and 4 it is possible to quantify the mass of the disk to a value of $10^{-3}M_{\odot}$ for the nonspinning BH, reaching a value of $0.19M_{\odot}$ for the spinning one, and a mass of the ejecta that varies from $\approx 10^{-3}M_{\odot}$ for the first one to a value of $0.01M_{\odot}$ for the second.

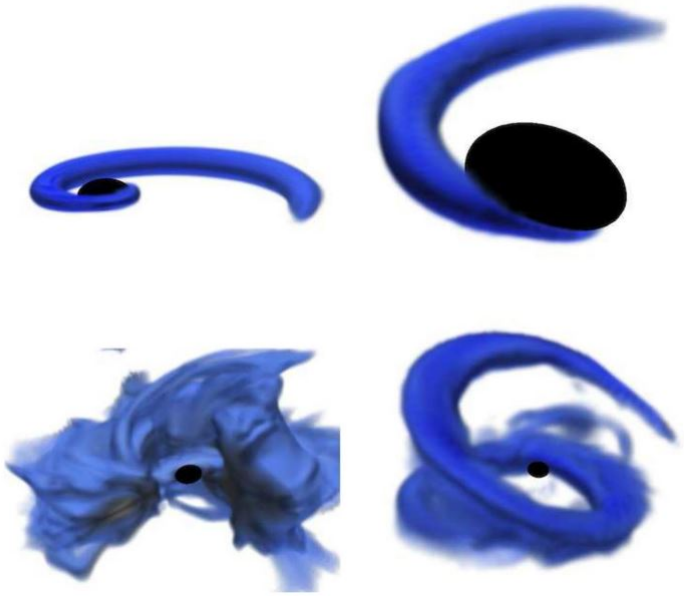

Figure 7: System with $Q = 7$, $\chi = 0.9$, and $\mathcal{C} = 0.144$ modeled by a $\Gamma = 2$ polytrope. The angles between the spin angular momentum of the black hole and the orbital angular momentum of the binary are 0° and 40° for the left and right panels. Image from: Foucart et al. (2013).

The possibility of dealing with inclined spins has also been considered in many simulations, even though covering the whole parameter space can become exceptionally demanding due to the increased number of degrees of freedom. Simulations with this property have not been handled during this project, however they do represent a valuable and informative test ground for astrophysics, since the inclination angle of the binaries has in fact a strong impact on the evolution of the system. Due to the misalignment between the angular momentum of the system and the orbital angular velocity vector, the vector normal to the orbital plane precesses around the system's angular momentum for the duration of the inspiral. Furthermore, this effect produces a net reduction of the tidal disruption, leading to less massive disk and dynamical ejecta. It is possible to relate spin-orbit interaction to the scalar product of the spin angular momentum $\boldsymbol{S}$ and the orbital momentum $\boldsymbol{L}$, $\boldsymbol{L} \cdot \boldsymbol{S}$, using post-Newtonian terminology (Kidder, 1995), which also means that the location of the ISCO will be affected by this product. Note-

[6]For this reason, the vast majority of current simulations have considered prograde or null spin.

worthy is the fact that, as the inclination angle increases, the spin-orbit repulsion for a given magnitude of the spin becomes weaker. Additionally, the shape of the dynamical ejecta will be distorted with respect to the spin-aligned case due to the violation of reflection symmetry, forming asymmetric remnants. We can have an idea of these effects by looking at Fig. 7 where we can see a system with the same parameters on the left and on the right but with different black hole inclination angles with respect to the total angular momentum (0° and 40° respectively). We can see how these systems evolve in both cases producing a tidal tail outside the ISCO. In the right column case, the tail self interacts creating a thick torus with an inclination angle different from the one of the non-precessing case. Eventually, a tilted disk will form, evolving in a different way than the aligned one, via processes like Lense-Thirring precession (Bardeen and Petterson, 1975), magnetically-induced turbulent viscosity (Fragile et al., 2007), or magnetic coupling with the remnant BH (McKinney et al., 2013).

2 The general relativistic 2 body problem

2.1 A Gravitational waves theory

The study of GW moves its first steps starting from Einstein theory of general relativity. Predicted in 1916, the first indirect experimental confirmation of GWs was in 1974, when Russell Alan Hulse and Joseph Hooton Taylor Jr. matched the orbital decay of a binary pulsar to the decay predicted by GR as energy lost via gravitational radiation. In this chapter, the main concepts related to the field of GR and GWs will be introduced, in order to get familiar with the terminology and the main theoretical ideas behind compact binaries inspiral and coalescence. Considering the Einstein Field Equation (EFE), written using the Einstein tensor $G_{\mu\nu}$ and the energy-momentum tensor $T_{\mu\nu}$

$$G_{\mu\nu} = 8\pi G T_{\mu\nu} \tag{8}$$

We can look for the simplest wave-like solutions that can be found in the weak field limit, by linearizing the equations around the Minkowski metric. In other words, we will consider a source of gravitational field sufficiently weak to justify an expansion around a flat spacetime. In this regime, we can assume the existence of a global inertial frame, where the metric tensor can be written as

$$g_{\mu\nu} = \eta_{\mu\nu} + h_{\mu\nu} \tag{9}$$

where $\eta_{\mu\nu}$ is the Minkowski metric, here defined with signature (-, +, +, +) and $|h_{\mu\nu}| \ll |\eta_{\mu\nu}| \ll 1$ are small perturbations on top of it. Quantities are then rewritten at first order in h, and the linearized equations are rewritten using the trace-reverse metric $\bar{h}_{\mu\nu}$ defined as

$$\bar{h}_{\mu\nu} = h_{\mu\nu} - \frac{1}{2}\eta_{\mu\nu}h \tag{10}$$

Applying gauge fixing conditions as the Lorenz or the Hilbert gauge, one can rewrite the EFE as wave equations:

$$\Box\bar{h}_{\mu\nu} = \frac{-16\pi G}{c^4}T_{\mu\nu} \tag{11}$$

Where c is the speed of light. If we now consider a further simplification such as the absence of a source term, we can obtain the linearized EFE in vacuum, which host solutions that can be constructed as a superposition of planar waves with constant wave vector k_μ and amplitudes $A^{\mu\nu}$

$$\bar{h}^{\mu\nu} = A^{\mu\nu}e^{ik_\rho x^\rho} \tag{12}$$

However, what we need is a description of a gravitational signal emitted from a mass/energy distribution. A formal solution for Eq. (11) can be obtained in terms of the Green function with retarded time $t_r := t - |\boldsymbol{x} - \boldsymbol{y}|/c$ (Jackson, 1975)

$$\bar{h}^{\mu\nu}(t, \boldsymbol{x}) = -\frac{4G}{c^4}\int \frac{T^{\mu\nu}(t_r, \boldsymbol{y})d^3\boldsymbol{y}}{||\boldsymbol{x} - \boldsymbol{y}||} \tag{13}$$

where $(t, \boldsymbol{x})$ labels the four-coordinates of an event on the spacetime, produced by a source spatially located in $\boldsymbol{y}$. Considering now a far-field approximation ($||\boldsymbol{y}|| \ll ||\boldsymbol{x}|| \sim ||\boldsymbol{x} - \boldsymbol{y}||$) and a source moving at slow velocities ($v \ll c$) we can perform a Taylor expansion of $\frac{1}{r} = \frac{1}{||\boldsymbol{x} - \boldsymbol{y}||}$ and considering only the leading order approximation

$$\bar{h}^{\mu\nu}(t, \boldsymbol{x}) = -\frac{4G}{c^4 r} \int T^{\mu\nu}(ct - r, \boldsymbol{y}) d^3\boldsymbol{y} \tag{14}$$

Among all the possible components of the stress-energy tensor $T^{\mu\nu}$, only the T^{ij} are time-varying and, therefore, possible sources of GWs. If we consider isolated sources without ongoing mass accretion processes, the energy content of the source T^{00} is constant in time, and so is the linear momentum along direction i, T^{0i} if we chose a reference frame that origins from the center of mass of the system. By using conservation laws on the flat background, it is possible to derive an equation for the integral of the spatial components T^{ij}

$$\int T^{ij}(ct', \boldsymbol{y}) d^3\boldsymbol{y} = \frac{1}{2c^2} \frac{d^2 I^{ij}(ct')}{dt'^2} \tag{15}$$

where I^{ij} is the moment of inertia tensor of the matter distribution. We can therefore simplify Eq. (14) considering only its spatial component

$$\bar{h}^{ij}(ct, \boldsymbol{x}) = -\frac{4G}{c^4 r} \int T^{ij}(ct_r, \boldsymbol{y}) d^3\boldsymbol{y} = -\frac{2G}{c^6 r} \left[\frac{d^2 I^{ij}(ct')}{dt'^2} \right]_{t'=t_r} \tag{16}$$

This formula, known as the quadrupole formula[7], represents a useful tool to relate the properties of the source to the physical phenomena measured at distance r. Using this definition, we developed a formalism that is only at leading order in the multipole expansion, valid only at a large distance from a (spatially) compact, slowly moving and non self-gravitating source. However, it is possible to show, e.g. (Thorne, 1980), that a generic gravitational source may be decomposed in an infinite series of multipoles, with the quadrupole being the lowest order one[8] (labeled with $\ell = 2$) described by the two indexes tensor $T^{\mu\nu}$. We can continue defining the moment of inertia tensor as

$$I^{ij}(ct) = \int T^{00}(ct, \boldsymbol{y}) y^i y^j d^3\boldsymbol{y} = c^2 \int \rho(ct, \boldsymbol{y}) y^i y^j d^3\boldsymbol{y} \tag{17}$$

the last identity is obtained in the limit of slowly moving particles where $T^{00} \sim \rho c^2$. We consider now the case of a binary system composed of two point masses in circular orbit

[7]More formally, the quadrupole formula is written substituting the inertia tensor with its traceless version, the quadrupole moment tensor defined in Eq. (64).

[8]The reason behind the absence of monopole and dipole moment ($\ell = 0$ and $\ell = 1$ respectively) is related to the conservation of mass and momentum. We leave as reference chapter 3 of Maggiore (2008).

on the (x_1, x_2) plane and reduce it to a one-body problem by introducing the reduced mass $\mu = m_1 m_2/(m_1 + m_2)$. The coordinates of the body, moving around the center of mass of the progenitor system are given by

$$\boldsymbol{x_s} = \begin{cases} x_s^1 = R\cos(\omega_s t) \\ x_s^2 = R\sin(\omega_s t) \\ x_s^3 = 0 \end{cases} \tag{18}$$

with ω_s as the orbital velocity of the effective body and R as the distance from the center during the circular motion. The density distribution of the particle is given by

$$\rho(ct, \boldsymbol{x}) = \mu\delta(x^1 - x_s^1)\delta(x^2 - x_s^2)\delta(x^3 - x_3^i) = \mu\delta(x^1 - R\cos(\omega_s t))\delta(x^2 - \sin(\omega_s t))\delta(x^3) \tag{19}$$

we can plug this definition into the moment of inertia tensor and find the associated values of $\bar{h}^{ij}$

$$\bar{h}^{ij}(ct, \boldsymbol{x}) = \frac{4G\mu R^2}{c^4 r}\omega_s^2 \begin{pmatrix} \cos(2\omega_s t_r) & \sin(2\omega_s t_r) & 0 \\ \sin(2\omega_s t_r) & -\cos(2\omega_s t_r) & 0 \\ 0 & 0 & 0 \end{pmatrix} \tag{20}$$

or, considering also the time component

$$\bar{h}^{\mu\nu}(ct, \boldsymbol{x}) = \frac{4G\mu R^2}{c^4 r}\omega_s^2 \begin{pmatrix} 0 & 0 & 0 & 0 \\ 0 & \cos(2\omega_s t_r) & \sin(2\omega_s t_r) & 0 \\ 0 & \sin(2\omega_s t_r) & -\cos(2\omega_s t_r) & 0 \\ 0 & 0 & 0 & 0 \end{pmatrix} \tag{21}$$

The number of independent components for a tensor inside the linearized EFE in vacuum is in principle 16 (being μ and ν, four-dimensional indexes) but applying symmetry and the Hilbert/Lorenz gauge, the problem reduces to 16-6-4=6 independent equations. However, freedom in the gauge's choice remains. Applying the traceless-tranverse (TT) gauge, that introduces four additional conditions, the system reduces to two degrees of freedom, with planar solution in the shape of

$$h_{\mu\nu}^{TT} = \begin{pmatrix} 0 & 0 & 0 & 0 \\ 0 & A_{11} & A_{12} & 0 \\ 0 & A_{12} & -A_{11} & 0 \\ 0 & 0 & 0 & 0 \end{pmatrix} e^{ie^{ik_\rho x^\rho}} \tag{22}$$

and are characterized by the values of $A_{11} = A_+$ and $A_{12} = A_\times$ which will denote the two possible polarization of the GW. Going back to Eq. (21), we can notice how a distant observer, looking at the two particles performing circular orbits on the (x_1, x_2) along the x_3 direction, receives a GW already projected on the TT gauge and therefore we can

define the two polarization as

$$\begin{cases} h_+ = \dfrac{4G\mu R^2}{c^4 r}\omega_s^2 \cos(2\omega_s t_r) \\ h_\times = \dfrac{4G\mu R^2}{c^4 r}\omega_s^2 \sin(2\omega_s t_r) \end{cases} \tag{23}$$

where we can assume r as the distance between the center of mass of the system and the GW detector. An additional generalization of these equations can be computed in the case of an observer looking at the inspiral along an arbitrary direction, forming an angle i with the orbital plane, such that $i = 0$ in the case of a line of sight perpendicular to (x_1, x_2)

$$\begin{cases} h_+ = \dfrac{4G\mu R^2}{c^4 r}\omega_s^2 \left(\dfrac{1+\cos^2(i)}{2}\right) \cos(2\omega_s t_r) \\ h_\times = \dfrac{4G\mu R^2}{c^4 r}\omega_s^2 \cos(i) \sin(2\omega_s t_r) \end{cases} \tag{24}$$

If one considers this system of equations as strictly Newtonian, the orbital parameters such as R and ω_s can be assumed as constant. In this framework, the circular orbits are stable, and no energy is subtracted from the system. However, in a relativistic context, GWs will be emitted, leading the orbits to shrink and the compact bodies to merge. This phenomenon is typically characterized by a very long timescale which also means that we can approximate the orbits as quasi-circular for the majority of the inspiral.

We continue the analysis by considering the back-reaction of the GWs emission on the system. The first theoretical work in this context was produced during the sixties, through fundamental works from Bondi, Goldberg, Newmann, Penrose, and many others. It clarified of GWs can not be explained via coordinate effects and how they can effectively transport energy and momentum. However, this topic comes with some caveats:

1. In GR there is no local definition of energy density for the gravitational field. This is a result of Einstein's equivalence principle, which allows us to eliminate gravitational forces at any point of the spacetime[9].

2. According to GR, any source of energy induces curvature through its stress-energy tensor. However, the definition of GWs given so far describes them as small perturbations on a flat background, that can not be curved. To reconcile this, there's a need to extend the concept of GWs as perturbations of a "generic background". A formal procedure related to this, was introduced by Isaacson, relying on a separation of scales of the variations of the metric (called short wave approximation).

[9]This concept is implemented in the diffeomorphism invariance of the theory, according to which a coordinate system such that in an arbitrary point p the metric is flat ($g_{\mu\nu}(p) = \eta_{\mu\nu}$) can always be considered.

This allows the identification of a background component upon which GWs can propagate.

$$g_{\mu\nu} \sim \text{background metric} + \text{waves} \tag{25}$$

In this way it is possible to define a stress-energy tensor suitable for GWs. However, this separation is not always allowed, and its applicability needs to be evaluated case-by-case by identifying the scales related to the chosen physical system.

3. A notion of global spacetime energy exists in the special cases of stationary spacetimes and other spacetimes describing isolated bodies. In this case (see section 3.4.1) a conserved global energy can be defined: we will come back to this point when talking about asymptotically flat spacetimes in NR.

Considering now an isolated system and a generic background metric $\eta_{\mu\nu}$, we postulate a formal expansion of the metric tensor as

$$g_{\mu\nu} = \eta_{\mu\nu} + h^{(1)}_{\mu\nu} + h^{(2)}_{\mu\nu} \tag{26}$$

which at first order is formally equal to the weak field approximation of Eq. (9). The terms $h^{(1)}_{\mu\nu}$ contain only short wavelength terms (or high frequency), while $h^{(2)}_{\mu\nu}$ can host long wavelength ones, due to resonance of high-frequency terms. In this way we can perform short-wave approximation, separating the contributions of the long wavelength terms (associated to the background) from the short ones (associated to the GWs). Averaging in time the long wavelength component leads to the definition of a stress energy tensor for GW (also known as Isaacson tensor) which is gauge invariant and that can be integrated inside a spherical surface of radius r to compute the GW luminosity dE/dt. In the case of a binary system in circular orbit, one can derive the total radiated power as

$$\frac{dE}{dt} = \frac{32}{5}\frac{G\mu^2}{c^5}R^4\omega_s^6 = \frac{32}{5}\frac{c^5}{G}\left(\frac{G\mathcal{M}_c\omega_{gw}}{2c^3}\right)^{\frac{10}{3}} \tag{27}$$

where in the last equivalence we introduced the chirp mass $\mathcal{M}_c = \mu^{3/5}(m_1+m_2)^{2/5}$ and the gravitational wave frequency $\omega_{gw} = 2\omega_s$. Assuming that this energy is subtracted by the orbital energy $E_{orb} = -G(m_1m_2)/2R$ during the motion

$$\frac{dE_{orb}}{dt} = -\frac{dE}{dt} \tag{28}$$

this balance law implies that the orbital energy will become more and more negative during the inspiral, leading the orbital radius to shrink and the orbital frequency to increase (and so the signal's frequency). Therefore, in presence of gravitational radiation, a circular orbit will be modified becoming an accelerated spiral motion during which the bodies become more and more relativistic as they approach until they collide. This leads to the emission of a characteristic signal, known as "chirp signal".

2.2 Relativistic stars and resonating black holes

2.2.1 Neutron stars

NSs are stellar remnants resulting from the gravitational collapse of a massive star during type II supernova event. They are the densest and tiniest stars known to exist in the universe and represent the ending point of stellar evolution for those objects whose mass was sufficiently large to trigger a core collapse event ($M > 11M_{\odot}$) but not enough to generate a BH ($M < 25M_{\odot}$). NSs have a typical mass in a range unexpectedly high: from modern observations we can set a typical regime between 1.2 $M_{\odot}$ and 2 $M_{\odot}$, which is increasing as new objects are discovered, supported by neutron degeneracy's pressure. While the masses can be today properly measured, the radius represents a real range of uncertainties as mentioned in section 1.4.1, and can be today estimated via pulse profile modelling related to brightness variations from the non-uniform surface of the NS, by fitting spectra with an appropriate atmospheric model to observations of the quiescent emission from low-mass X-ray binaries, through detections of gravitational waves from BNS systems together with many other techniques. Typical values range in 8-13 km, suggesting that the NS central density may reach values of 10 times the nuclear density ($\rho_{nuc} := 2.4{\times}10^{14}\mathrm{g/cm}^{-3}$), an ultra-dense regime for which the EOS is still unknown. NSs show a complicated layered structure, characterized by an outer solid crust (an ionic or nuclear lattice) where the pressure comes from degenerate electrons. As we delve deeper into the interior, the nature of the nuclei in the solid region changes: starting from layers that can have still some remnant of Fe, as the density increases we proceed toward a neutron rich medium, since pressure forces electron capture. Eventually, a point is reached where the conditions give rise to a fluid consisting of degenerate electrons, free nuclei, and free neutrons in a superfluid state. As the density continues to rise to ultra-high levels, the isolated nuclei are disrupted, leading to the formation of a neutron-rich fluid that characterizes the core and that can not be reconstructed in laboratories on Earth. Also, since the gravitational confinement of the star covers a long timescale, weak forces have time to operate, assembling ordinary matter into a stable state of exotic matter which can take very different forms including quarks locked up in hyperons, mixture of deconfined quarks etc...

When perturbed, a NS just like any other elastic body, is free to oscillate into a set of normal modes that involve the whole structure. There are different astrophysical processes during which these normal modes can be excited including supernovae explosions, the collapse of compact binary systems, or the formation of a proto-NS. There is a large literature describing the asteroseismologic properties of these bodies, but since this Master thesis is focused on describing BHNS systems, we won't go further into the detail of internal structure quakes and structural rearrangement, as well as in those modes associated to proto-NS formation related to the coalescence of NS-NS binaries.

The study of stellar perturbations starts from the definition of an equilibrium con-

figuration: considering a spherically-symmetric and nonrotating star[10], the metric inside and outside the NS can be described in the form:

$$ds^2 = -e^{2\Phi(r)}c^2dt^2 + e^{2\Lambda(r)}dr^2 + r^2(d\theta^2 + sin^2\theta d\phi^2) \tag{29}$$

The NS matter is here considered a perfect fluid with energy-momentum tensor given by

$$T^{\mu\nu} = (\rho + \frac{p}{c^2})u^\mu u^\nu + pg^{\mu\nu} \tag{30}$$

where ρ, p and u^μ are the density, pressure and four-velocity of the fluid. In this metric, the radial component of energy-momentum conservation gives[11]

$$\frac{dp}{dr} = -(\rho c^2 + p)\frac{d\Phi}{dr} \tag{31}$$

This recovers the Newtonian equation of hydrostatic equilibrium in the gravitational potential, since in the non-relativistic limit $p \ll \rho c^2$, this reduces to $dp/dr = \rho dU/dr$, where $U = -\Phi c^2$ is the sign-reversed gravitational potential. The 00 component of the Einstein equation gives

$$e^{-2\Lambda(r)} = 1 - \frac{2Gm(r)}{rc^2} \tag{32}$$

with $m(r)$ being the relativistic analogous of the energy/mass enclosed within a sphere of radius r:

$$m(r) = 4\pi \int_0^r dr' r'^2 \rho(r') \tag{33}$$

Combining the rr component of the Einstein equation with Eq. (31), we can get the relativistic equation for hydrodynamic equilibrium

$$\frac{dp}{dr} = -\frac{G}{c^2}(\rho c^2 + p)\left[m(r) + \frac{4\pi r^3 p(r)}{c^2}\right]\frac{1}{r[r - 2Gm(r)/c^2]} \tag{34}$$

Eqs. (31), (33), and (34) are the Tolman-Oppenheimer-Volkov (TOV) equations and, together with an EOS $p = p(\rho)$, determine the equilibrium configuration of a nonrotating NS. Perturbing this equilibrium configuration, it is possible to obtain a set of coupled wave equations for the matter and the spacetime variables from which the normal modes can be determined. In this way, it is possible to retrieve a rich spectrum of normal modes that includes fluid modes[12] where the matter variables $\delta\rho, \delta p, \delta u^\mu$ are excited, and spacetime modes where the metric perturbations outside the NS are excited. In the

[10]Notice that while the spherical symmetry approximation is excellent for equilibrium NS' configuration, the rotation is significantly important but challenging to model.

[11]Detailed derivations can be found in section 23.5 of Misner et al. (2017).

[12]Fluid modes are typically computed in the Cowling approximation, which consists of neglecting the spacetime perturbations.

simplest analysis, a NS is modeled using a polytropic EOS and it is approximated as a nonrotating, non magnetized object. In this approximation exists three main classes of fluid modes: fundamentals modes (f-modes), pressure modes (p-modes) and gravity modes (g-modes); for a more complete descriptions, r-modes from rotational effects and w-mode from spacetime perturbations outside the NS should be also considered.

2.2.2 Black hole perturbation theory

Just like the aforementioned case of NSs, also BHs can react to external disturbances vibrating in a set of normal modes. This kind of modes can be for instance excited by infalling material, then decay via GWs emission. To stress out the fact these modes are damped, they are typically referred to as **quasi-normal modes**. However, while in the case of NSs we could consider the presence of a resonating fluid, BHs are assumed purely spacetime oscillators. Despite this property, they do behave quite much like elastic bodies with (quasi-) normal modes that depend only on the BH's mass and spin. It is also important to point out that while for NSs we considered spacetime oscillations to affect the external region of the metric, for BH's we consider oscillations outside the horizon. To study gravitational perturbations of BH's, let's start by examining them as Schwarzschild solutions for static and spherically symmetric in vacuum Einstein equations. In this case, we can write the metric as

$$\bar{g}_{\mu\nu}dx^{\mu}dx^{\nu} = -A(r)(cdt)^2 + B(r)dr^2 + r^2(d\theta^2 + sin^2\theta d\phi^2) \tag{35}$$

where the notation used is

$$A(r) = 1 - \frac{R_S}{r}; \qquad B(r) = \frac{1}{A(r)} \tag{36}$$

where $R_S = 2GM/c^2$ is the Schwarzschild radius, denoting the spherical surface within which we locate the event horizon. The perturbations on such an object will be given by

$$g_{\mu\nu}(x) = \bar{g}_{\mu\nu}(x) + h_{\mu\nu}(x) \tag{37}$$

where $\bar{g}_{\mu\nu}(x)$ is the Schwarzschild metric, and $h_{\mu\nu}$ are the perturbations on top of it. We could for instance associate this scenario with the image of some external matter, described by an energy-momentum tensor $T_{\mu\nu}$, falling on the BH. In this sense we can associate an energy-momentum tensor to the infalling material and study the perturbed EFE assuming that this perturbation are sufficiently small to be studied in a linear regime. Starting from the EFE, we can expand the Einstein tensor $G_{\mu\nu}$ as in Eq. (37)

$$G_{\mu\nu} = \bar{G}_{\mu\nu} + \Delta G_{\mu\nu} \tag{38}$$

and knowing that the Schwarzschild metric is a solution for the EFE in vacuum $\bar{G}_{\mu\nu} = 0$, one finds that the equations governing the perturbations are

$$\Delta G_{\mu\nu} = \frac{8\pi G}{c^4} T_{\mu\nu} \tag{39}$$

There are different ways to proceed at this point, but a typical technique consists in choosing a suitable gauge (e.g. the Regge-Wheeler gauge) to simplify the equations. By doing that, and choosing suitable redefinitions, it is then possible to express the perturbations in terms of two master equations: the Regge-Wheeler equation for axial perturbation and the Zerilli equation for polar perturbation. Setting the source term to zero, one could study how these perturbation evolve with time by writing an equation in the form of

$$\phi''(\omega, x) + [\omega^2 - V(x)]\phi(\omega, x) = 0 \tag{40}$$

where $x = r^*/c$, and $r^* = r + R_S \log(r/R_S - 1)$ is known in the literature as tortoise coordinate, and $V(x)$ is a potential. This method eventually reduces to the standard praxis followed to study the response of a resonant bar or a resonant string: in that case, the imposition of the right boundary conditions (such as $\phi(t, \pm L/2) = 0$ for a string with fixed endpoints in $x = \pm L/2$) selects a discrete set of frequencies ω_m (known as normal frequencies) and whose associated solutions are the normal modes :

$$\phi_n(t, x) = e^{-i\omega_n t}\psi_n(x) \tag{41}$$

However, in the case of a perturbed BH there are no fixed endpoints where kinetic energy bounces back and forth: the system is open, which means that the energy of the perturbation will eventually disappear. For this reason, the solutions that one can find take the name of quasi-normal modes: they are damped oscillations describing the pulsational response of the BH to a perturbation, caused for instance by infalling matter. This set of quasi-normal modes generates the so-called ringdown signal and will lead the perturbed BH toward relaxation over a time-scale associated with the longest-living quasi-normal mode, typically of the order of R_s/c. To provide an example, the ringdown of a $10M_\odot$ BH will vanish with a timescale of a millisecond, while for a supermassive BH, with a mass of $10^6 M_\odot$ it can last for a few minutes.

2.2.3 Rotating black holes and the Newman–Penrose formalism

Until this point, the discussion about BHs was based on spherically symmetric, nonrotating, Schwarzschild BHs. However, in a more realistic astrophysical framework, BHs are expected to be rapidly rotating. Thinking about the gravitational collapse, a star will go through a strong reduction of its radius, and therefore, conservation of angular momentum implies a strong increase in its angular velocity. This means that even a slowly rotating progenitor star should in principle generate a remnant BH (or NS) which is rapidly spinning. To take this into account, it is necessary to modify (or better generalize) the Schwarzschild metric. We start by defining the Kerr metric for a BH with

mass M and angular momentum J as

$$\begin{aligned} ds^2 = &-(1-\frac{R_S r}{\rho^2(r,\theta)})c^2dt^2 - \frac{2aR_S r\sin^2\theta}{\rho^2(r,\theta)}cdtd\phi + \frac{\rho^2(r,\theta)}{\Delta(r)}dr^2 + \rho^2(r,\theta)d\theta^2 \\ &+ (r^2+a^2+\frac{a^2R_S r\sin^2\theta}{\rho^2(r,\theta)})\sin^2\theta d\phi^2 \end{aligned} \tag{42}$$

where a is called Kerr parameter, defined as

$$a := \frac{J}{Mc} \tag{43}$$

In the case of $a = 0$, the Kerr metric reduces to the Schwarzschild metric. Thinking about the motion of a particle in this geometry, we can appreciate many differences with respect to nonrotating BHs, for instance considering a radially moving particle falling into the BH from an infinite distance, which in the case of Schwarzschild geometry will always remain on a radial path, in the case of Kerr its geodesic is bent toward the direction in which the BH rotates: this will be for instance the case described by binary systems in the test-mass limit, where one of the two objects is extremely more massive than the other and the second one can be schematized as a point particle.

We could now look for the equations that govern perturbations of the Kerr metric in a similar way to what we did previously for Schwarzschild BHs. However, this time the equations are significantly more complicated, spherical symmetry can not be applied, and therefore a different formalism must be considered. We briefly introduce the Newman-Penrose formalism, just to provide the reader with some of the concepts that will be used during the numerical extraction of GWs (see section 4.2.2). Let's start by defining null tetrads on spacetime with metric $g_{\mu\nu}$ as a set of four linearly independent four-vectors

$$z^\mu_a = (l^\mu, n^\mu, m^\mu, \bar{m}^\mu) \tag{44}$$

The four-vectors l^μ and n^μ are real, while m^μ is complex and $\bar{m}^\mu$ is its complex conjugate. They are chosen for a specific metric, in this case the Kerr metric, with values such that

$$g_{\mu\nu}l^\mu l^\nu = g_{\mu\nu}n^\mu n^\nu = g_{\mu\nu}m^\mu m^\nu = g_{\mu\nu}\bar{m}^\mu\bar{m}^\nu = 0 \tag{45}$$

and

$$g_{\mu\nu}m^\mu\bar{m}^\nu = 1, \quad g_{\mu\nu}l^\mu n^\nu = -1 \tag{46}$$

We can now define the Weyl tensor, as a combination of the Riemann tensor $R_{\mu\nu\rho\sigma}$, the Ricci tensor $R_{\mu\nu}$ and the metric tensor $g_{\mu\nu}$:

$$C_{\mu\nu\rho\sigma} = R_{\mu\nu\rho\sigma} - \frac{1}{2}(g_{\mu\rho}R_{\nu\sigma} - g_{\mu\sigma}R_{\nu\rho} - g_{\nu\rho}R_{\mu\sigma} + g_{\nu\sigma}R_{\mu\rho}) + \frac{1}{6}R(g_{\mu\rho}g_{\nu\sigma} - g_{\mu\sigma}g_{\nu\rho}) \tag{47}$$

Projecting this tensor onto a null tetrad, we can define the following quantities, known as Newman-Penrose scalars

$$\begin{cases} \psi_0 = C_{\mu\nu\rho\sigma} l^\mu m^\nu l^\rho m^\sigma, \\ \psi_1 = C_{\mu\nu\rho\sigma} l^\mu n^\nu l^\rho m^\sigma, \\ \psi_2 = \dfrac{1}{2} C_{\mu\nu\rho\sigma} l^\mu n^\nu (l^\rho n^\sigma + m^\rho \bar{m}^\sigma), \\ \psi_3 = C_{\mu\nu\rho\sigma} n^\mu l^\nu n^\rho \bar{m}^\sigma, \\ \psi_4 = C_{\mu\nu\rho\sigma} n^\mu \bar{m}^\nu n^\rho \bar{m}^\sigma \end{cases} \tag{48}$$

Adopting a proper choice for the tetrads, it is possible to introduce a relation between the ψ_4 scalar and the GW + and × polarizations

$$\psi_4 = \ddot{h}_+ - i\ddot{h}_\times \tag{49}$$

This procedure has become nowadays a standard praxis in the field of NR, since provides a way to characterize GWs in terms of quantities that can be derived directly from the Riemann curvature tensor. However, this expression is valid only at an asymptotically far distance from the source. To have an additional in-depth analysis of GWs, the ψ_4 should be expanded using suitable functions, but since the Newman-Penrose scalars were derived for the Kerr geometry which is not spherically symmetric, it is not possible to perform a decomposition in spherical harmonics which was a typical way to describe the perturbations. However, it is still possible to separate the variables using a different set of functions known as spin-weighted-spherical-harmonics[13]

$$Y_s^{\ell m}(\theta, \phi) = (-1)^s \sqrt{\frac{(2\ell+1)}{4\pi}}\, d^\ell_{m(-s)}(\theta)\, e^{im\phi} \tag{50}$$

where the index s refers to the spin weight, and $d^{sm}_\ell(\theta)$ are called Wigner d-function, defined as

$$\begin{aligned} d^\ell_{ms}(\theta) = \sum_{t=C_1}^{C_2} (-1)^t \sqrt{\frac{(\ell+m)!(\ell-m)!(\ell+s)!(\ell-s)!}{(\ell+m-t)!(\ell-s-t)!t!(t+s-m)!}} \\ \times \left(\cos(\theta/2)\right)^{2\ell+m-s-2t} \left(\sin(\theta/2)\right)^{2t+s-m} \end{aligned} \tag{51}$$

with $C_1 = \max(0, m-s)$ and $C_2 = \min(\ell+m, \ell-s)$. In this way, one can obtain for a $s = -2$ field[14]

$$\psi_4(t, r, \theta, \phi) = \sum_{\ell,m} \psi_4^{\ell m}(t, r)\, Y^{-2}_{\ell m}(\theta, \phi) \tag{52}$$

[13]We leave as reference Gó mez et al. (1997) for a quick introduction to spin-weighted fields.

[14]See section 2.2.1 "Why a spin-2 field?" in Maggiore (2008).

and therefore, the waveform can be expanded in the same way

$$h = h_+ - ih_\times = \sum_{\ell m} h_{\ell m}(t, r)\, Y^{-2}_{\ell m}(\theta, \phi) \tag{53}$$

The multipolar waveforms $h_{\ell m}$ can be obtained by integrating twice in time $\psi_4^{\ell m}$, see Eq. 49. These quantities describe the intrinsic gravitational effect that we want to measure, while the spin-weighted spherical harmonics $Y^{-2}_{\ell m}(\theta, \phi)$ describe how the signal is projected on the sky. The gravitational wave strain h, represents the natural observable for GW and therefore, it is the natural quantity measured by detectors. Some problems can occur while moving from the numerically computed Ψ_4, to the detected h since their relation only holds at infinite distance, while GWs are numerically estimated at finite radii. We will come back to this problem in section 4.3.1.

2.3 Post-Newtonian formalism

The generation of GWs has been discussed until this point under the assumption that the background spacetime could be considered flat. This implied that sources of GWs in the far-field region were not contributing to the spacetime's curvature in the near-field region. Moreover, we computed an expansion in v/c to find the quadrupole formula assuming that the background curvature and the velocity of the source could be considered independent parameters (i.e. keeping the spacetime flat while expanding v/c). These assumptions are typically correct in the case of a system whose dynamic is not governed by gravitational forces: an example of this could be a system of particles moving in a Minkowski spacetime, or a beam of charged particles accelerated by an external electric field that could reach relativistic speeds, while not contributing to the curvature of the background metric. However, when dealing with astrophysical systems like self-gravitating bodies, i.e. compact objects, these assumptions may not hold; in such cases there is a need to extend the results of slowly moving, non-gravitating sources, with a more sophisticated formalism that can describe and account for self-gravitating objects.

The theory of gravitational radiation from isolated sources is a complex science. Deriving an exact and sufficiently general solution for the Einstein's equations, valid for extremely different matter systems, and describing accurately the emission and propagation of GWs from the source to an infinite distant detector, and their back-reaction mechanism, is extremely hard to obtain. Therefore, a typical way to proceed is by considering approximated methods, with the ultimate aim of extracting some firm predictions by producing template waveforms that can model all the stages from the inspiral to the post-merger and comparing them with the experimental outcomes (Ajith et al., 2008). Among the many different approximation methods, we considered the post-Newtonian approximation (PN), developed in 1916 by Einstein himself, by Droste, de Sitter, and Lorentz, following Blanchet (2014). This theory has been providing invaluable predictions on the physics of compact binaries, including problems of motion and gravitational

radiation (Damour, 1983). Let's start by defining as compact, those systems characterized by a distance between the two objects a, comparable to the total gravitational mass of the system M

$$a \approx \frac{MG}{c^2} \tag{54}$$

from this definition follows that only two astrophysical objects can be considered as compact: BHs and NSs. The creation of a complete and accurate template, however, is not a straightforward procedure: in fact, the PN approximation has a regime of validity that covers only slowly moving sources and weak field regimes. This can be appreciated by looking at the plot of Fig. 8, showing on the y-axis the symmetric mass ratio $\nu = (m_1 \cdot m_2)/(m_1 + m_2)^2$ which covers values closed to zero if one of the two objects is significantly larger then the other, condition that typically takes the name of test-mass limit, and values close to 1/4 in the case of equal masses; and, on the x-axis a slow-motion parameter v^2/c^2 that can be also interpreted as an indicator of the field's strength. This is an effect due to the virial theorem that sets a relation between the source's velocity and the gravitational potential

$$\left(\frac{v}{c}\right)^2 \sim \frac{2GM}{c^2 R} = \frac{R_s}{R} \tag{55}$$

In this notation, v is the relative orbital velocity and c stands for the speed of light. We can notice that when the two bodies have comparable masses and enter the strong field regime, i.e. they approach the coalescence, the tools that one can adopt are provided just by NR techniques, while BH perturbation theory can be exploited as an approximated technique for analyzing the post-merger waveform during the ringdown phase when the remnant BH emits radiation via quasi-normal modes [15]. What one could think now, is to adopt a complete NR simulation to have an ideal description of the waveform[16], however, this would require thousands of orbital cycles, computed with high precision. This last point, is manifestly unfeasible, both in terms of computational costs and in terms of the required accuracy. Therefore, the typical way to proceed is to combine the numerical results with the approximated ones from PN and perturbation theory. Nevertheless, this matching technique does not work particularly well, and better methods are required to fill the gap between the PN inspiral and the NR merger phase. An idea for doing that is provided by the effective-one-body (EOB) formalism, which provides a way to extend the domain of validity of the PN model beyond the inspiral phase (see section 2.5). In the case of PN approximation, the matter source is considered at once slowly moving and weakly stressed. Therefore, we can define a PN parameter ϵ, which is always

[15]It can be furthermore used for describing the coalescence of binaries with an extreme mass ratio in the test-mass limit.

[16]Interestingly enough, in this branch of physics there is a notable preference for numerically computed solutions, often regarded as more accurate and reliable, over the analytical ones sometimes deemed as too approximated.

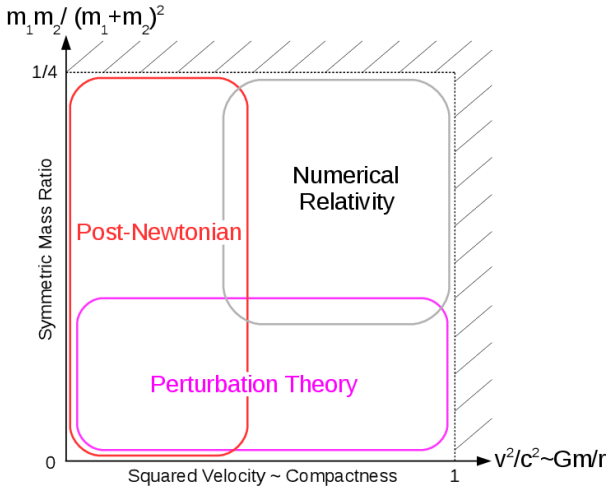

Figure 8: Sketch showing the different regimes of validity of PN, NR and perturbation theory. Image from: Blanchet (2019).

significantly smaller than one, and which is defined from the stress-energy Tensor and the source's Newtonian potential U as

$$\epsilon := \max\left[\left|\frac{T^{0i}}{T^{00}}\right|, \left|\frac{T^{ij}}{T^{00}}\right|^{\frac{1}{2}}, \left|\frac{U}{c^2}\right|^{\frac{1}{2}}\right] \tag{56}$$

this parameter reduces to a slow-motion estimation $\epsilon \approx v/c \ll 1$. The definition of slow-motion can sound in this definition a little inappropriate since we can consider very relativistic sources as inspiralling compact binaries that can reach values of v/c closed to 50% in the last orbits, by introducing contributions of higher-order PN approximations. If the PN parameter ϵ of the studied source is sufficiently small, then we can proceed by expanding in ϵ. As a formal note, we will call an expansion in ϵ^n, $n/2$ PN order[17].

We end this section by providing a quick description of the energy of compact binaries in circular orbits with masses $m_1 > m_2$ and dimensionless spin $\chi_i = S_i/m_i^2$ $(i = 1, 2)$. Other useful definitions for a more compact notation are

$$\widetilde{a}_i := \frac{S_i}{mm_i} = \frac{\chi_i m_i}{m}, \quad \widehat{a}_0 := \widetilde{a}_1 + \widetilde{a}_2, \quad \widetilde{a}_{12} := \widetilde{a}_1 - \widetilde{a}_2. \tag{57}$$

In the test mass limit, $\widetilde{a}_1 \to S_1/(m_1)$ is the dimensionless spin of the large black hole and $\widetilde{a}_2 \to 0$. Defining x as

$$x = \left(\frac{1}{2}\frac{Gm}{c^3}\omega_s\right)^{2/3} \tag{58}$$

[17]As pointed out in many different studies, e.g. Cutler et al. (1993b), Cutler et al. (1993a) and many others, in order to obtain a sufficiently accurate theoretical template, contributions up to 3PN level must be included.

the energy of circular orbits can be rewritten as the sum of three/four different contributions

$$E(x) = E_{orb}(x) + E_{so}(x) + E_{ss}(x) \tag{59}$$

where the different terms describe the orbital, spin-orbit and spin-spin interactions. In the case of finite size effects due to the presence of matter, like in the case BNS or BHNS binaries, an additional contribution will be given by the tidal effects. A more in depth description of the latter will be provided in section 2.4. The leading order contribution is given by $E_{Newt} = \dfrac{-\mu c^2 x}{2}$ The expansion of each of these terms is particularly long and therefore we report only a few of the leading terms

$$\begin{aligned}\frac{E_{\rm orb}}{E_{\rm Newt}} =& 1 - \left(\frac{3}{4} + \frac{\nu}{12}\right) x + \left(-\frac{27}{8} + \frac{19\nu}{8} - \frac{\nu^2}{24}\right) x^2 + \left(-\frac{675}{64} + \left(\frac{34445}{576}\right.\right. \\ & \left. - \frac{205\pi^2}{96}\right)\nu - \frac{155\nu^2}{96} - \frac{35\nu^3}{5184}\Bigg) x^3 + \Bigg[-\frac{3969}{128} + \left(\frac{9037\pi^2}{1536} - \frac{123671}{5760}\right. \\ & \left. + \frac{448}{15}(2\gamma_E + \ln(16x))\right)\nu + \left(\frac{3157\pi^2}{576} - \frac{498449}{3456}\right)\nu^2 + \frac{301\nu^3}{1728} + \frac{77\nu^4}{31104}\Bigg] x^4 + \dots\end{aligned} \tag{60}$$

where $\gamma_E = 0.577\dots$ is the Euler constant. The spin contribution are

$$E_{\rm so} = -\frac{1}{6}(7\hat{a}_0 + \widetilde{a}_{12}\sqrt{(1-4\nu)})\nu x^{5/2} + \dots \tag{61}$$

$$E_{\rm ss} = \frac{1}{2}\hat{a}_0^2 \nu x^3 + \dots \tag{62}$$

Notice that the above definition for the spin-orbit interaction is defined as a negative value. This will have a relevant impact in terms of the evolution and the dynamics of the system. More information on this topic can be found in section 5.2 where it is shown how these different contributions can be extracted and measured.

2.4 Tidal effects

The discussion made in section 1.3 did not consider in a detailed way the effects of tidal deformation except for the elongation parameter c_R. Tidal interaction can behave as an additional attractive force, with the ability to modify the location of the ISCO, the orbital evolution, and the criterion for tidal disruption. The relativistic theory of tides in its current form for compact binary coalescence (Damour and Nagar, 2009) is due to the work of Thibault Damour (Damour, 1983). The tidally deformed NS originates a quadrupole moment with a magnitude of component $\propto r^{-3}$, and the gravitational potential develops a r^{-6} term in addition to the usual r^{-1} term of the monopolar interaction, therefore it will be crucial to determine the properties of the closest orbits. In this way, tidal effects make the potential more attractive, making the coalescence process faster if

compared to a pure nonspinning BBH case where these phenomena are absent. The tidal effects enter the equation at the fifth PN order, but it is important to remark that the point-particle terms at this order still have to be derived. For this reason, GW modelling via EOB formalism and NR has become more and more important in the last few years.

The theory of tidal deformation for NSs can be characterized by their **Love numbers**. Starting from Newtonian gravity, we can consider an external gravitational potential U_{ext} (generated by a companion in the binary system) acting on the NS, generating a quadrupolar tidal field.

$$\mathcal{E}_{ij} = -\partial_i \partial_j U_{ext} \tag{63}$$

Considering a nonrotating NS, as a spherically symmetric object, the presence of an external tidal field would produce perturbation $\delta\rho$ in the equilibrium position of the NS' self-gravitating fluid. Outside the NS we can perform a multipole expansion taking as origin its center of mass: in this way we can generate an unperturbed monopole term Gm/r (with m being the NS's mass), a dipole term which vanishes being on the center of mass frame, and other high order terms produced by the deformed NS. The total potential will be therefore given by an "external" contribution, related to the companion, and a "self" contribution related to the deformation. The first term generated by the perturbation can be found inside the second moment of the mass density, and can be written using the quadrupole moment tensor, a traceless version of the moment of inertia tensor seen in Eq. (15), defined as

$$Q^{ij} = \int d^3x \rho(t, \boldsymbol{x})(x^i x^j - \frac{1}{3} r^2 \delta^{ij}) \tag{64}$$

We can add the potential created by the deformed NS to the gravitational potential of the companion as a second external potential $U_{ext} = -\frac{1}{2}\mathcal{E}_{ij} x_i x_j + O(x^3)$ so to have a total potential $U(t, \boldsymbol{x})$ given by

$$U(t, \mathbf{x}) = \frac{Gm}{r} + \frac{3G}{2r^5} x^i x^j Q_{ij}(t) + O\left(\frac{1}{r^4}\right) - \frac{1}{2}\mathcal{E}_{ij}(t) x_i x_j + O(x^3) \tag{65}$$

This equation is valid in the star's local asymptotic rest frame (asymptotically mass-centered Cartesian coordinates) at large distance r. The equation is characterized by the presence of three dominant terms: the standard gravitational potential, and two leading order terms arising from the perturbation: one describing an external tidal field and one describing the resulting tidal distortion. Considering the external perturbation $\mathcal{E}_{ij}$ as static, then also the star's induced quadrupole term will also be constant in time and the potential U will be just a function of the spatial coordinate $\mathbf{x}$. By making this assumption, the quadrupole term can be rewritten at linear order as

$$Q_{ij}(t) = -\lambda \mathcal{E}_{ij}(t) \tag{66}$$

where λ can be found in the literature, e.g. (Hinderer et al., 2010), as an EOS-dependent tidal deformability parameter related to the $l = 2$ tidal Love number k_2

$$k_2 = \frac{3}{2}\frac{G\lambda}{R^5} \tag{67}$$

where R is the NS' radius. We can use this definition to redefine the quadrupole moment tensor as

$$Q_{ij} = -\frac{2}{3G}k_2 R^5 \mathcal{E}_{ij} \tag{68}$$

The potential takes the form

$$U(t, \mathbf{x}) = \frac{Gm}{r} - \frac{1}{2}\mathcal{E}_{ij}(t)x_i x_j \left[1 + 2k_2 \left(\frac{R}{r}\right)^5\right] + O\left(\frac{1}{r^4}\right) + O(x^3) \tag{69}$$

This procedure can be extended to any generic l, by considering higher-multipole contributions of the external field. It is possible to define a Love number k_l for each Newtonian multipole considering the Newtonian approximation of the g_{00} component of the metric.

$$g_{00} = -1 + 2\frac{2Gm}{c^2 r} - \frac{1}{c^2}\sum_{l=2}^{\infty}\frac{2}{l(l-1)}\mathcal{E}_{i_1,i_2,\ldots,i_l}x^{i^1}\ldots x^{i^l}\left[1 + 2k_l\left(\frac{R}{r}\right)^{2l+1}\right] \tag{70}$$

However, working with higher accuracy means developing a fully relativistic theory of tidal deformation. In particular, working in a strong field regime means that Eq. (64) and 63 are no longer valid; while we can still use Eq. (65) in the asymptotically flat region at a large distance from the source. To do that, the appropriate way to proceed is to consider perturbation theory over the equilibrium configuration of the star. This problem will be separated into an interior and exterior problem, that will consider respectively the perturbed equations inside and outside the NS. In this way, the metric perturbations are separated per each multipole into polar and axial modes and their coefficients, which, as long as we only consider the exterior problem are just free parameters, will define two families of Love numbers: *electric type* $k_l^{(e)}$ for polar modes and *magnetic-type* $k_l^{(m)}$ for axial modes. We can use them to parametrize the most general solution for the perturbation of the component of the metric. In the case of non-relativistic limit, the magnetic type multipoles just disappear and we go back to Eq. (70). To estimate the Love numbers, we start by considering the TOV equilibrium configuration (which carries information about the EOS) together with perturbed EFE and perturbed hydrodynamical equations. Matching the external and internal solution, for a range of realistic EOS, we can find typical values of k_2 between 0.05 and 0.15. An additional effect related to tidal fields is a modification of the equation of motion: given the presence of a quadrupole moment, the orbits of the binary system will be modified. Considering a frequency domain inspiral waveform in PN approximation, the GW phase

evolution is, at large separations and low orbital frequencies, driven by the value of the chirp mass only. However as the frequency increases and the objects get closer the phase evolution will be more and more influenced by the tidal effects, that can eventually become the dominant effect towards the end of the inspiral in the case of nonspinning BNS. It is convenient to define the tidal polarizability Λ to introduce the phase correction due to tidal effects

$$\Lambda_i = \frac{2}{3} k_2 \left(\frac{R_i}{G m_i / c^2} \right)^5 \tag{71}$$

which can take typical values between 10^2 and 10^3 with the larger values obtained for less compact NSs. The definitions here reported are typical of a BNS system, but can be easily reduced to the BHNS case by assuming a single NS. In the case of BNS we can define a reduced tidal polarizability as

$$\tilde{\Lambda} = \frac{16}{13} \frac{(m_1 + 12 m_2) m_1^4 \Lambda_1 + (m_2 + 12 m_1) m_2^4 \Lambda_2}{(m_1 + m_2)^5} \tag{72}$$

so that the phase correction can be written as

$$\Delta \Psi^{tidal} = -\frac{117}{256} \frac{m^2}{m_1 m_2} \tilde{\Lambda} \left(\frac{v}{c} \right)^5 \tag{73}$$

In some case, especially near the late inspiral phase, this tidal effects can overcome lower-order terms in the PN expansion making them detectable for third-generation interferometers.

2.5 The Effective-One-Body framework

The effective-one-body (Buonanno and Damour, 1999) is a complex Hamiltonian formalism that incorporates results from PN, black hole perturbation theory and NR to generate GWs templates. It allows to map the general-relativistic two-body problem into the dynamics of an effective particle in an effective metric, starting from PN knowledge and introducing suitable resummations of the Taylor expansions to obtain a more compact notation of the PN terms. Introducing only the main results, the first idea consists of combining together the results from the PN inspiral of compact bodies, with the test-mass results for a point-like object, orbiting in the gravitational field of a BH without causing spacetime deformation, where the weak field limit assumption can be avoided and strong field features such as the presence of an ISCO or a lightring can be described exactly for both the Schwarzschild and the Kerr metrics. To simplify the results, the notation in this section will pose $G = c = 1$ and will consider only nonrotating BHs.

In the case of the GR two-body problem for objects with mass m_1 and m_2, the dynamics is encoded into the mass-shell condition of each particle

$$g^{\mu\nu} p_\mu p_\nu = p^2 = -m^2 \tag{74}$$

with $p_\mu = mu_\mu/\sqrt{-u_\nu u^\nu}$ being the four-linear momentum and u^μ the four-velocity. In fact, considering a Schwarzschild metric and the problem of a test particle with mass μ, orbiting around a BH with mass M, we can rewrite the mass-shell condition as a condition for a Hamiltonian that will describe the equation of motion through an action principle. The idea is to map this two-body problem into an effective-one-body problem, in a similar way to what was done for the Newtonian binary problem. In the latter case, a system of two masses orbiting around their center of mass could be described using a variable transformation, obtaining a body with relative momentum $\boldsymbol{p} = \boldsymbol{p}_1 = -\boldsymbol{p}_2$ and reduced mass $\mu = m_1 m_2/(m_1+m_2) = m_1 m_2/M$ orbiting around a fixed gravitational background described by a mass $M = m_1 + m_2$, with total linear momentum $\boldsymbol{P} = \boldsymbol{p}_1 + \boldsymbol{p}_2 = 0$ in the center of mass frame. In the relativistic case, we can write the total four-momentum as $P^\mu = p_1^\mu + p_2^\mu$ where p_i^μ $(i = 1, 2)$ are the momenta of the two individual bodies. To efficiently map the two-body problem we have therefore to find a mass-shell condition for P^μ that associates the results

$$p_i^2 = m_i^2 \longrightarrow P^\mu = ? \tag{75}$$

Simplifying the problem assuming flat space, i.e. considering the two bodies moving along straight lines without interaction, one can set $g_{\mu\nu} = \eta_{\mu\nu}$ and in the center of mass frame, the relative four-momentum is

$$p^\mu = \left(-\frac{1}{M} p_{1\mu} p^{2^\mu},\ \frac{1}{M} P_0 p_1^i\right), \tag{76}$$

with $p_1^i = -p_2^i$. One can find the constraints for the relative and total momenta as

$$-p_\mu p^\mu = \mu^2, \qquad -P_\mu P^\mu = M_p^2 = M^2\left[1 + 2\nu\left(-\frac{p_0}{\mu} - 1\right)\right] \tag{77}$$

with $\nu = \mu/M$. We have therefore two constraints: one for the total center of mass momentum and one for the effective particle. We can at this point calculate the real Hamiltonian and the effective Hamiltonian with the map $(p_0 \Longleftrightarrow P_0)$ since

$$H = -P_0 \qquad H_{\text{eff}} = -p_0 \tag{78}$$

Solving for the real Hamiltonian, that describes the binary motion we can find

$$H = \sqrt{M^2[1 + 2\nu(H_{\text{eff}}/\mu - 1)] + P^2} \tag{79}$$

which is purely obtained from the kinematics of particles without interaction[18]. The next step consists of finding a PN approximation for the real Hamiltonian H. However,

[18]In the case the center of mass is static, P^2 can be neglected. However, in the case of strongly asymmetric systems, the emission of radiation is larger along a certain direction, pushing the system and leading to a moving remnant BH.

it is important to recall that this function is not unique and equivalent descriptions can be achieved through canonical transformations. Therefore $H_{\rm PN}$ and H don't have to be exactly the same function but can be interconnected by these transformations. There are different methods to face this problem which are based on comparing gauge independent quantities or explicitly constructing the canonical transformations. We proceed by providing a modified version of the test-body Hamiltonian $H_{\rm eff}$, achieved by deforming the Schwarzschild metric, Eq. (35), and the mass-shell condition, Eq. (74) but this time estimated for the effective particle μ.

$$g^{\rm eff}_{\mu\nu}\, dx^\mu dx^\nu = -A dt^2 + \frac{dr^2}{A\cdot \bar{D}} + \frac{r^2}{c}(d\theta^2 \sin^2\theta d\phi^2) \tag{80}$$

$$g^{\mu\nu}_{\rm eff}\; p_\mu p_\nu + Q = \mu^2 \tag{81}$$

where $A, \bar{D}$ and C are functions of r and ν, and Q is function of r, ν and p_r. With these choices the effective Hamiltonian takes the form

$$H_{\rm eff} = -p_0 = \sqrt{A\left(\mu^2 + A\cdot\bar{D}\cdot p_r^2 + \frac{L^2}{r} + Q\right)} \tag{82}$$

and it reduces to the case of a particle moving on a Schwarzschild's spacetime for $\bar{D} = 1$ and $Q = 0$. To efficiently construct the mapping between the effective and the real Hamiltonian, we have to match these functions to the PN results. In this way one can find the EOB potentials

$$A = 1 - 2u + 2\nu u^3 + (\frac{94}{3} - \frac{41\pi^2}{32}\cdot\nu u^4) + \dots \tag{83}$$

$$\bar{D} = 1 + d\nu u^2 + (52\nu - 6\nu^2)u^3 + \dots \tag{84}$$

$$Q = 2(4-3\nu)\nu u^2 p_r^4 \tag{85}$$

with $u = M/r$, while r is the relative distance between the two particles. The content of the EOB potential is based on an infinite amount of terms coming from the PN Taylor expansion, therefore resummation techniques should be employed to improve the model. However, since the entire series is unknown a priori some guesswork has to be performed and must be verified against all the available exact results. A relevant example in this sense is provided by Padé approximants, described in Appendix D and that comes with fitting coefficient to be estimated.

The Q potential describes how the motion deviates from a geodesic line: in the case of circular orbits $p_r = 0$, $Q = 0$ and $\bar{D}$ is negligible, therefore the dynamics is exclusively related to the A potential. Using the same formulas of a Schwarzschild's spacetime, for which $A = 1 - 2u$, one can find strong field features, including the existence of an ISCO (at $r \sim 6M_{BH}$) and a lightring (at $r \sim 3M_{BH}$). The latter represents an unstable orbit for massless particles like photons: an object positioned on it can move

on a circular orbit as long as its motion is purely tangential. However, even the slightest radial perturbation inward or outward will cause it to either fall into the black hole or be ejected from the system. Therefore, thinking about an object that is emitting GWs while moving on the lightring, half of the radiated energy will escape, while the other half will be absorbed by the BH. Notably, the GWs emitted from this region will exhibit the largest amplitude in the waveform creating a distinctive signature in the signal, followed by an absolute minimum that marks the end of the chirp signal. However, it is essential to note that at this point the dynamics is also reaching the highest velocity and, therefore, the assumption of circular orbits becomes ineffective. Taking this into account, an EOB waveform can be improved by introducing a multiplicative correction called Next-to-Quasi-Circular correction. This modification allows for the development of an inspiral+plunge waveform which is then smoothly connected to a ringdown model derived from the BH perturbation theory, providing a comprehensive representation of the entire gravitational wave signal encompassing inspiral, plunge, and ringdown phases. The discussion made until this point however, was concerning only BBH systems. The extension to BHNS and BNS comes with the necessity to include tidal effects: this can be done by modifying the EOB potential (Damour and Nagar, 2010)

$$A \longrightarrow A + A_{tidal} \tag{86}$$

with an expression that includes free parameters and the electric and magnetic type Love number. The model obtained is then tuned using NR simulations that fix those free coefficients that characterize the resummation techniques, the Next-to-Quasi-Circular corrections, and the tidal parameters. This matching process is approached as a parameter estimation problem where the NR waveform is treated as the reference model, with the goal of identifying the set of parameters that best align the analytical model with the NR simulation, ensuring an optimal fit between the two, refining and calibrating the EOB result.

2.6 `TEOBResumS`

The EOB model utilized and studied during the development of this project is `TEOBResumS`. Initially proposed in Nagar et al. (2018) as an approximant to describe spinning BBH and BNS[19], it was then improved with the possibility to describe BHNS systems in Gonzalez et al. (2023a). In this way, it can describe at the same time tidal and spin-orbit effects, including high order modes[20]. This model is based on an analytical description of the dynamics through the inspiral, merger, and ringdown phases, which was made possible through information coming from NR simulations that can drastically improve the

[19]The tidal model used to describe BNS evolution up to the merger was initially proposed in Bernuzzi et al. (2015).

[20]See as references Akcay et al. (2019) and Riemenschneider et al. (2021).

late-inspiral, strong-field, and fast-velocity regime of the model. This procedure consists of least-square fitting many NR waveforms to analytical templates with free coefficients. For instance, in the case of BNS and BHNS, tidal interactions are quantified using a set of dimensionless tidal polarizability coefficients (for each deformed body) that can be tuned in this way. The most important of the latter can be found in the literature as tidal polarizability parameter Λ, and that we already described in Eq. (71). These parameters strongly vary with the NS's internal structure: both the radius R and the gravito-electric love number k_2 are fixed for a given mass by the chosen EOS; therefore measuring them can provide strong constraints on the allowed EOS for cold degenerate matter at supranuclear density. This was done for the first time in Abbott et al. (2017a), putting constraints that disfavor some of the stiffest EOS. The construction of BHNS waveforms from the early inspiral to the ringdown is similar to the one of BBH: in fact, the results are expected to be in extremely good agreement for those systems characterized by a NS that is not tidally disrupted during the inspiral. Also in the case of a mass-shedding limit met outside the ISCO, the waveform is a chirp-like signal qualitatively similar, but modified by the presence of tidal effects. Nevertheless, in both of the cases, the ringdown waveform will differ from the one produced by BBH, as well as the post-merger remnant. Therefore, the approach followed to create BHNS model consists of employing NR fitting formulas that describe how much a given quantity differs from the BBH case. To construct the waveform, an accurate model for the remnant BH's mass and dimensionless spin is required: this can be achieved via fitting formulas based on NR simulated data, that allow to map M^{BH}_{rmn} and χ^{BH}_{rmn}, knowing the symmetric mass ratio ν, the tidal polarizability parameter Λ and the dimensionless spin of the progenitor BH χ^{BH} (Zappa et al., 2019). In particular, in the $\Lambda \approx 0$ limit, the model reduces to the BBH case, and in the $\nu \approx 0$ limit, it furthermore reduces to the test mass case. It is important to notice how the amount of stellar material falling onto the BH will impact the final mass and spin of the remnant (more details on this will be provided in section 5.4). As far as the ringdown emission is concerned, `TEOBResumS` has implemented a BHNS model constructed as a deformation of the EOB ringdown for BBH. However, the NS's tidal disruption is still playing a fundamental role, damping significantly the emission of quasi-normal modes: in those regions of the parameter space where this is going to happen, the BBH representation of the ringdown is no longer accurate. Also in this case fitting formulas are required, with coefficients related to the amplitude and the frequency at the peak of each quasi-normal mode and free coefficients to be fitted from NR data. However, the state of the art of the parameter space's exploration for BHNS systems, is not sufficiently advanced to investigate efficiently the waveforms for different mass ratios and spin configurations for different EOS. It is therefore fundamental to efficiently produce NR simulated data, as to create realistic templates able to capture the complex physics hidden behind compact binary mergers.

3 Numerical Relativity

The following section will be used to guide the reader through the main concepts of Numerical Relativity with the aim of providing the fundamental information necessary for a better understanding of the rest of the project. Here we will find the most important concepts and problems associated with solving EFE using numerical techniques. Just to provide a brief excursus on the topic, I will start by saying that the formalism here introduced, called **3+1 formalism** is nowadays used in a large collection of physical problems including :

- Gravitational collapse and black hole formation
- Black holes and neutron stars collisions
- Dynamical stability of stationary solutions (from rotating stars and discs to black strings)

and originates from works by Georges Darmois in the 1920s, André Lichnerowicz in the 1930-40 and Yvonne Choquet-Bruhat in the 1950s. In the late fifties and sixties the 3+1 formalism was adopted by Richard Arnowitt, Stanley Deser and Charles W. Misner to propose the Hamiltonian formulation of general relativity known as *ADM formalism*. In the 1970s a crucial role was covered by the work of James W. York, who developed a general method to solve the initial data (ID) problem and who put the 3+1 equations in the shape used afterward by the numerical community (hereafter ADMY equations). The main idea behind this formalism consists in rewriting EFE as a set of partial differential equations (PDE), slicing the four-dimensional spacetime (procedure known as *foliation*) using three-dimensional surfaces (called *hypersurfaces*). This procedure allows us to reformulate EFE as a *Chauchy problem* with constraints.

3.1 Framework and Notation

We start by considering a spacetime $(\mathcal{M}, \boldsymbol{g})$ where $\mathcal{M}$ is a four-dimensional manifold and $\boldsymbol{g}$ a Lorentzian metric on $\mathcal{M}$ with signature (-, +,+,+). We assume it to be time orientable, so that every light cone of the metric $\boldsymbol{g}$ can be divided continuously over $\mathcal{M}$ in two parts: a past and a future cone. Choosing any point $p \in \mathcal{M}$, we can define the four-dimensional tangent space to p as $\mathcal{T}(\mathcal{M})_p$ and its dual space (also called co-tangent space) as $\mathcal{T}^*(\mathcal{M})_p$. The following index convection from Gourgoulhon (2007) has been adopted:

- Greek indices run in 0,1,2,3. Letters from the beginning of the alphabet $(\alpha, \beta, \gamma, \dots)$ for free indices and letters starting from μ $(\mu, \nu, \rho, \dots)$ as dumb indices for contraction, to make more manifest the tensorial degree of any equation

- Lower case latin indices from i $(i, j, k, \dots)$ run in 1,2,3 while those starting from a $(a, b, c, \dots)$ run only in 2,3

With this notation, we can define a basis vector $(\boldsymbol{e}_\alpha)$ for the tangent space $\mathcal{T}^(\mathcal{M})_p$ and another one $(\boldsymbol{e}^\alpha)$ for the associated dual space $\mathcal{T}^*(\mathcal{M})_p$. Therefore we can define the component $T^{\alpha_1 \dots \alpha_p}{}_{\beta_1} \dots {}_{\beta_q}$ of a tensor $\boldsymbol{T}$ of type $\binom{p}{q}$ with respect to these basis $(\boldsymbol{e}^\alpha)$ and $(\boldsymbol{e}_\alpha)$ through the expansion

$$\boldsymbol{T} = T^{\alpha_1 \dots \alpha_p}{}_{\beta_1} \dots {}_{\beta_q} \boldsymbol{e}_{\alpha_1} \otimes \dots \otimes \boldsymbol{e}_{\alpha_p} \otimes \boldsymbol{e}^{\beta_1} \otimes \dots \otimes \boldsymbol{e}^{\beta_q}$$

3.2 Geometry of hypersurfaces

As mentioned in the previous section, in order to solve EFE algorithmically, what we want to do is rewrite them as an evolution problem in which a three-dimensional spatial slice is evolved in time. More formally, we can assume that a four-dimensional spacetime can be subdivided into a family of hypersurfaces Σ, namely the images of three-dimensional manifolds $\hat{\Sigma}$ by an embedding (i.e. a 1-to-1 map) $\Phi : \hat{\Sigma} \to \mathcal{M}$ such that $\Sigma = \Phi(\hat{\Sigma})$. Thanks to this one-to-one character each point of Σ is mapped by a single point in $\hat{\Sigma}$, both Φ and Φ^{-1} are continuous, and the hypersurface Σ is guaranteed not to intersect itself and is considered as spacelike. To define what a spacelike hypersurface is, let's consider a coordinate system $x^\alpha = (x^0, x^i)$ of $\mathcal{M}$, so that Σ can be defined as the level set of a scalar field on $\mathcal{M}$, that is to say a set of points for which that scalar field is constant. For instance, calling t the scalar function associated to x^0 (that we'll later identify with being the time coordinate), one could say that

$$\forall p \in \mathcal{M}, p \in \Sigma \iff t(p) = 0 \tag{87}$$

In other words, one could introduce a coordinate system[21] of $\mathcal{M}$ $((x^0, x^i) = (t, x, y, z))$ such that t spans $\mathbb{R}$, (x, y, z) are Cartesian coordinates spanning $\mathbb{R}^3$, and Σ can be defined by those coordinate having $t = 0$. The vector normal to the surface will be described by the gradient $\boldsymbol{d}x^0$ whose components are

$$\nabla^\alpha t = g^{\alpha\mu} \nabla_\mu t = g^{\alpha\mu} (\boldsymbol{d}x^0)_\mu \tag{88}$$

which defines the unique direction perpendicular to Σ. In particular we can characterize Σ as spacelike, having a timelike $\nabla^\alpha t$. Also we can call $\boldsymbol{v}$ any vector tangent to Σ so that $\langle \boldsymbol{d}t \ , \ \boldsymbol{v} \rangle = 0$. In this way any other vector normal to Σ must be collinear to $\boldsymbol{\nabla} t$.

We can renormalize $\boldsymbol{\nabla} t$ to make it a unit vector by setting

$$\boldsymbol{n} := (\pm \boldsymbol{\nabla} t \cdot \boldsymbol{\nabla} t)^{-1/2} \boldsymbol{\nabla} t \tag{89}$$

[21] Assuming Σ as a connected submanifold of $\mathcal{M}$, with topology $\mathbb{R}^3$.

with $\boldsymbol{n} \cdot \boldsymbol{n} = -1$ being Σ spacelike, the unit normal vector is chosen as to point toward increasing values of t. In this way, we can decompose any four-dimensional tensor into spatial parts defined on the hypersurfaces, and timelike part normal to Σ and aligned with $\boldsymbol{n}$. It is also important to notice that, when talking about embedding and maps, what we are doing is to consider a three spatial manifold $\hat{\Sigma}$ whose curves and vectors are carried on $\mathcal{M}$ by a mapping Φ such that (see Fig. 9)

$$\hat{\Sigma} \to \mathcal{M} \tag{90}$$

$$(x, y, z) \mapsto (0, x, y, z) \tag{91}$$

If one considers the vectors belonging to the tangent space of $\hat{\Sigma}$, we can define a mapping Φ_* so that those vectors $\boldsymbol{v} = (v^x, v^y, v^z)$ are transformed into vectors of the tangent space of $\mathcal{M}$, $\Phi_* \boldsymbol{v} = (0, v^x, v^y, v^z)$. This procedure takes the name of push-forward mapping. Conversely, one can define a pull-back mapping between the linear forms of $\mathcal{T}_p(\mathcal{M})$ and those on $\mathcal{T}_p(\hat{\Sigma})$. Applying the latter procedure to the spacetime metric $\boldsymbol{g}$, one could define an induced metric also known as **3-metric**.

$$\gamma = \Phi^* \boldsymbol{g} \tag{92}$$

so that

$$\gamma_{ij} = g_{ij} \tag{93}$$

This "reverse mapping" can be intuitively described also in terms of an orthogonal projector P (or explicitly $P^{\alpha}_{\ \beta} = \delta^{\alpha}_{\ \beta} + n_\alpha n_\beta$), so that

$$\begin{aligned} \mathcal{T}_p(\mathcal{M}) &\to \mathcal{T}_p(\Sigma) \\ \boldsymbol{v} &\mapsto \boldsymbol{v} + (\boldsymbol{n} \cdot \boldsymbol{v})\boldsymbol{n} \end{aligned}$$

In particular, the 3-metric can be obtained from

$$\gamma_{\alpha\beta} = P^{\mu}_{\ \alpha} P^{\nu}_{\ \beta}\ g_{\mu\nu} = g_{\alpha\beta} + n_\alpha n_\beta \tag{94}$$

From the above formula, the projector is nothing but the 3-metric $\gamma_{\alpha\beta}$ with an index raised with $g_{\alpha\beta}$ we can therefore use it to find the spatial part of any four-dimensional tensor.

3.2.1 Curvature

Since in this discussion we considered only spacelike hypersurfaces, what we have is a non-degenerate, definite positive[22], induced metric $\boldsymbol{\gamma}$. This implies the existence of a

[22] A definite positive or Riemannian metric is characterized by a signature (+,+,+).

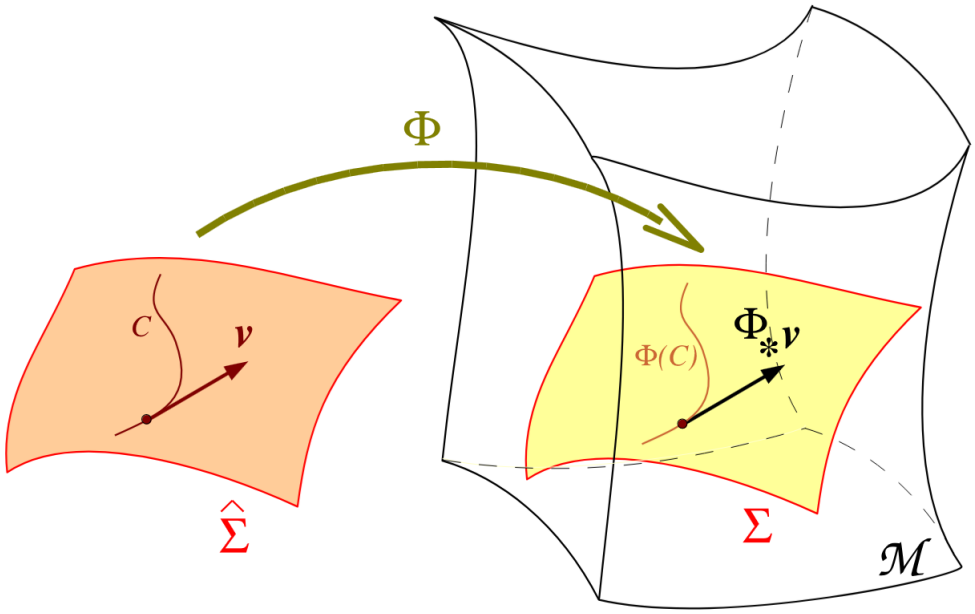

Figure 9: Embedding of a three-dimensional manifold $\hat{\Sigma}$ in a four-dimensional one $\mathcal{M}$, defining the hypersurface Σ. The vector $\boldsymbol{v}$, tangent to some curve C in $\hat{\Sigma}$ is mapped into a vector tangent to the mapped curve $\Phi(C)$. Image from Gourgoulhon (2007).

unique connection, which also means a unique covariant derivative $\mathbf{D}$, on the manifold Σ, so that

$$\mathbf{D}\boldsymbol{\gamma} = 0 \tag{95}$$

which takes the name of Levi-Civita connection, and an associated Riemann tensor, defined as:

$$(D_i D_j - D_j D_i)v^k = R^k{}_{lij}v^l \tag{96}$$

which provides a measure of the intrinsic curvature of (Σ, γ), just like ${}^4R^{\mu}{}_{\nu\alpha\beta}$ does for $(\mathcal{M}, \mathbf{g})$. In order to enhance readability, we denote the three Riemann tensor ${}^3R^k{}_{lij} := R^k{}_{lij}$. The information we lack in this description is related to how Σ is bent inside $\mathcal{M}$. This bending corresponds to the change of direction of the normal vector $\boldsymbol{n}$ as one moves from $\hat{\Sigma}$ to Σ and we can describe it using a tensor called extrinsic curvature tensor

$$K_{\alpha\beta} = -\gamma^{\mu}{}_{\alpha}\gamma^{\nu}{}_{\beta}\nabla_{\mu}n_{\nu} \tag{97}$$

Another way to cast this definition, is by using the Lie Derivative along the normal vector $\boldsymbol{n}$

$$K_{\alpha\beta} = -\frac{1}{2}\mathcal{L}_{\mathbf{n}}\gamma_{\alpha\beta} \tag{98}$$

also known as kinematical equation. In this context, the Lie derivative can be considered as a geometric generalization of the partial time derivative ∂_t even though formally, it

represent a way to measure how much a change in a tensor field along a given direction x_α differs from an infinitesimal coordinate transformation generated by x_α (see Fig. 11).

We can therefore associate the evolution of the 3-metric to the extrinsic curvature. In this terms, a four-dimensional globally hyperbolic spacetime[23]$(\mathcal{M}, \mathbf{g})$, foliated[24] by a family of non intersecting hyperfurfaces Σ_t (so that $\mathcal{M} = \cup\Sigma_t$) can be represented as the time evolution of a three-dimensional slice $(\Sigma_0, \boldsymbol{\gamma})$, see Fig. 10.

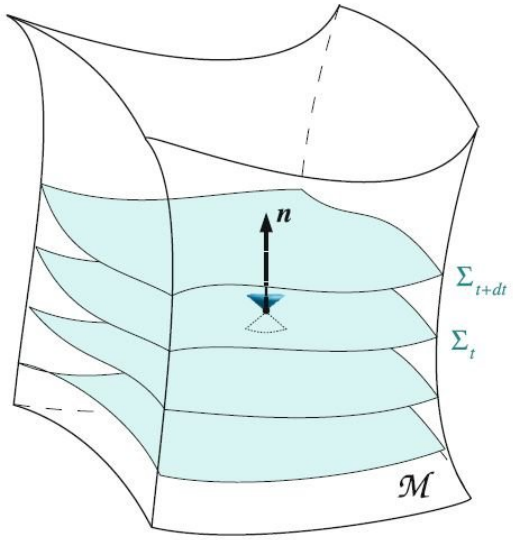

Figure 10: Foliation of the spacetime $\mathcal{M}$ by a family of spacelike hypersurfaces $(\Sigma_t)_t \in \mathbb{R}$. Image from Gourgoulhon (2007).

3.2.2 Foliation kinematic

As mentioned in the above section, the timelike future directed unit vector $\boldsymbol{n}$, normal to the slice Σ_t can be written as

$$\boldsymbol{n} := -\alpha \boldsymbol{\nabla} t \tag{99}$$

with α being $(-\boldsymbol{\nabla} t \boldsymbol{\nabla} t)^{-1/2}$ and a minus sign so to have future oriented vectors $\boldsymbol{n}$ for a scalar field t increasing toward the future. We define the scalar field α the **lapse func-**

[23]A spacetime is said to be globally hyperbolic if it admits spacelike hypersurfaces Σ such that each causal curve (that is to say timelike or null curve) intersects Σ once and only once.

[24]Any globally hyperbolic surface can be represented as a family of spacelike hypersurfaces Σ_t. By foliation or slicing we refer to the existence of a smooth scalar field $\hat{t}$ on $\mathcal{M}$ which is regular and such that each Σ_t is a level surface of it

$$\forall t \in \mathbb{R}, \Sigma_t = p \in \mathcal{M}, \hat{t}(p) = \text{const} = t$$

tion, which by construction is always positive and never vanishes for regular foliations. Considering the normal vector $\boldsymbol{n}$, one can define worldlines orthogonal to Σ_t: physically this means that the hypersurfaces represent the set of events that happens simultaneously from the perspective of some observer that we will call **Eulerian observer** and whose acceleration is given by

$$\boldsymbol{a} := \boldsymbol{\nabla}_{\boldsymbol{n}}\boldsymbol{n} = \boldsymbol{D}\ln\alpha \tag{100}$$

The vector $\boldsymbol{a}$ is orthogonal to $\boldsymbol{n}$ and tangent to Σ_t. Together with $\boldsymbol{n}$ we can also define a normal evolution vector

$$\boldsymbol{m} = \alpha\boldsymbol{n} \tag{101}$$

With these definitions we can provide some kinematic properties of 3+1 GR exploiting geometrical properties of spacelike foliations:

- The normal evolution vector carries points from Σ_t to $\Sigma_{t+\delta t}$;
- Tensors defined on Σ_t can be transported to tensors on $\Sigma_{t+\delta t}$ using the Lie derivative along the normal evolution vector m^α;
- The Lie derivative of the 3-metric (i.e. its time evolution) is given by the extrinsic curvature $\boldsymbol{K}$.

3.3 3+1 decomposition of Einstein Equation

In Eq. (98) we can see an interpretation of the extrinsic curvature being the time derivative of the spatial metric. It should not come as as surprise that spatial projection of the four Riemann tensor will internalize factors related to $\boldsymbol{K}$ and to its time derivative. ${}^4R^\alpha{}_{\beta\gamma\delta}$ can be projected in three different ways: projecting all four indexes on Σ produces the Gauss equation

$$\gamma^\mu{}_\alpha\gamma^\nu{}_\beta\gamma^\gamma{}_\rho\gamma^\sigma{}_\delta\ {}^4R^\rho{}_{\sigma\mu\nu} = R^\gamma{}_{\delta\alpha\beta} + K^\gamma{}_\alpha K_{\delta\beta} - K^\gamma{}_\beta K_{\alpha\delta} \tag{102}$$

Three spatial projection and a contraction with $\boldsymbol{n}$ takes the name of Codazzi equation

$$D_\beta K^\gamma{}_\alpha - D_\alpha K^\gamma{}_\beta = \gamma^\gamma{}_\rho n^\sigma\gamma^\mu{}_\alpha\gamma^\nu{}_\beta\ {}^4R^\rho{}_{\sigma\mu\nu} \tag{103}$$

Two spatial projections and two contractions with $\boldsymbol{n}$ give the Ricci's equation

$$\gamma_{\alpha\mu}n^\rho\gamma^\nu{}_\beta n^\sigma\ {}^4R^\mu{}_{\rho\nu\sigma} = \frac{1}{\alpha}\mathcal{L}_m K_{\alpha\beta} + \frac{1}{\alpha}D_\alpha D_\beta\alpha + K_{\alpha\mu}K^\mu{}_\beta \tag{104}$$

We can now use these equations to decompose EFE obtaining Hamiltonian and momentum constraints and evolution equations for the extrinsic curvature. Let's start by considering the Einstein equation without cosmological constant:

$${}^4\boldsymbol{R} - \frac{1}{2}R\boldsymbol{g} = 8\pi\boldsymbol{T} \tag{105}$$

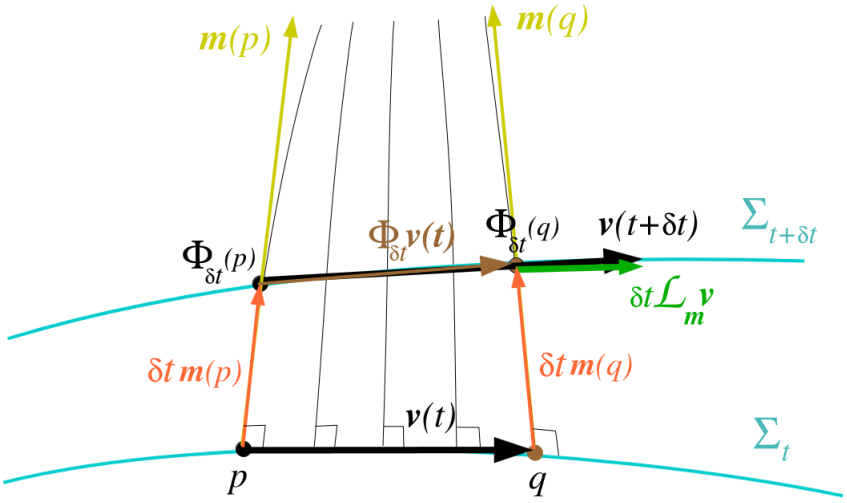

Figure 11: Let's consider a vector $\mathbf{v}$ as the infinitesimal displacement between two points q and t on the hypersurface Σ_t. Transporting those points on the neighboring hypersurface $\Sigma_{t+\delta t}$ along the field lines of vector field $\boldsymbol{m}$. The displacement between $p(t)$ and $\Phi_{\delta t}(p)$ is given by $\delta t\boldsymbol{m}$. The new points on $\Sigma_{t+\delta t}$ denote a new vector $\Phi_{\delta t}\boldsymbol{v}(t)$ tangent to it. The geometrical interpretation of the Lie Derivative of $\boldsymbol{v}$ along direction $\boldsymbol{m}$ is the difference between the value of $\boldsymbol{v}$ in $\Phi_{\delta t}$. i.e. $v(t+\delta t)$. and the vector transported along $\boldsymbol{m}$ $\Phi_{\delta t}\boldsymbol{v}(t)$. Image from Gourgoulhon (2007).

Where ${}^4\boldsymbol{R}$ is the Ricci tensor[25] associated to $\boldsymbol{g}$, R is the Ricci scalar and $\boldsymbol{T}$ is the matter stress-energy tensor. Let's consider as usual a globally hyperbolic spacetime $(\mathcal{M}, \boldsymbol{g})$, foliated by Σ_t spacelike hypersurfaces. The 3+1 formalism aims to project the EFE on and perpendicularly to Σ_t. Projecting Eqs. (105) entirely along $\boldsymbol{n}$ and using the Gauss equation (102) one can obtain

$$R + K^2 - K_{ij}K^{ij} = 16\pi E \tag{106}$$

a scalar equation known as Hamiltonian constraint. The variable E is defined as the matter-energy density as measured by an Eulerian observer

$$E := n^\mu n^\nu T_{\mu\nu} \tag{107}$$

Projecting once on Σ_t and once along $\boldsymbol{n}$ and using the Codazzi equation (103) we obtain the momentum constraint (a rank 1 tensorial equation with 3 components)

$$D_j K^i{}_j - D_i K = 8\pi p_i \tag{108}$$

[25] In terms of components, the Ricci tensor can be considered as a contraction of the Riemann tensor, such that ${}^4R_{\alpha\beta} = {}^4R^\mu{}_{\alpha\mu\beta}$.

with $p_\alpha = -T_{\mu\nu}n^\mu\gamma^\nu{}_\alpha$ as the matter momentum density as measured by the Eulerian observer. The reason why Eqs. (106) and (108) take the name of constraints is adducible to the fact that the final form of 3+1 EFE will be the one of a time evolution system tractable as a Cauchy problem with them constituting the constraints, and therefore will have to hold on each individual spatial slide Σ_t. The full projection onto Σ_t produces instead the evolution equation

$$\mathcal{L}_m K_{ij} = -D_i D_j \alpha + \alpha \left\{ R_{ij} + K K_{ij} - 2K_{ik}K^k{}_j + 4\pi[(S-E)\gamma_{ij} - 2S_{ij}] \right\} \tag{109}$$

where S is the trace of the projected stress-energy tensor $S_{\alpha\beta} = \gamma^\mu{}_\alpha \gamma^\nu{}_\beta T_{\mu\nu}$. In this way it is possible to rewrite the 10 EFE (four of which involving only first time derivatives of the metric $\boldsymbol{g}$ and six involving second time derivatives) in a system of 4+6+6 equations (106,108, 109, 98) typically referred to as ADM equations, Arnowitt R. (1962). While the two constraints set values for $\boldsymbol{\gamma}$ and $\boldsymbol{K}$ on every slice, the other two provide a description of how these quantities evolve forward in time from one hypersurface to the other. The general covariant behaviour of EFE is maintained in the 3+1 form, and translated in the freedom of choice for the lapse function and for the three spatial coordinates which are unspecified on Σ_t. We can therefore proceed to introduce coordinates on the four-dimensional manifold, a procedure necessary to convert our system of tensorial equations into a system of PDE. We can choose on each hypersurface some coordinate system $(x^i) = (x^1, x^2, x^3)$, and if it varies smoothly from one slice to the other then we can define a well-behaved coordinate system $(x^\alpha) = (t, x^1, x^2, x^3)$ on $\mathcal{M}$. We can define a set of basis $\boldsymbol{\partial_\alpha} = (\boldsymbol{\partial}_t, \boldsymbol{\partial}_i)$ for $\mathcal{T}_p(\mathcal{M})$, associated with coordinates x^α

$$\begin{aligned} \boldsymbol{\partial}_t &:= \frac{\partial}{\partial t} \\ \boldsymbol{\partial}_i &:= \frac{\partial}{\partial x^i}, \qquad i \in (1,2,3) \end{aligned}$$

where $\boldsymbol{\partial}_t$ is tangent to the lines of constant spatial coordinates. However, in general, $\boldsymbol{\partial}_t$ is not a timelike vector: its direction depends on the spatial coordinates. One could be tempted to say that $\boldsymbol{m}$ and ∂_t coincide, but this is true only in the special case of having coordinates x^i such that the lines $x^i = \text{const}$ are orthogonal to the foliation (see Fig. 12). The difference between them is described by the **shift vector**, $\boldsymbol{\beta}$:

$$\boldsymbol{\partial}_t = \boldsymbol{m} + \boldsymbol{\beta} = \alpha \boldsymbol{n} + \boldsymbol{\beta} \tag{110}$$

which is always tangent to the hypersurfaces Σ_t. We can now specify the tensorial ADM equations using this system of adapted coordinates to obtain PDEs. However, one could notice that some freedom remains in the choice of the lapse function and for the shift vector which must be specified to close the system. The simplest choice one could make is to consider

$$\alpha = 1; \qquad \beta^i = 0 \tag{111}$$

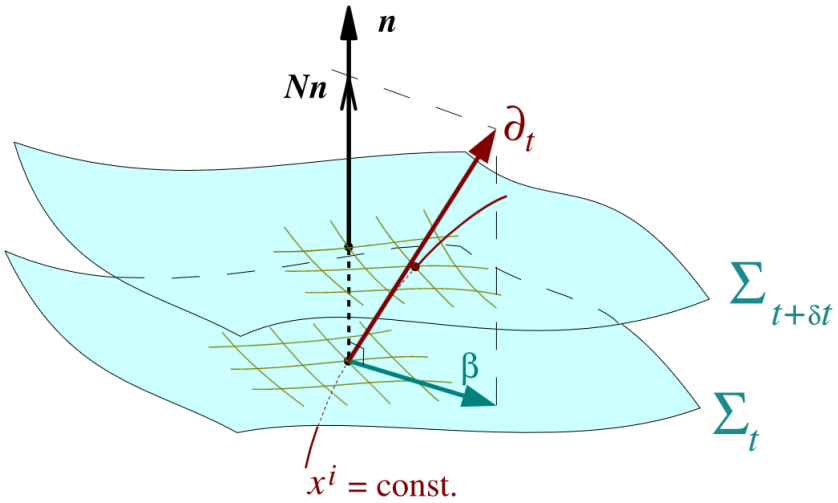

Figure 12: Coordinates (x^i) on the hypersurfaces. The lines $x^i = \text{const}$ define time vector ∂_t which differs from the normal evolution vector (in this figure the letter N refers to the lapse function α) by a shift vector $\boldsymbol{\beta}$. Image from Gourgoulhon (2007).

this choice takes the name of Geodesic gauge or Geodesic slicing. In this case, the constant spatial coordinates are orthogonal to the hypersurfaces and the time coordinate is the proper time of the Eulerian observer. It is also possible to rewrite the ADM equation using this gauge as :

$$\partial_t \gamma_{ij} = -2K_{ij} \tag{112}$$

$$\partial_t K_{ij} = R_{ij} + KK_{ij} - 2K_{ik}K^k{}_j + 4\pi[(S-E)\gamma_{ij} - 2S_{ij}] \tag{113}$$

$$R + K^2 - K_{ij}K^{ij} - 16\pi E = 0 \tag{114}$$

$$D_j K^j{}_i - D_i K - 8\pi P_i = 0 \tag{115}$$

ending up with a system of nonlinear PDE, of first order in time and second order in space wavelike equations. In order to find a solution, initial data must be provided, satisfying the four constraint equations. However, this procedure involves specify some free data, whose choice has physical meaning and it is based on:

1. Astrophysical expectations for the solution;
2. Physical meaning of the metric fields;
3. Mathematical necessity (equations must be well-posed, decoupled, etc...).

3.4 The initial data problem

In the previous section we discussed how, thanks to the 3+1 decomposition, finding a solution for the EFE can be reconsidered to solving a Cauchy problem, consisting in evolving forward in time a set of initial data. However, finding suitable values is not an easy task, being subjected to the Hamiltonian and momenta constraints. The problem could be split into two main parts:

1. a mathematical problem: given a hypersurface Σ_0, find a Riemannian metric $\boldsymbol{\gamma}$, a symmetric bilinear form $\boldsymbol{K}$ and some matter distribution $(E, \boldsymbol{p})$ on Σ_0 such that the constraints are satisfied;

2. an astrophysical problem: the solution to the constraint equations should not be random, but should take into account the physical system that one is studying.

There are many possible ways to solve this issue: one of the most used today is based on splitting the initial data to be found $(\boldsymbol{\gamma}, \boldsymbol{K})$, between an arbitrarily chosen part, and a second part obtained by solving the constraints (Lichnerowicz, 1944). This idea, proposed initially by Lichnerowicz, was then extended in Choquet-Bruhat (1971), York (1979) and more recently in Pfeiffer and York (2003), and take the name of conformal decompositions method.

3.4.1 Asymptotic flatness & global quantities

Before jumping straight into the initial data problem, let's start by providing an overview of the main concept of energy in GR starting from the case of asymptotically flat (AF) spacetimes. The concept of asymptotic flatness can be applied to stellar-type objects, in isolated conditions and to be faced, the existence of an extra structure on the hypersurfaces Σ_t is required, named as **background metric** $\boldsymbol{f}$. $\boldsymbol{f}$ has signature (+,+,+) (so it is a Riemannian metric as $\boldsymbol{\gamma}$) and its component f_{ij} are time evolved along ∂_t, following the condition:

$$\frac{\delta f_{ij}}{\partial t} = 0 \tag{116}$$

and if the topology of Σ_t allows it, then $\boldsymbol{f}$ is typically chosen as a flat metric (so that its Riemann tensor vanishes). Going back to the concept of asymptotic flatness, a spacetime is said to be asymptotically flat if $\forall \Sigma_t \; \exists f_{ij}$:

1. f_{ij} is flat (except on the strong field region where we have located our source);

2. There is a Cartesian-type coordinates system $x^i = (x, y, z)$ on Σ_t such that outside the strong field region $\boldsymbol{f} = \mathrm{diag}(1, 1, 1)$ and $r = \sqrt{x^2 + y^2 + z^2}$ can take arbitrarily large values on Σ_t;

3. when $r \to +\infty$, the components of $\boldsymbol{\gamma}$ satisfy

$$\gamma_{ij} = f_{ij} + O(r^{-1}) \tag{117}$$

$$\frac{\partial \gamma_{ij}}{\partial x^k} = O(r^{-2}) \tag{118}$$

4. when $r \to +\infty$, the components of $\boldsymbol{K}$ satisfy

$$K_{ij} = O(r^{-2}) \tag{119}$$

$$\frac{\partial K_{ij}}{\partial x^k} = O(r^{-3}) \tag{120}$$

So besides a narrow region of the spacetime, what we have are asymptotically decaying conditions. Noteworthy the fact that requirement 3. forbids the existence of gravitational waves at spatial infinity, however, this issue can be solved by considering that any isolated source has started emitting GWs at a finite time in the past and that these waves have still not reached the spatial infinity.

In a AF spacetime, it is always possible to define a global conserved energy contained on each Σ_t and therefore a mass. Let's define $\mathcal{V}$ as the portion of $\mathcal{M}$ delimited by two hypersurfaces Σ_{t_1} and Σ_{t_2} $(t_1 < t_2)$

$$\mathcal{V} = \bigcup_{t=t_1}^{t_2} \Sigma_t \tag{121}$$

and its boundary $\partial\mathcal{V}$ (assumed as a timelike hypersurface). Defining $\mathcal{S}_t$ as

$$\mathcal{S}_t = \partial\mathcal{V} \cap \Sigma_t \tag{122}$$

we can describe the ADM mass of the slice Σ_t as

$$M_{ADM} = -\frac{1}{16\pi} \lim_{\mathcal{S}_t \to +\infty} \oint_{\mathcal{S}_t} [\mathcal{D}_j \gamma_{ij} - \mathcal{D}_i(f^{kl}\gamma_{kl})] s^i \sqrt{q} d^2y \tag{123}$$

where $\mathcal{D}$ is the connection associated to the background metric $\boldsymbol{f}$, s^i represents the unit vector normal to $\mathcal{S}_t$, and $\sqrt{q}d^2y$ denotes the surface element induced by the spacetime metric[26] on $\mathcal{S}_t$. In particular if one uses Cartesian coordinates x^i, then $\mathcal{D}_i = \dfrac{\partial}{\partial x^i}$ and $f^{kl} = \delta^{kl}$ Eq. (123) can be written as

$$M_{ADM} = -\frac{1}{16\pi} \lim_{\mathcal{S}_t \to +\infty} \oint_{\mathcal{S}_t} (\frac{\partial \gamma_{ij}}{\partial x^j} - \frac{\partial \gamma_{jj}}{\partial x^i}) s^i \sqrt{q} d^2y \tag{124}$$

[26]In this case $\mathbf{q}$ is the induced metric on $\mathcal{S}_t$, $y^a = (y^1, y^2)$ are arbitrary coordinates on $\mathcal{S}_t$, for instance $y^a = (\theta, \phi)$, and q is the determinant of q_{ab}.

and always takes finite values thanks to AF conditions. By taking the Newtonian limit, the ADM mass represents the total mass of the considered system. Moreover, it can be shown, e.g. (Schoen and Yau, 1979) and (Schoen and Yau, 1981), that if matter obeys the dominant energy condition $E^2 \geq P_i P^i$, then the ADM mass is always non-negative and it is null only in the case of having Minkowskian hypersurfaces Σ_t with extrinsic curvature $\boldsymbol{K} = 0$. Remarkable is the fact that, although from a theoretical perspective this quantity should remain constant in time, during NR simulations this integral is computed on spheres of finite radius, therefore the numerical approximation could lead to a violation of this condition.

Another conserved quantity that will be useful later on, is the ADM angular momentum $\boldsymbol{J_{ADM}}$ associated with the invariance of the action with respect to rotations. One could then define a set of rotational killing vectors ϕ_i of $\boldsymbol{f}$, associated with a rotation about the x, y, and z axis respectively, in terms of Cartesian coordinates x_i:

$$\phi_x = -z\boldsymbol{\partial}_y + y\boldsymbol{\partial}_z \tag{125}$$
$$\phi_y = -x\boldsymbol{\partial}_z + z\boldsymbol{\partial}_x \tag{126}$$
$$\phi_z = -y\boldsymbol{\partial}_x + x\boldsymbol{\partial}_y \tag{127}$$
$$\tag{128}$$

One can then define the ADM angular momentum as

$$J_i := \frac{1}{8\pi} \lim_{\mathcal{S}_t \to +\infty} \oint_{\mathcal{S}_t} (K_{jk} - K\gamma_{jk})(\phi_i)^j s^k \sqrt{q} d^2 y \tag{129}$$

3.4.2 Conformal decomposition

The specification of the 12 variables that characterize the γ_{ij} and K_{ij} components of the induced metric and of the extrinsic curvature on Σ_0 is what characterizes the initial data problem. To find an estimation for these quantities what one could do is to use the four constraints equations, ending up eventually with an over-determined problem where the prescription of some quantities is required in order to solve for the others. A typical approach to this problem involves a conformal decomposition of γ_{ij} (Lichnerowicz, 1952) in the form

$$\boldsymbol{\gamma} = \Psi^4 \bar{\boldsymbol{\gamma}} \tag{130}$$

where Ψ, called **conformal factor**, is some scalar field strictly positive and $\bar{\boldsymbol{\gamma}}$ an auxiliary metric on Σ_t, necessarily positive definite as $\boldsymbol{\gamma}$, that will be referred to as the **conformal metric**. At first glance, this could look like a superficial mathematical trick, fruitful only in terms of simplifying the calculations of the constraint equation. However at a deeper level, it defines an equivalence class of manifolds and metrics, related by $\bar{\gamma}_{ij} = \gamma^{1/3}\gamma_{ij}$ where γ is the determinant of the induced metric. By choosing $\bar{\gamma}_{ij}$ as the flat spatial

metric η_{ij}, one can find the so-called **conformally flat metric**. This choice allows us to rewrite the surface integral of Eq. (123) as a volume integral over the whole hypersurface

$$M_{ADM} = \int_{\Sigma_t} \Psi^5 (E + \frac{1}{16\pi} K_{ij} K^{ij}) d^3x, \tag{131}$$

where E is the total energy density of matter as seen by an Eulerian observer.

In order to proceed in this decomposition, let's consider the extrinsic curvature $\boldsymbol{K}$. First of all, let's split it up into two components: a trace part obtained using $\boldsymbol{\gamma}$, and a traceless part $\boldsymbol{A}$ so to have

$$K_{ij} = A_{ij} + \frac{1}{3}\gamma_{ij} K \tag{132}$$

and then proceed by conformally decomposing the traceless part $\boldsymbol{A}$

$$A^{ij} = \Psi^p \bar{A}^{ij} \tag{133}$$

the choices of the power p are typically two:

- $p = -4$ is typically used to deal with time evolutions. Let's define the values obtained with this choice by using the symbol $\wedge$ as in $\hat{A}$.
- $p = -10$ is the natural choice to deal with the initial data problem. We will in this case use the symbol $\sim$, as in $\tilde{A}$.

By considering the former choice, it is possible to rewrite Eq. (98) using Eqs. (130) and (132)

$$\left(\frac{\partial}{\partial_t} - \mathcal{L}_\beta\right) \tilde{\gamma}^{ij} = 2\alpha \tilde{A}^{ij} + \frac{2}{3} \tilde{D}_k \beta^k \tilde{\gamma}^{ij} \tag{134}$$

where the notation $\tilde{\boldsymbol{D}}$ refers to the conformal connection (see Appendix B). Considering the power $p = -10$, it is possible to rewrite the Hamiltonian and momentum constraints, Eqs. (106) and (108), respectively as

$$\begin{cases} \tilde{D}_i \tilde{D}^i \Psi - \frac{1}{8}\tilde{R}\Psi + \frac{1}{8}\hat{A}_{ij}\hat{A}^{ij}\Psi^{-7} + (2\pi E - \frac{1}{12}K^2)\Psi^5 = 0 \\ \tilde{D}_j \tilde{A}^{ij} + 6\tilde{A}^{ij}\tilde{D}_j \ln\Psi - \frac{2}{3}\tilde{D}^i K = 8\pi\Psi^4 p^i \end{cases} \tag{135}$$

where $\tilde{R}$ is the Ricci scalar associated with the conformal metric. The former one being called **Lichnerowicz equation**, is typically interpreted as a non-linear elliptic equation for the conformal factor Ψ. Well-posedness and uniqueness of the boundary value problem for the Lichnerowicz equation have been deeply studied under the constant mean curvature condition ($K = \gamma^{ij} K_{ij} = \text{const}$). In particular, if one considers AF hypersurfaces, $K = E = 0$, the equation is solvable if and only if the metric $\tilde{\boldsymbol{\gamma}}$ is conformal to a metric with null scalar curvature, i.e. ${}^4R = 0$.

3.4.3 Conformal thin sandwich method

This method to compute ID was introduced for the first time in York (1999). The starting point of this method consists in taking Eq. (134) and solving for $\tilde{A}$. Defining $(\tilde{L}X)^{ij}$ as the **conformal Killing operator** associated with the metric $\tilde{\gamma}$ and acting on the vector field X

$$(\tilde{L}X)^{ij} = \tilde{D}^i X^j + \tilde{D}^j X^i - \frac{2}{3}\tilde{D}_k X^k \tilde{\gamma}^{ij} \tag{136}$$

(also called longitudinal part of $\hat{A}^{ij}$) and using the notation

$$\dot{\tilde{\gamma}}^{ij} = \frac{\partial}{\partial t}\tilde{\gamma}^{ij} \tag{137}$$

We can rewrite Eq. (134) as

$$\tilde{A}^{ij} = \frac{1}{2\alpha}\dot{\tilde{\gamma}}^{ij} + (\tilde{L}\beta)^{ij} \tag{138}$$

Using the relation $\hat{A}^{ij} = \Psi^6 \tilde{A}^{ij}$, we can get

$$\hat{A}^{ij} = \frac{1}{2\tilde{\alpha}}\dot{\tilde{\gamma}}^{ij} + (\tilde{L}\beta)^{ij} \tag{139}$$

where the conformal lapse $\tilde{\alpha} = \Psi^{-6}\alpha$ has been introduced. This equation represents a decomposition of $\hat{A}^{ij}$ that we can use to rewrite the Lichnerowicz equation and the momentum constraint as a new system described by

$$\begin{cases} \tilde{D}_i\tilde{D}^i\Psi - \dfrac{\tilde{R}}{8}\Psi + \dfrac{1}{8}\hat{A}_{ij}\hat{A}^{ij}\Psi^{-7} + 2\pi\tilde{E}\Psi^{-3} - \dfrac{K^2}{12}\Psi^5 = 0 \\ \tilde{D}_j\left(\dfrac{1}{\tilde{\alpha}}(\tilde{L}\beta)^{ij}\right) + \tilde{D}_j\left(\dfrac{1}{\tilde{\alpha}}\dot{\tilde{\gamma}}^{ij}\right) - \dfrac{4}{3}\Psi^6\tilde{D}^i K = 16\pi\tilde{p}^i \end{cases} \tag{140}$$

with conformal data $\tilde{E} = \Psi^8 E$ and $\tilde{p}^i = \Psi^{10} p^i$. The method to compute initial data consists therefore in choosing arbitrarily $\tilde{\gamma}_{ij}, \dot{\tilde{\gamma}}^{ij}, K, \tilde{\alpha}, \tilde{E}$ and $\tilde{p}^i$ on Σ_0 and solving the system for Ψ and β^i. As for other techniques to solve the ID problem, the conformal thin sandwich method, which takes its name from the fact that one of the parameters ($\dot{\tilde{\gamma}}^{ij}$) can be obtained from the value of the conformal metric on two neighboring slice (Σ_t and $\Sigma_{t+\delta t}$), in the case of constant mean curvature condition becomes an elliptic equation for the shift vector $\boldsymbol{\beta}$.

3.4.4 Extended conformal thin sandwich method

Considering the equations of system (140), it looks like there is no easy way to pick a value for the conformal lapse that satisfies the requirement we saw in section 3.3. Instead of choosing an arbitrary value, it was suggested in Pfeiffer and York (2003) to compute a

value out of the Einstein equation, given the time derivative of the trace of the extrinsic curvature

$$\left(\frac{\partial}{\partial t} - \mathcal{L}_\beta\right) K = -\Psi^{-4}(\tilde{D}_i\tilde{D}^i\alpha + 2\tilde{D}_i \ln\Psi \tilde{D}^i\alpha) + \alpha\left[4\pi(E+S) + \tilde{A}_{ij}\tilde{A}^{ij} + \frac{k^2}{3}\right] \quad (141)$$

This expression can be manipulated a bit using the identity

$$\tilde{D}_i\tilde{D}^i\alpha + 2\tilde{D}^i \ln\Psi \tilde{D}^i\alpha = \Psi^{-1}[\tilde{D}_i\tilde{D}^i(\alpha\Psi) + \alpha\tilde{D}_i\tilde{D}^i\Psi] \quad (142)$$

and solving the former equation of system (140) for $\tilde{D}_i\tilde{D}^i\Psi$ one can get

$$\tilde{D}_i\tilde{D}^i(\tilde{\alpha}\Psi^7) - (\tilde{\alpha}\Psi^7)\left[\frac{1}{8}\tilde{R} + \frac{5}{12}K^2\Psi^4 + \frac{7}{8}\hat{A}_{ij}\hat{A}^{ij}\Psi^{-8} + 2\pi(\tilde{E} + 2\tilde{S})\Psi^{-4}\right] + (\dot{K} - \beta^i\tilde{D}_iK)\Psi^5 = 0 \quad (143)$$

using the notation $\dot{K} := \dfrac{\partial K}{\partial t}$ and $\tilde{S} := \Psi^8 S$. Adding this equation to those of system (140), we obtain the Extended conformal thin sandwich (XCTS) system for the ID problem. This time the free data consists in the conformal metric $\tilde{\boldsymbol{\gamma}}$, its coordinate time derivative $\dot{\tilde{\boldsymbol{\gamma}}}$, the trace of the extrinsic curvature K and its coordinate time derivative $\dot{K}$ and the rescaled variables $\tilde{E}, \tilde{S}$ and $\tilde{p}^i$, while the conformal factor Ψ, the conformal lapse $\tilde{\alpha}$ and the shift vector β are constrained by the equations. This technique happens to be particularly suited to describe quasi-stationary spacetimes and it is therefore used to prepare quasi-equilibrium ID such as the one produced in chapter 4.1.

3.5 Initial data for binary systems

Constructing efficiently ID for binary systems made of compact objects is still today one of the major topics of NR. The reason for that relies on the fact that such systems constitute the main sources of detectable gravitational waves for the interferometric detectors either ground-based (LIGO, VIRGO, KAGRA) or space-based (LISA). The motion of compact bodies, entangled in a long inspiral, will eventually lead to their merging since the emission of GWs will cause the orbits to shrink. However, this effect causes also an efficient circularization of the orbits, allowing us to describe this motion as closed circular orbits. From the perspective of relativity, having exact circular orbits implies the existence of some symmetry (that in this case is called helical symmetry, Fig. 13) and of an associated killing vector $\boldsymbol{\ell}$. This can suggest a choice of coordinate such that $\boldsymbol{\partial} t = \boldsymbol{\ell}$. With this choice all fields are time independent, and in particular $\dot{\tilde{\gamma}}^{ij} = 0$ and $\dot{K} = 0$ will be our prescription for those XCTS free parameters. This assumption holds for the majority of the inspiral phase, during which the timescale under which the orbits shrink is much larger than the orbital one and so the evolution can be considered as a quasi-adiabatic process, even though strictly closed circular orbits could not be admitted in a relativistic framework, due to the emission of GWs. This concept has been used to

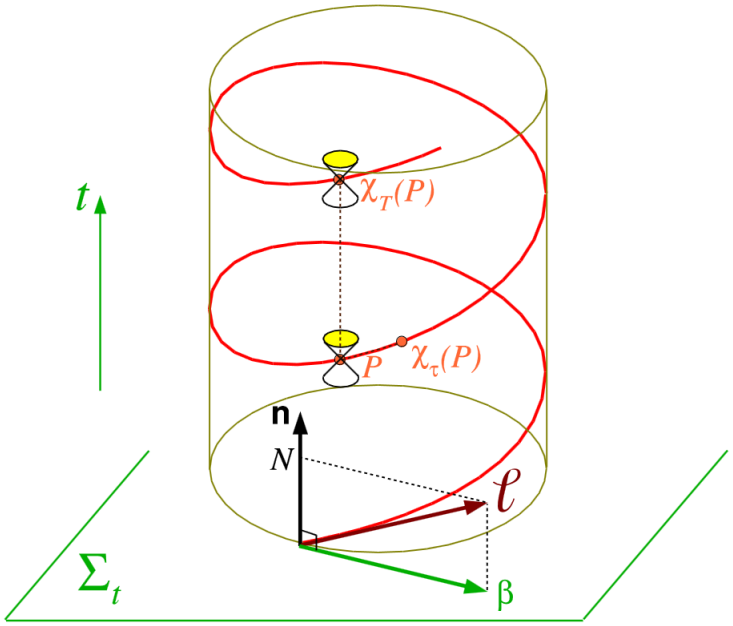

Figure 13: Action of the helical symmetry group. We can follow the displacement χ_τ of point P as it moves forward in time. With the notation N the author refers to the lapse function, and with β to the shift vector associated with coordinates adapted to the symmetry (i.e. (t, x^i) such that $\boldsymbol{\partial} t = \boldsymbol{\ell}$). Image from Gourgoulhon (2007).

generate ID for all kinds of compact binaries, however, after a certain amount of orbits, the motion will become unstable and the two bodies will collide, leading to a violation of the assumptions and the symmetries described until this point. To determine the point at which this happens, i.e. to locate the last stable circular orbit for which we can compute ID, we could study the evolution of the binding energy E_b of the system, locating its turning point. In the case of BBH systems, this quantity can be defined as

$$E_b = M_{ADM} - 2M_{BH} \tag{144}$$

where the black hole mass can be defined using the irreducible mass, see Eq. (176). Defining l as the proper separation between the two horizons (see the next section for more details), we can find the turning point as

$$\frac{\partial E_b}{\partial l} = 0 \tag{145}$$

In this case, a minimum in the binding energy corresponds to a stable quasi-circular orbit, while a maximum to an unstable orbit. The transition between these two defines the ISCO which occurs at the saddle point

$$\frac{\partial^2 E_b}{\partial l^2} = 0 \tag{146}$$

On the other hand, in the case of BNS systems, it is possible to localize the ISCO by looking for the presence of a minimum of the total energy/mass, that should coincide with a minimum in the angular momentum. Both of these techniques can be applied to look for stable orbits for BHNS systems. The evolutionary sequence in the case of BNS can end either at the ISCO, at the collision, or at the formation of a cusp on the NS surface. Differently to BHNS systems, the latter case corresponds to the inset of mass-transfer and formation of a dumbbell-like structure.

3.5.1 Black hole initial data

While describing the evolution of BHNS systems a problem arises when we come to numerically describe a BH. One could start by stating that a BH represents a certain region of the spacetime out of which no null geodesic can escape to infinity. In this sense, we could identify the presence of a BH with a certain surface, for instance the one delimited by the boundary between those events that can emit light rays visible to infinity and those that can not. This rough definition coincides with the one of the event horizon: a gauge invariant entity that contains important geometrical information. However, this happens to be a global property of the spacetime depending on past, present and future events which makes it very complicated to provide a good location: a complete knowledge of the entire future spacetime is in fact needed to decide whether or not a certain null geodesic will eventually escape or not.

Finding a good description for the surface of a BH becomes a matter of primary importance also in terms of the numerics: the singularities contained at the center of the BH must be somehow excluded from the grid to avoid spurious calculations. One technique could consist of choosing an ad hoc slicing of the spacetime, technique that however typically leads to grid's pathologies causing the code to crash. Another idea could arise from the fact that the interior of a BH can never influence the exterior: in this sense we could excise a spacetime region just inside the event horizon from the numerical grid. The problem of doing that consists in the requirement of knowing the location of the horizon for all the timesteps throughout the evolution. Since, as said, this is unachievable, one can locate an **apparent horizon**. When dealing with spherical symmetry, it is quite easy to provide a definition for this object: we define it as the boundary of smooth 2+1 surfaces embedded in spatial slices Σ_t whose outgoing null geodesic have zero expansion. This definition is local in time and can be provided on each slice. From the singularity theorems of general relativity (Hawking and Ellis, 1973) we can also say that if an apparent horizon exists on a given slice, it must be contained inside the BH's event horizon and that its area can not decrease[27]. Another issue consists of choosing the topology of the solution to be constructed. For the aim of this project, let's consider the so-called **puncture approach** (Brandt and Brügmann, 1997). We

[27]Because of this property, it is possible to define a quantity called irreducible mass. See Eq. (176).

choose as topology for Σ_0, $\mathbb{R}^3$ minus a point:

$$\Sigma_0 = \mathbb{R}^3 \backslash \{\mathcal{O}\} \tag{147}$$

the removed point $\mathcal{O}$ is named as **puncture**. The singularities in Hamiltonian constraint are with this choice absorbed in an analytical expression. This idea can be generalized to the case of multiple BHs: the starting ansatz consists of expressing the conformal factor as a generalization of the results found by Brill and Lindquist(Brill and Lindquist, 1963), introducing a correction u

$$\Psi = \Psi_{BL} + u = \sum_{h=1}^{N} \frac{M_h}{|x^i - c_h^i|} + u \tag{148}$$

where M_h is the mass of the h-th black hole and Ψ_{BL} is the same analytical factor found for the Brill-Lindiquist data and that contains the singularities located in c_h^i which are removed from the slice. Plugging this definition inside the Lichnerowicz equation we can obtain the following equation that defines u:

$$\Delta u + \frac{\hat{A}_{ij}\hat{A}^{ij}}{8\Psi_{BL}^7}\left(1 + \frac{u}{\Psi_{BL}}\right)^{-7} = 0 \tag{149}$$

with boundary conditions given by the AF requirement

$$u = 1 + \mathcal{O}(r^{-1}) \qquad \partial_r u = \frac{1-u}{r} \qquad \text{for } r \to \infty \tag{150}$$

In this way, the analytical term absorbs the BH singularity and the corrections u are regular everywhere, except at the punctures. This means that Eq. (149) can be always solved without the need to excise the BH interior from the computational grid. As for other data, the spacetime of the punctured ones presents AF region for each puncture.

3.5.2 Neutron star initial data

In order to compute ID for NSs, it is necessary to consider equation of motion for the fluids together with EFE. To consider a matter source in the equations, let's consider an energy-momentum tensor for a perfect fluid:

$$T^{\mu\nu} = (\rho_0 + \rho_i + P)u^\mu u^\nu + P g^{\mu\nu} \tag{151}$$

Here $\boldsymbol{u}$ is the four-velocity of the fluid, and ρ_0, ρ_i and P are respectively the rest-mass density, internal energy density and pressure as observed by a comoving observer. We define the specific enthalpy as

$$h = \exp\left(\int \frac{dP}{\rho_0 + \rho_i + P}\right) \tag{152}$$

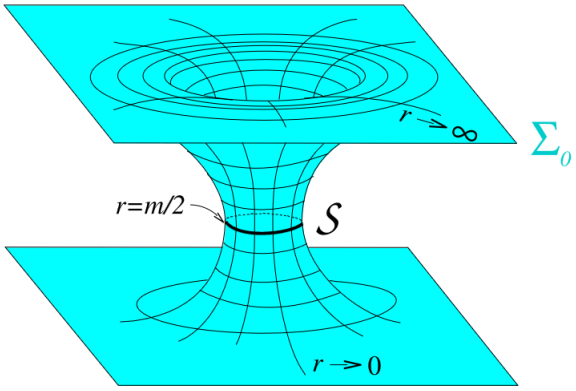

Figure 14: The wormhole topology for punctured data is the same defined by the extended hypersurface Σ_0' obtained by gluing a copy of Σ_0. The region around $\mathcal{S}$ is called **Einstein-Rosen bridge** and connects two AF regions without entering below the event horizon. The figure displays an embedding diagram based on the metric $\boldsymbol{\gamma}$. Using the punctured approach the entire N +1 wormhole topology can be represented in a single three-dimensional space $\mathbb{R}^3$, without the need to excise any region during numerical simulations. Image from Gourgoulhon (2007).

that reduces for polytropic EOS to

$$h = \frac{\rho_0 + \rho_i + P}{\rho_0} \tag{153}$$

From the equation of motion

$$\nabla_\nu T^{\mu\nu} = 0 \tag{154}$$

one can find the Euler equation

$$u^\nu \nabla_\nu (h u_\mu) + \nabla_\mu h = 0 \tag{155}$$

and the continuity equation for the rest-mass

$$\nabla_\mu (\rho_0 u^\mu) = 0 \tag{156}$$

We can now project these four-dimensional equations on the slice Σ_t. Rewriting the fluid four-velocity as $u^\mu = u^t(l^\mu + V^\mu)$ where l^μ is timelike and V^μ is purely spatial, we can rewrite Eq. (155) as

$$\gamma_i{}^\mu \mathcal{L}_{\boldsymbol{l}}(h u_\mu) + D_i(\frac{h}{u^t} + \hat{u}_j V^j) + V^j(D_j \hat{u}_i - D_i \hat{u}_j) = 0 \tag{157}$$

and Eq. (156) as

$$\alpha(\mathcal{L}_{\boldsymbol{l}}(\rho_0 u^t) + \rho_0 u^t \nabla_\mu l^\mu) + D_i(\alpha \rho_0 u^t V^i) = 0 \tag{158}$$

Here we used the notation $\hat{u}_i = \gamma_i{}^\mu h u_\mu$ as the spatial projection of hu_i. The analysis made so far, did not consider the possibility of having symmetries, however it is possible to consider l^μ as a helical killing vector simplifying furthermore[28] Eqs. (155) and (156).

3.6 Evolution schemes

We will now conclude this chapter by introducing a description of the evolution scheme used to run the simulations studied in this project. Let's start by defining the free evolution schemes as a group of techniques for integrating the 3+1 EFE in time, where the constraint equations are solved only initially to get the ID, without the need to consider them again for the subsequent time steps. In fact, fixing some choices for the lapse function and shift vector, while considering only the evolution equation (109) and the kinematical equation (98) is sufficient to reconstruct the full spacetime metric $\boldsymbol{g}$ at each time t. By doing that, however, the constraints may be violated, leading to a metric that doesn't satisfy the EFE. Nevertheless, it can be shown that if the constraints are satisfied at the initial time $t = 0$, then the dynamical equation ensures that they are satisfied for all the other $t > 0$. The scheme we will describe now, is called BSSN scheme (Shibata and Nakamura, 1995). The starting point is the conformal 3+1 Einstein system, rewritten using a Ricci tensor $\tilde{\boldsymbol{R}}$ expressed using the conformal metric $\tilde{\boldsymbol{\gamma}}$. Introducing a tensor field

$$\Delta^k{}_{ij} = \frac{1}{2}\tilde{\gamma^{kl}}(\mathcal{D}_i\tilde{\gamma}_{lj} + \mathcal{D}_j\tilde{\gamma}_{il} - \mathcal{D}_l\tilde{\gamma}_{ij}) \tag{159}$$

where $\mathcal{D}_i$ stands for the covariant derivative associated with the flat metric $\boldsymbol{f}$, we can rewrite the Ricci tensor as

$$\tilde{R}_{ij} = \frac{1}{2}\left(\tilde{\gamma}^{kl}(\mathcal{D}_k\mathcal{D}_l\tilde{\gamma}_{ij} + \tilde{\gamma}_{ik}\mathcal{D}_j\mathcal{D}_l\tilde{\gamma}^{kl} + \tilde{\gamma}_{jk}\mathcal{D}_i\mathcal{D}_l\tilde{\gamma}^{kl}\right) + \mathcal{Q}_{ij}(\boldsymbol{\gamma}, \boldsymbol{\mathcal{D}\gamma}) \tag{160}$$

where

$$\mathcal{Q}_{ij}(\boldsymbol{\gamma}, \boldsymbol{\mathcal{D}\gamma}) := -\frac{1}{2}\left(\mathcal{D}_k\tilde{\gamma}_{lj}\mathcal{D}_i\tilde{\gamma}^{kl} + \mathcal{D}_k\tilde{\gamma}_{il}\mathcal{D}_j\tilde{\gamma}^{kl} + \mathcal{D}_k\tilde{\gamma}_{kl}\mathcal{D}_l\tilde{\gamma}_{ij}\right) - \Delta^k{}_{il}\Delta^l{}_{kj} \tag{161}$$

If we now consider the Ricci tensor as a differential operator acting on $\tilde{\gamma}$, its principal part (i.e. those terms with the highest derivatives) is given by the three terms in the right-hand side of Eq. (160), involving second derivatives. In particular, considering the first term $\tilde{\gamma}^{kl}\mathcal{D}_k\mathcal{D}_l\tilde{\gamma}_{ij}$, we can find something similar to a Laplace operator acting on $\tilde{\gamma}_{ij}$. Introducing auxiliary variables, it is possible to rewrite it as a wave operator, acting on the metric coefficients. In this way it is possible to obtain a formulation which leaves free the coordinate choice, introducing new constraint and evolution equation for the auxiliary variable. An example of this procedure consists in defining as auxiliary variable

$$\tilde{\Gamma}^i = -\mathcal{D}_j\tilde{\gamma}^{ij} \tag{162}$$

[28] See chapter 9 - "Binary Neutron Stars Initial Data", Baumgarte (2003), for more details.

to rewrite the Ricci tensor as a Laplace-like operator. The evolution of $\tilde{\Gamma}^i$ is related to the evolution of the spatial coordinates x^i on each hypersurface Σ_t, which is governed by the shift vector $\boldsymbol{\beta}$, and to the choice of foliation, related to the lapse function α. The choices of the shift vector and lapse function are therefore fundamental and will determine the form of the 3+1 Einstein system to solve. We introduce as choice for α, a foliation called **1+log slicing**, where the condition for the lapse is in the form

$$\left(\partial_t - \beta^i \partial_i\right) \alpha = -2\alpha K \tag{163}$$

Foliations whose lapse function obeys this condition have a strong singularity avoidance property and therefore are widely used in BBHs simulations. The prescription for the evolution of spatial coordinates that we introduce is called **Gamma freezing**, obtained from the condition

$$\mathcal{D}_j \dot{\tilde{\gamma}}^{ij} = 0 \tag{164}$$

and, expressing the covariant derivative in terms of the Christoffel symbol $\bar{\Gamma}^i{}_{jk}$ of the metric $\boldsymbol{f}$ with respect to coordinates x^i, and defining

$$\tilde{\Gamma}^i := \tilde{\gamma}^{jk} \left(\tilde{\Gamma}^i{}_{jk} - \bar{\Gamma}^i{}_{jk}\right) \tag{165}$$

Then Eq. (164), can be rewritten as

$$\mathcal{D}_j \tilde{\gamma}^{ij} = -\tilde{\Gamma}^i \tag{166}$$

which is exactly our auxiliary variable of Eq. (162) and whose time derivative is zero: for this choice $\tilde{\boldsymbol{\Gamma}}$ does not evolve, from here the name. Writing this into a condition for the shift vector $\boldsymbol{\beta}$, one can find

$$\begin{aligned} \frac{\partial \tilde{\Gamma}^i}{\partial t} =& \tilde{\gamma}^{jk} \mathcal{D}_j \mathcal{D}_k \beta^i + \frac{1}{3} \tilde{\gamma}^{ij} \mathcal{D}_j \mathcal{D}_k \beta^k + \frac{2}{3} \tilde{\Gamma}_i \mathcal{D}_k \beta^k - \tilde{\Gamma}^k \mathcal{D}_k \beta^i + \beta^k \mathcal{D}_k \tilde{\Gamma}_i \\ & - 2\alpha \left[\pi \Psi^4 p^i - \tilde{A}^{jk} \left(\tilde{\Gamma}^i_{jk} - \tilde{\Gamma}^i_{jk}\right) - 6 \tilde{A}^{ij} \mathcal{D}_j \ln \Psi + \frac{2}{3} \tilde{\gamma}^{ij} \mathcal{D}_j K \right] - 2 \tilde{A}^{ij} \mathcal{D}_j \alpha \end{aligned} \tag{167}$$

which is exactly the evolution equation, needed for the auxiliary variable in the BSSN scheme, while Eq. (162), will be its constraint. The combination of punctured ID and BSSN evolution scheme represents the pillar of the moving puncture paradigm used by the `BAM` code, described in the next chapter.

4 Numerical methods

This chapter will be dedicated to a detailed description of the numerical tools used to develop this master's thesis project. As mentioned, high-accuracy NR simulations are today required to face the complex physics hidden within GW's observations. However, the production of this kind of codes can be very demanding, both in terms of complexity and computational costs. Their development thus follows the most sophisticated algorithms and state-of-the-art techniques. Among all possible choices, NR codes look for those algorithms that can grant a satisfactory result in terms of accuracy, reliability, and computational costs. For this reason, two main methods are nowadays adopted (Duez et al., 2008):

- Finite differences schemes: they provide a simple and easy way to describe dynamical fields. They should converge to the exact solution as some power of the grid spacing, and, together with shock-capturing techniques, can be used to evolve fluids with sharp discontinuities in a stable and accurate way. However, they require the use of large grids in order to obtain accurate results (a problem that can be partially resolved by using mesh refinement or higher-order schemes);

- Spectral methods: functions are approximated as a truncated series expansion, written in a set of orthogonal basis functions. These methods allow to solve exactly the derivatives of the approximated functions; particularly in the case of smooth problems, they show exponential convergence to the exact solution and have been shown to provide highly precise solutions in a large variety of problems from fluid dynamics to astrophysics.

We begin this chapter with a description of the production of constraint-satisfying and self-consistent ID. Being this problem of primary importance, significant efforts have been made by the NR community, leading to the development of several codes. To name a few of the most important ones: `COCAL` (Uryū and Tsokaros, 2012) is a code for constructing quasi-equilibrium spinning BBH and BNS ID on circular, but not eccentricity-reduced orbits [29]; the `FUKA` code (Papenfort et al., 2021), useful for computing eccentricity-reduced BBH, BNS, and BHNS binaries with aligned or anti-aligned spins; the public code `LORENE`[30] for quasi-equilibrium or corotational BBH, BHNS, and BNS, where only black holes can have spin (either aligned or anti-aligned). The ID solver used to construct the initial conditions for our simulations is `Elliptica` (Rashti et al., 2022), one of the

[29] Being the orbits of compact binaries nearly completely circularized just before the merger, the orbital eccentricity computed by the code should be as close as possible to zero. Even a small value of $e \approx 0.01$ in the theoretical template can significantly degrade the accuracy with which we can measure the tidal deformability. Therefore an eccentricity reduction routine is nowadays typically performed on the ID.

[30] Lorene, Langage Objet pour la RElativité NumériquE, URL `http://www.lorene.obspm.fr.`

most ductile codes available today thanks to its ability to describe compact binaries with spin vectors pointed towards arbitrary directions, based on the XCTS method. The output of this code will be then used to generate a series of quasi-equilibrium states and, by putting them together, sequences (see section 5.1). The latter give us the possibility to have a better understanding of physical interaction phenomena such as tidal effects on comparable-mass objects, and can be considered a sort of approximate model for the evolutionary path of the system. The complete evolution of these ID is then performed using the latest version of `BAM` (Brügmann et al., 2008): a NR code based on the "moving puncture" paradigm (see section 3.6) to simulate black hole spacetimes without excision, adopting finite differences schemes and "moving boxes" mesh refinement.

4.1 Constructing the initial data with `Elliptica`

As mentioned in section 3.4 and 3.5 constructing ID in NR for a given BHNS initial configuration means finding a solution for the constraint equations as well as for the Euler's equations, Eqs. (106), (108), (155). As we saw the former are obtained from Einstein's field equations, while the latter can be derived from the conservation of the stress-energy tensor. There are different forms into which these equations can be cast; the one chosen by `Elliptica` consists of a system of coupled nonlinear elliptic partial differential equations (see section 3.4.3 and 3.4.4). Furthermore, the NS's surface location is not known a priori, but it is found as a solution for an additional algebraic equation for the specific enthalpy[31](Tichy et al., 2019). These equations are then solved on a computational grid using a spectral method based on Chebyshev polynomials of the first kind (Boyd, 2001) together with a Schur complement domain decomposition method (SCDD) (Saad, 2003). However, the number of computations to be performed depends on the number of points that we consider when discretizing the domain and can become prohibitively expensive. The strategy adopted by the code to face this problem is to subdivide the domain into subsystems and to solve each of them separately. This divide-et-impera procedure allows to solve in parallel all the equations. To do that, `Elliptica` considers a grid Ω with outer-boundary $\partial\Omega$, covered by patches ($\Omega_1, \Omega_2, \Omega_3, \ldots, \Omega_s$ where s is the number of subdomains) that touch but never overlap, each of them described by their own set of coordinates (see Fig. 15). It finds the solutions on the common interfaces first where those patches are in contact to decouple the equations, and then proceeds to solve them for each patch independently.

The equations are then solved iteratively until a given stopping condition is met (e.g., the number of iterations is larger than some limit or the numerically computed value of some boundary condition exceeds a certain tolerance). The coordinate system assigned to each patch can be Cartesian or cubed spherical. In this way, it is possible

[31]The specific enthalpy can be shown to connect metric variable and matter variables, therefore knowing h means knowing the matter distribution.

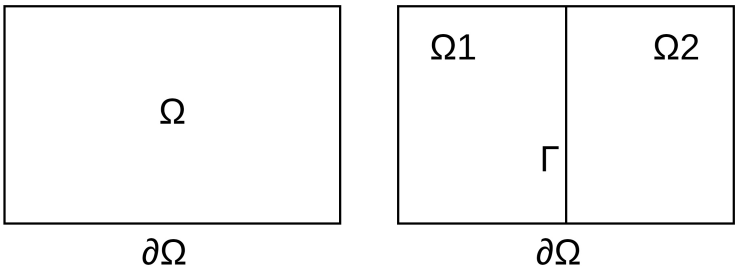

Figure 15: Visualization of a two-dimensional grid Ω, covered by two subdomains Ω_1 and Ω_2 with a single common interface Γ. Image inspired from Rashti et al. (2022).

to separate matter and vacuum region into different patches to avoid Gibbs phenomena (Boyd (2001)) in an efficient way (notice how the coordinates change inside and outside the NS surface in Fig. 16). The transformation between Cartesian Coordinates $x^i = (x, y, z)$ and cube-spherical coordinates $X^i = (X, Y, Z)$ is given by

$$X = \frac{x^I}{x^K} \tag{168}$$

$$Y = \frac{x^J}{x^K} \tag{169}$$

$$Z = \frac{x^K - r_{in}}{r_{out} - r_{in}} \tag{170}$$

where $I, J, K \in 1, 2, 3$ are all distinct and $X, Y \in [-1, 1]$, $Z \in [0, 1]$.

$$r_{\rm in} = \frac{\sigma_{\rm in}(X, Y)}{\sqrt{1 + X^2 + Y^2}} \tag{171}$$

$$r_{\rm out} = \frac{\sigma_{\rm out}(X, Y)}{\sqrt{1 + X^2 + Y^2}} \tag{172}$$

The inner and outer boundary of each patch is described by $\sigma_{\rm in}(X, Y)$ and $\sigma_{\rm out}(X, Y)$ respectively. These two values are related to Cartesian coordinates by the equation $\sigma_{\rm out}(X, Y) = \sqrt{x^2 + y^2 + z^2}$. For instance, if one requires a patch to be a perfect sphere of constant radius R_*, a boundary condition $\sigma_{\rm out}(X, Y) = R_*$ could be adopted. In this way, it is possible to choose a domain boundary that coincides with the NS surface. The possibility of using different grids opens up the availability of different setups for various purposes, including covering the NS or the space between the two bodies. It is also possible to use a Cartesian coordinates patch around the center of each spheroidal object, in order to avoid coordinates' singularities that may arise for r=0.
As one can see from Fig. 16, the BH's description for these ID follows an excision

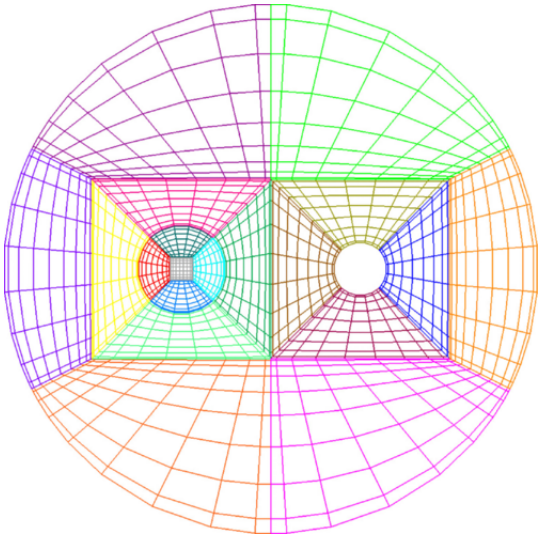

Figure 16: A computational grid implementing cubed spherical coordinates. In this image, we can see a slicing of the domains through the xy-plane and their coordinate lines. The right part of the domain covers the BH while the left one the NS. Their surfaces are both roughly spherical. Focusing on the NS one can notice how the patches form a central cube, surrounded by six cubed spheres (but only four of those are shown since we are displaying a 2d slice). Figure taken from Rashti et al. (2022).

method (see section 3.5.1): everything contained inside the AH area is removed from the computational domain and boundary conditions are imposed on the excised surface and at spatial infinity in order to have a unique physical solution. As a final note, to close the system of Einstein-Euler equations an EOS for the NS must be considered. The code supports both polytropic and piecewise polytropic EOS, see Eq. (6).

4.1.1 Parameter space investigated

In order to maximize to probability of seeing a tidal disruption scenario, the parameters of the simulations were chosen to fulfill the requirements seen in section 1.3, while maintaining canonical astrophysical values for masses and spins. Here is a list of some of the parameters that the user can specify in the parameterfile, all of them are expressed in geometric units[32] with $G = c = M_\odot = 1$.

- *The NS's baryonic mass*- Defined as

$$M_B = \int_{NS} (-J^\mu_B n_\mu)\, dV \tag{173}$$

[32]We recall the main transformation rules to move from geometric to cgs units in Appendix C.

where $-J^{\mu}_{B} n_{\mu}$ is the baryonic mass density as measured by an Eulerian observer and

$$J^{\mu}_{B} = \rho_0 u^{\mu} \tag{174}$$

is the baryonic mass density 4-current, and **u** is the fluid 4-velocity. In terms of 3+1 decomposition, this equation can be rewritten as

$$M_B = \int_{NS} \rho_0 \alpha \Psi^6 \sqrt{\gamma}\, \bar{d}^3 x \tag{175}$$

following the notation of section 3.3. The relation between the baryonic mass and the specific enthalpy is hidden in the rest mass density of the fluid ρ_0 which is actually a function of h.
The NS's baryonic mass is a conserved quantity throughout the quasi-equilibrium sequence, given the fact no mass ejection from the NS happens before the merger and the continuity equation is not violated. Given its value and an EOS, it is then possible to retrieve the gravitational mass of the isolated body using the TOV equation for nonspinning objects. In the case of the ALF2 EOS, a gravitational mass of $M_{gr} = 1.44$ is associated with the chosen value of $M_B = 1.60$, so to be consistent with the canonical NS mass value.

- *An arbitrary EOS* - In our case, ALF2, a piecewise-polytropic EOS with constants $\boldsymbol{K} = (8.95 \cdot 10^{-2},\ 2.82 \cdot 10^{8},\ 2.11 \cdot 10^{3},\ 7.43 \cdot 10)$, density threshold for different pieces $\boldsymbol{\rho_{th}} = (0,\ 3.15 \cdot 10^{-4},\ 8.11 \cdot 10^{-4},\ 1.62 \cdot 10^{-3})$ and Polytropic index $\boldsymbol{\Gamma} = (1.36,\ 4.07,\ 2.41,\ 1.89)$.

- *The NS spin vector* - During this simulations' campaign only irrotational NSs have been considered, being the most realistic ones for BHNS systems.

- *The BH's irreducible mass* - Defined as

$$M_{irr} = \sqrt{\frac{\oint_{AH} dA}{16\pi}} \tag{176}$$

where dA is the proper surface element of the apparent horizon defined as

$$dA = \sqrt{\gamma_{ij} \frac{\partial x^i}{\partial y^a} \frac{\partial x^j}{\partial y^b}} dy^a dy^b \tag{177}$$

where γ_{ij} is the 3-metric and y^a are coordinates on the apparent horizon (see section 3.5.1). This parameter was chosen with values of $M_{irr} = 3.2, 4.8, 6.4$ to have small enough mass ratios ($Q = 2, 3, 4$ respectively).

- *The dimensionless spin*

$$\chi_i := \frac{S_i}{M_{Chr}^2} \tag{178}$$

chosen with values of $\boldsymbol{\chi} = (0, 0, 0)$ and $\boldsymbol{\chi} = (0, 0, \pm 0.3)$ (so to have spin-aligned simulations). In the formula, M_{Chr} is the BH's Christodoulou mass defined as

$$M_{Chr} = \sqrt{M_{irr} + \frac{S_{BH}^2}{4M_{irr}^2}} \tag{179}$$

and S_i is the BH's spin

$$S_i = \frac{1}{8\pi} \oint_{AH} \boldsymbol{\phi}_i s^k K_{jk} dA \tag{180}$$

with K_{ij} being the extrinsic curvature, s^i the outward pointing unit normal on the excised surface, and $\boldsymbol{\phi}$ the flat space coordinate rotational Killing vector on the apparent horizon. In terms of Cartesian coordinates $x_i = (x, y, z)$, the 3 vectors $\boldsymbol{\phi_i}$ take the form

$$\boldsymbol{\phi_x} = -(z - z_c)\boldsymbol{\partial_y} + (y - y_c)\boldsymbol{\partial_z} \tag{181}$$

$$\boldsymbol{\phi_y} = +(z - z_c)\boldsymbol{\partial_x} + (x - x_c)\boldsymbol{\partial_z} \tag{182}$$

$$\boldsymbol{\phi_z} = -(y - y_c)\boldsymbol{\partial_x} + (x - x_c)\boldsymbol{\partial_y} \tag{183}$$

corresponding to a rotation about the x,y and z axis respectively and having $\boldsymbol{\partial_i}$ as the basis vectors associated with the coordinates used and $(x_c,\ y_c,\ z_c)$ as the coordinate center of the BH.

- *The BHNS coordinate distance* - This parameter was taken with values between d=62 and d=40 in order to have a fair representation of the dynamics of the inspiral and at the same time to have ideal ID to generate simulations of a few orbits before the merging, so as not to have too computationally expensive simulations but still complete waveforms.

4.1.2 Iteration

Since this code adopts an iterative method to solve the equations, initial guesses are required for the fields $\Psi, \beta_i, \alpha, \phi$, and h on the computational grid. To do that, `Elliptica` takes into account well-known analytical solutions for single objects such as the TOV solution for the NS and the Schwarzschild solution in isothropic coordinate for the BH. Having set all the parameters is then possible to solve the coupled elliptic PDEs by using a Newton-Raphson algorithm. However, there is no guarantee that the two bodies's mass and spin will converge to the target values specified in the parameter file, resulting in wrong estimations of the ID. Moreover, since the NS's surface is found by numerically

M_{irr}	M_{Chr}	$\chi_{z,BH}$	Q
3.20	3.20	0.0	2
3.20	3.24	± 0.3	2
4.80	4.80	0.0	3
4.80	4.86	± 0.3	3
6.4	6.40	0.0	4
6.4	6.47	± 0.3	4
M_B	M_{gr}	R(TOV)	$\mathcal{C}$
1.60	1.44	6.88	0.17

Table 2: Input values for the construction of the ID, the upper values refer to BH parameters while the bottom ones are related to the NS. All values are reported in geometric units with $G = c = M_\odot = 1$. The polytropic EOS is ALF2. The initial coordinate distances d = (40, 50, 52, 54, 60) in geometric units or d=(59.08, 73.85, 76.80, 79.76, 88.62) [km]

solving the algebraic equation for the enthalpy, its value will change at each iteration. This problem can be solved by finding at first the surface and then readjusting the coordinate patches so that the surface is forced to be a patch boundary. In order to overcome these possible issues, it is crucial to monitor, modify, and control various parameters at each step of the algorithm, which consists of an iterative procedure to refine the results. The code starts solving the equations at a low resolution and continues iteratively, adjusting the parameters until the chosen stopping condition is met, then increases the resolution as much as needed and solves the system of PDE again. In this way, it is possible to find a stable, unique and physical solution of the Einstein-Euler equations. The criterion used to exit the algorithm is based on the computed value of the Hamiltonian and momenta constraints (Eqs. (106) and (108), rewritten so to have all the terms at the left-hand side and zero on the right-hand side):

$$H := R - K_{ij}K^{ij} + K^2 - 16\pi E = 0 \tag{184}$$

$$M_i := D_j(K^{ij} - \gamma^{ij}K) - 8\pi j^i = 0 \tag{185}$$

When the values of H and M_i are no longer decreasing, it means they have reached the truncation error for that resolution (this behavior can be seen in Fig. 17).

The main steps of the iteration scheme to find the ID for BHNS systems are the following:

1. Solve the elliptic PDEs;
2. Update the fields;
3. Adjust BH's parameters to satisfy the target values of $\chi_{\rm BH}$ and M_{irr};

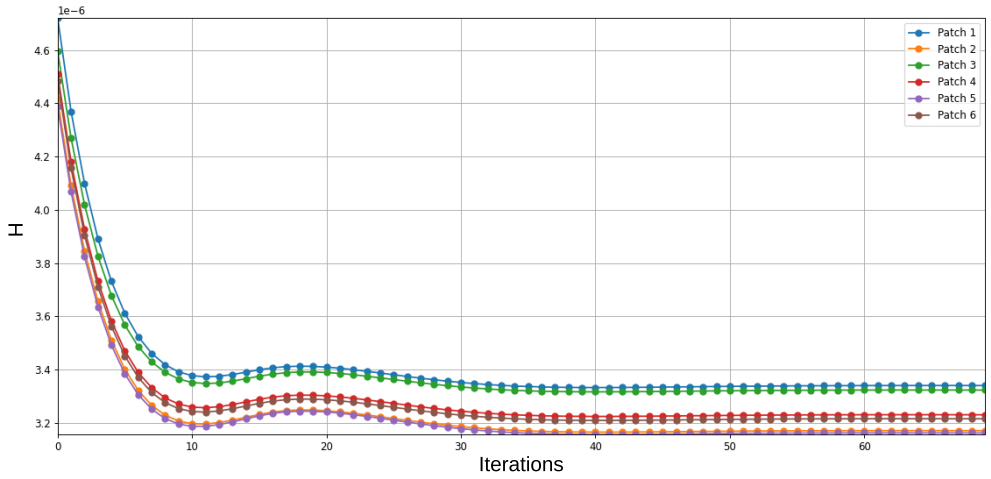

Figure 17: Evolution of the Hamiltonian constraint violation estimated in the 6 patches surrounding the BH, for a simulation with resolution 20×20×20, $M_{bar} = 1.6 M_{irr} = 6.4$, and $\chi_{z,BH} = 0$. When a sufficient amount of iterations has been performed, its value reaches the truncation error and therefore a plateau appears in the plot.

4. Solve Euler's equation to fix the NS baryonic mass;
5. Update the enthalpy;
6. Extrapolate the matter fields ϕ, w^i and h outside the NS;
7. Shift the matter to keep the NS's center fixed;
8. Find the new location of NS's surface by solving for r the equation;

$$h(r) = 1 \tag{186}$$

   this will determine the value of $\sigma(X, Y)$, seen in 4.1;
9. Create a new grid and interpolate the fields' values from the previous grid;
10. If constraints have plateaued exit or increase the resolution, otherwise go back to 1.

The maximum resolution considered depends on how large is the maximum error on the constraint we tolerate. The number of iterations used during this project is 200 at the lowest resolution (12 points per direction per patch) and 70 for the highest (20 points per direction per patch), for some simulations it was necessary to increase the maximum

resolution to 22 points with 30 iterations so to achieve better results. These simulations were performed on the HPC- Cluster ARA[33], on a single Intel Xeon node with 36 cores, and took $\approx$ 96 hours of actual wall clock time, reaching $\approx$ 140 hours for those with higher resolution.

4.1.3 Diagnostic

We conclude this section on `Elliptica` by verifying the exponential convergence expected by this spectral code. Let's consider the violation of the Hamiltonian and momentum constraints. Fig. 18 shows the L^2 norm[34] of Eqs. (184) and (185). The violation of these constraints decays exponentially for all the simulations. However, this can happen at different paces, in particular for those patches close to the BH where quantities are more difficult to estimate, it could be necessary to increase the resolution or the number of iterations to achieve a better result. In Fig. 19, the final values of the binding energy are represented per each resolution considered. As one can notice the values for the highest resolutions(e.g. 16, 18, 20) tend to oscillate around an equilibrium value. For this reason, the errors on this quantity are estimated as an arithmetic mean of the

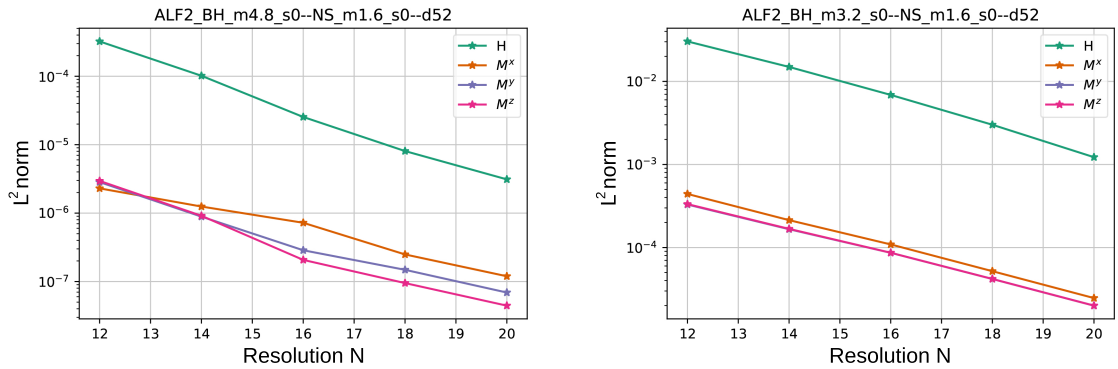

Figure 18: Spectral convergence of the Hamiltonian and momentum constraint as function of the resolution. On the vertical axis we can see the value of the L^2 norm of each constraint: we could consider it as a sort of residual between the numerically computed result and the theoretical value we wish to obtain. In the right panel, we can see how the violation of the constraints is still too high with resolution 20. For this simulation was therefore necessary to increase the points per direction to 22. Patch considered: left frontal around NS (right panel), and right frontal around BH (left panel).

[33]A description of this facility can be found at `https://wiki.uni-jena.de/pages/viewpage.action?pageId=22453005`, access date: 13 October 2023

[34]The L^2 norm of a quantity q is defined as $|q|_2 = \sqrt{\frac{\sum_{i=1}^{N} q_i^2}{N}}$ where the summation considers all grid points that contain valid data.

relative differences between the last three higher resolutions. It is also interesting to notice how the fluctuations can become larger both as the coordinate distance increases or decreases significantly. This effect can be due to a relaxation of the hypothesis on which the ID are built: objects that are not enough separated from each other cannot be completely described on an AF spacetime, nor considered as isolated. On the other hand, simulations with a too large spacing will go through a degradation of the resolution on those patches which not located around the bodies.

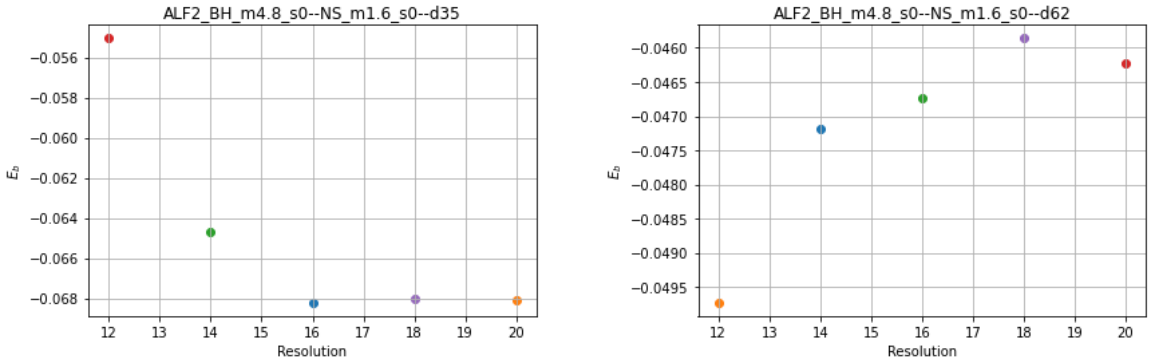

Figure 19: Final value obtained for the binding energy at different resolutions. The iteration scheme adopted is 12(×200), 14(×100), 16(×100), 18(×100), 20(×70) per direction per patch. Parameters of the simulations $M_{bar} = 1.6$ $M_{irr} = 4.8$, $\chi_{z,BH} = 0$
, and coordinates separation $d = 35$ (left panel) and $d = 62$ (right panel).

4.2 Evolving the data with `BAM`

Once the ID production has been concluded, the following step involves evolving those data. To do this, we adopted the latest version of the `BAM` code, initially proposed in Brügmann et al. (2004) and furthermore updated in Brügmann et al. (2008), Thierfelder et al. (2011), and Dietrich et al. (2015). This code exploits a different description of the BH's interior: while for `Elliptica` an excision method was employed, `BAM` adopts a moving-puncture gauge. Solving this incompatibility requires an ad hoc technique to fill the empty BH's interior with arbitrary smooth data (at least C^2 across the AH). It can be shown (Brown et al., 2007) that any constraint violations introduced inside the black holes cannot affect the exterior spacetime, therefore we can robustly exploit a seventh-order polynomial extrapolation of all the field values, using radial uniform points, for $r \geq r_{AH}$. However, this ID reading procedure is not as straightforward as one may think, and the technique explained above can be quite demanding in terms of computational resources.

The code works by splitting the computational domain into hierarchical cells, nested inside each other, using Cartesian grids with an increasing refinement factor of 2. This

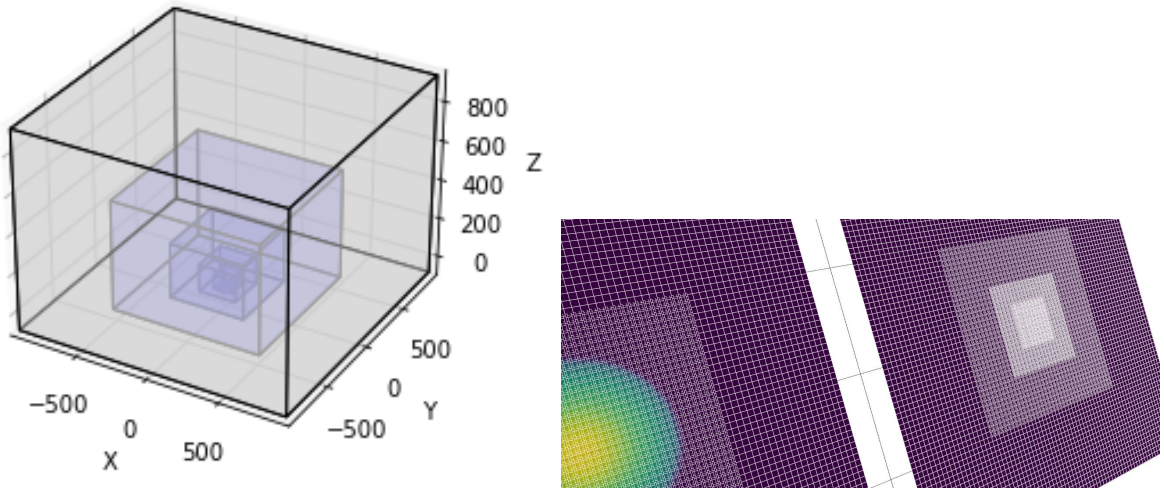

Figure 20: Grid structure for simulations using $l_{mv} = 4$. **Left panel**: Three-dimensional plot showing $l = 0, 1, 2, 3, 4$. The outermost boxes used by `BAM` are static cubes centered on the origin. **Right panel:** 2-dimensional snapshot showing the density field of the simulation (n_{mv}=64, BH finest refinement level $l = 8$, NS finest refinement level $l = 6$). Only levels $l = 5, 6, 7, 8$ are displayed: in this way, it is possible to notice how the finest levels are centered on the two compact bodies. As one can notice, between consecutive levels the size is halved, while the grid spacing is doubled, therefore the number of points n_{mv} remains constant

means that each level of refinement (labeled from $l = 0$ being the coarsest, outermost one, to $l = L - 1$ being the finest one) will have its own Cartesian grid with a given spacing $h_l = h_0/2^l$ (where h_0 is the grid spacing in the outermost level). The domain decomposition performed with this approach is such that the coordinate extension of any level l, will be completely covered by the one of level $l - 1$ (right panel of Fig. 20). The user is allowed to consider the innermost levels centered on the BH and NS respectively, while the outermost can be centered on the center of mass frame origin as long as the hierarchy is followed. In this way, the resolution of the simulation will be maximal close to the compact bodies, and minimal at spatial infinity, avoiding the waste of computational resources.

Refinement levels above a given user-defined threshold l_{mv}, have the possibility to be dynamically moved and modified, as to follow the orbits of the two objects, adopting a "moving boxes" technique. A usual choice for that consists in taking as static the outermost ones so to avoid unnecessary grid motion. Specifically, the code creates boxes with n_l points per direction (for a total of n_l^3 points on level l) which are allowed to move, always remaining contained inside the parent level. In order to obtain this, those

levels that are static will require a slightly larger box in order to contain the moving ones, from now on the points associated with the moving levels will be referred to as n_{mv}, while the notation n will be associated to static points[35]. Typically these boxes are cubical on the finest levels and follow the motion of the two bodies. However, as they overlap, the code replaces them using the associated bounding box, which is the smallest rectangular (in general non-cubical) box containing the two original ones (Fig. 21). A typical initial configuration for a binary system consists of two separate cubical boxes, located on the finest levels available on each object, but as we consider coarser levels, their size increases until overlapping, and a single rectangular box is formed, becoming more and more cubical as we move toward $l = 0$ (left panel of Fig. 20). The variables are then discretized at the center of each grid cell. This means that, on level 0, with spacing h_0, the value of the considered function will be estimated in $h_0/2 + j$ (with j being an integer number), on level 1 it will be $h_1/2+j = h_0/4+j$, on level 2 at $h_2/2+j = h_0/8+j$ and so forth. The data is then transferred between levels using a sixth-order polynomial interpolation and spatial derivatives are computed using fourth-order finite differences. In order to reduce the computational costs of these simulations, a bitant symmetry (i.e. reflection along the z=0 plane) is implemented. Time evolution is performed by adopting explicit 4th-order Runge-Kutta schemes, together with a Berger-Oliger type adaptive mesh refinement (AMR) (Berger and Oliger, 1984) to increase its efficiency. Its algorithm consists in choosing a user-defined level l_{BG} and dividing by a half the value of the time-step for each level above l_{BG}. Here's an example of a Berger-Oliger time stepping procedure for the first iteration performed on a grid with 8 refinement levels, $l_{BG} = 6$, $h_0 = 8$.

```
level  iter  tstep      h
  0      1    1.6e-01   8.000e+01
   1     1    1.6e-01   4.000e+01
    2    1    1.6e-01   2.000e+01
     3   1    1.6e-01   1.000e+01
      4  1    1.6e-01   5.000e+00
       5 1    1.6e-01   2.500e+00
        6 1   1.6e-01   1.250e+00
         7 1  7.8e-02   6.250e-01
          8 1 3.9e-02   3.125e-01
          8 1 3.9e-02   3.125e-01
         7 1  7.8e-02   6.250e-01
          8 1 3.9e-02   3.125e-01
          8 1 3.9e-02   3.125e-01
```

[35]Being $n \geq n_{mv}$ always, the value of l_{mv} can impact significantly the computational costs. The user should therefore consider the trade-off between unnecessary motion and unnecessarily larger boxes before choosing this parameter.

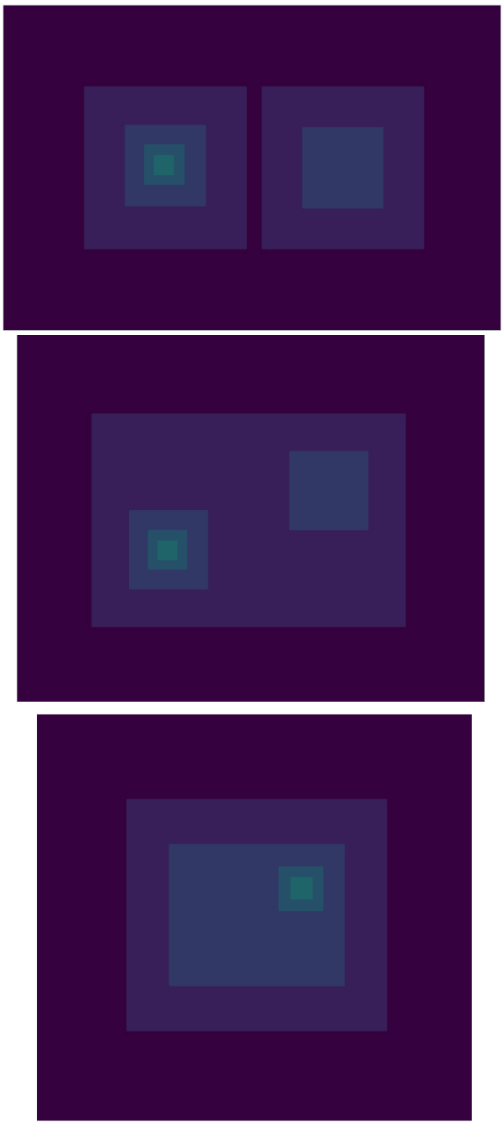

Figure 21: Snapshot of moving boxes structure for a simulation with 8 refinement levels on the BH and 6 on the NS. In the three panels, we can see the structure of the boxes on moving levels $l = 4, 5, 6, 7, 8$. While at the beginning of the simulations the moving boxes are independent cubes, as they overlap, the code replaces them with the smallest rectangular box containing the two initial boxes. This happens first for the boxes on level 5 (second panel), and then for the boxes on level 6 (third panel). Noteworthy is the shape of level 4 which moves from being rectangular to cubical as the simulation evolves.

4.2.1 Hydro-Scheme

To describe the evolution of the matter field, the code solves for the general-relativistic hydrodynamics (GRHD) equations (see section 3.5.2) in first-order flux-conservative form [36], so that:

$$\partial_t \mathbf{q} = -\partial_i \mathbf{f}^i(\boldsymbol{q}) + \mathbf{s}(\boldsymbol{q}) \tag{187}$$

where $\boldsymbol{q} = \sqrt{\{\gamma\{D, S_i, \tau)\}}$ being the vector of the Eulerian conservative variables defined in terms of the primitive variables as

$$D = W\rho, \qquad S_i = W^2 \rho h v_i, \qquad \tau = (W^2 \rho h - p) - D \tag{188}$$

where D is the rest-mass density, S_i is the momentum density and τ is the internal energy as viewed by an Eulerian observer. The primitive variables are the rest-mass density ρ, the pressure p, the specific internal energy ϵ, and the 3-velocity v_i of the fluid (considered as perfect and simple, i.e. made of just one particle's species). Additionally, we define the Lorentz factor $W = 1/\sqrt{1 - v_i v^i}$, the specific enthalpy $h = 1 + \epsilon + p/\rho$, and the determinant of the 3-metric γ. The associated flux $\mathbf{f}(\mathbf{q})$ along direction i are then defined as

$$\boldsymbol{f}^i = \sqrt{-g}\left\{ D\left(v_i - \frac{\beta^i}{\alpha}\right), \qquad S_k\left(v^i - \frac{\beta^i}{\alpha}\right) + p\delta^i_k, \qquad \tau\left(v^i - \frac{\beta^i}{\alpha}\right) + pv^i \right\} \tag{189}$$

while the source term is given by

$$\begin{aligned} \boldsymbol{s} = \sqrt{-g}\Bigg\{ 0, \qquad & T^{00}\left(\frac{1}{2}\beta^i\beta^j\partial_k\gamma_{ij} - \alpha\partial_k\alpha\right) + T^{0i}\beta^j\partial_k\gamma_{ij} + T^0_i\partial_k\beta^i + \frac{1}{2}T^{ij}\partial_k\gamma_{ij}, \\ & T^{00}\beta^i\beta^j K_{ij} - \beta^i\partial_i\alpha + T^{0i}\left(2\beta^j K_{ij} - \partial_i\alpha\right) + T^{ij}K_{ij} \Bigg\} \end{aligned} \tag{190}$$

and is finite even in the presence of physical shocks since it is not related to any derivative of the fluid variables. Moreover, all of its component vanish in the case of a flat spacetime described by Cartesian coordinates. However, in general, among the four equations of the system (187), only the first one is a conservation law

$$\partial_t \mathbf{q}^{(D)} + \partial_i \mathbf{f}^{(D)i} = 0 \tag{191}$$

being the source term always zero, we associate a conserved quantity: the baryonic (or rest-) mass M_b here defined as

$$M_b = \int d^3 q^D = \int d^3\sqrt{\gamma} D \tag{192}$$

[36] Rezzolla and Zanotti (2013), for references.

This quantity should remain constant on each level and could be used to test the performance of the conservative AMR scheme. As a matter of fact, one of the main problems of simulating hydrodynamical flows with AMR techniques is to ensure the global conservation of mass even in the presence of shocks, contact discontinuities, or sharp gradients. For this reason, the code adopts a high-resolution-shock-capturing method (Martí and Müller, 1999) based on primitive reconstruction, performed using 4th-order WENO scheme (Borges et al., 2008), and the Local-Lax-Friedrich's (LLF) central scheme for the numerical fluxes in a similar way to what was done in Zanna and Bucciantini (2002). Considering the semi-discretized description[37] of Eq. (187) along the x direction only:

$$\frac{d\boldsymbol{q_{i,j,k}}}{dt} = \boldsymbol{s_i} + \frac{1}{h}\left(\boldsymbol{F}_{i-\frac{1}{2},j,k} - \boldsymbol{F}_{i+\frac{1}{2},j,k}\right) \tag{193}$$

where h is the grid spacing and $\mathbf{F}$ are the numerical flux, or better, high-order approximations to the primitives of physical fluxes. This means that cell averages of the $\mathbf{F}(\mathbf{x})$ function must coincide with point values $\boldsymbol{f}_{i,j,k}$ of the flux function $\mathbf{f}(\mathbf{x})$ ($\boldsymbol{F}_{i\pm\frac{1}{2},j,k} = \boldsymbol{f}_{i\pm\frac{1}{2},j,k}$). These equations are then integrated in time using a 4th order Runge-Kutta method. This explicit time-advancing scheme is stable under the Courant-Friedrichs-Lewy condition $c < 1$, therefore, a canonical value of 0.25 was chosen for this factor. For every Runge-Kutta cycle and for every direction the code has to reconstruct the primitive variables from the conservative ones and to define the numerical fluxes on the cells' interfaces. We report here the principal steps of this procedure:

1. Retrieve primitive variables from conservative ones:

$$\{\boldsymbol{q}_i\} \to \{\boldsymbol{p}_i\} \qquad i = 1, 2, \ldots, N$$

2. Reconstruct the primitive variables at cell interfaces (both right and left):

$$\{\boldsymbol{p}_i\} \to \{\boldsymbol{p}^L_{i+1/2}\}, \{\boldsymbol{p}^R_{i+1/2}\} \qquad i = 0, 2, \ldots, N$$

3. Solve the Riemann problem at each inter-cell point. In this project, the fluxes $\boldsymbol{f}_{i+1/2}$ are computed using LLF as Riemann solver so that

$$\boldsymbol{f}^{\mathrm{LLF},}_{i+\frac{1}{2}} = \frac{1}{2h}\left(\boldsymbol{f}_L + \boldsymbol{f}_R - a(\boldsymbol{q}_L - \boldsymbol{q}_R)\right) \tag{194}$$

   The parameter a is the maximum of the local characteristic speed and the labels L and R stand for Left and Right interface respectively.

4. Calculate the derivative.

[37] That is to say keeping continuous time dependency in spatially discretized quantities.

The different elements of the algorithm used to evolve hydro-dynamical variables contribute differently to the error budget: while some errors converge rapidly, others tend to dominate. According to previous results (Thierfelder et al., 2011), the overall error is expected to be dominated by the truncation error of the finite differences: in this case the matter high-resolution-shock-capturing scheme is at most 2nd order accurate. In this way the evolved fields and those relevant post-processed quantities such as the gravitational waves and the constraints, are expected to reach the continuum solution with a 2nd order convergency rate. Another problem may arise from the description of low-density material characterizing accretion disks and dynamical ejecta. In particular, the latter can be significantly challenging to calculate on a grid, being their densities several orders of magnitude smaller than the typical NS maximum density (see section 5.5).

Related to that is the problematic description of vacuum regions outside the stars. Formally the GRHD equation can not be applied here and at the same time the numerical algorithm can not be used since the equations necessary to recover the primitives from the conservatives are singular: this makes the description of vacuum around the NS problematic already at a Newtonian level. A standard method to face this problem is to replace the vacuum with a minimal atmosphere characterized by a density several orders of magnitude smaller than the typical density of the system. The main assumption behind this technique is that, being the atmosphere's density extremely small, it will have a negligible dynamical impact and, as a matter of fact, we found it sufficiently robust for our purposes. However, this description could in principle lead to the violation of mass conservation and could potentially invalidate the improvements related to conservative AMR. Following Thierfelder et al. (2011), a low-density static and barotropic atmosphere was used with density

$$\rho_{atm} = f_{atm} \cdot \max[\rho(t=0)] \tag{195}$$

In this way, a point is set to the atmosphere if its density is below the threshold

$$\rho_{thr} = f_{thr} \cdot \rho_{atm} \tag{196}$$

The values used for this project are $f_{thr} = 100$ and $\rho_{atm} = 10 \cdot 10^{-10}$.

4.2.2 Gravitational wave extraction

The extraction of physical information from NR simulations is typically a non-trivial task. The reasons for that are essentially two: the numerically computed functions are coordinates dependent, and, secondly, we must be sure to define in a general relativistic framework, in an unambiguous way, those quantities typically used to describe local systems in other areas of physics. For the problem that we have to face, the most important quantities to be extracted are the energy and momenta carried away by the emission of GWs and their precise shape as seen by a detector at a large distance from

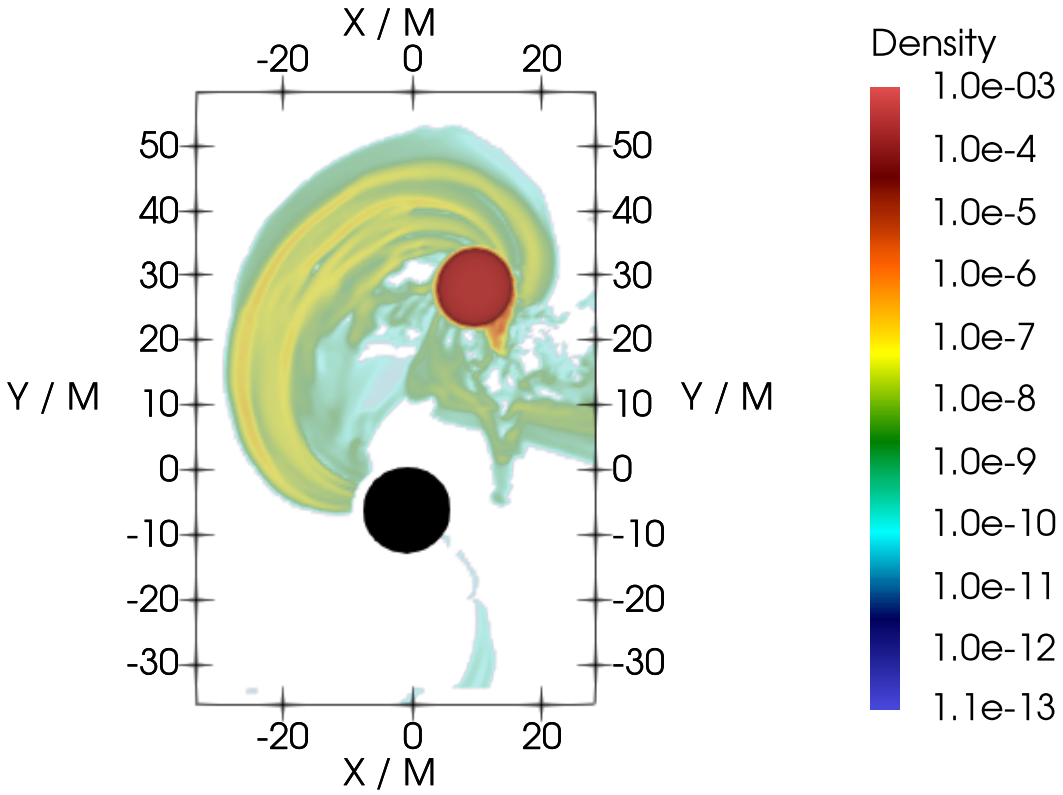

Figure 22: Qualitative plot to provide a visualization of the complicated description of the atmosphere. Simulation with $n_{mv} = 128$, LLF scheme. The density is reported in geometric units. A spurious emission of particles is happening during the evolution without affecting substantially the results.

the binary system. The method adopted to extract these quantities was based on the Newman-Penrose approach (see section 2.2.3), the code will thus focus its effort on the calculation of the Newman-Penrose scalar ψ_4. It starts by assuming known values for the ADM variables g_{ij} and K_{ij} on a given hypersurface Σ_t, then constructs a triad of orthonormal spatial vectors by applying the Gram-Schmidt orthonormalization procedure to the three-dimensional vectors

$$\begin{aligned} u_i &= (-y, x, 0), \\ v_i &= (x, y, z), \\ w_i &= g^{ia}\varepsilon_{abc}u^a v^b \end{aligned}$$

with ε_{abc} being the permutation tensor. The tetrad vectors are then

$$\begin{aligned} n^0 &= \sqrt{\frac{1}{2\alpha}}\left(\frac{-\beta^i}{\alpha} - v^i\right), \\ l^0 &= \sqrt{\frac{1}{2\alpha}}\left(\frac{-\beta^i}{\alpha} + v^i\right), \\ m^0 &= 0, \end{aligned} \qquad \begin{aligned} n^i &= \frac{1}{\sqrt{2}}\left(\frac{-\beta^i}{\alpha} + v^i\right), \\ l^i &= \frac{1}{\sqrt{2}}\left(\frac{-\beta^i}{\alpha} - v^i\right), \\ m^i &= \frac{1}{\sqrt{2}}\left(u^i + iw^i\right). \end{aligned}$$

The next step consists in defining the ψ_4 scalar in terms of the three-dimensional quantities available on each slice. This can be done using the Gauss-Codazzi equations (see section 3.3) which relate the spacetime projections of the four-dimensional Riemann tensor to its three-dimensional counterpart and to the ADM variables. The contribution of each mode (ℓ, m) is then obtained by projecting it onto -2 spin-weighted spherical harmonics $Y^{-2}_{\ell m}$. These projections are defined using a scalar product

$$A_{\ell m} = \langle Y^{-2}_{\ell m}, \quad \psi_4 \rangle = \int_0^{2\pi}\int_0^{\pi} \psi_4 \overline{Y^{-2}_{\ell m}} \sin\theta \, d\theta \, d\phi \tag{197}$$

the integrand is evaluated on the Cartesian grid and interpolated onto a sphere of radius r_{ext} (from now on called extraction radius) using fifth-order polynomials. The spherical integration is performed using the fourth-order Simpson method. Furthermore, it is possible to define the energy and momenta radiated away in terms of the ψ_4 scalar using

the expressions:

$$\frac{dE}{dt} = \lim_{r\to\infty}\left[\frac{r^2}{16\pi}\int_\Omega\int_{-\infty}^{t}|\psi_4\tilde{dt}|^2 d\Omega\right], \tag{198}$$

$$\frac{dP_i}{dt} = -\lim_{r\to\infty}\left[\frac{r^2}{16\pi}\int_\Omega \ell_i\int_{-\infty}^{t}|\psi_4\tilde{dt}|^2 d\Omega\right], \tag{199}$$

$$\frac{dJ_z}{dt} = -\lim_{r\to\infty}\left\{\frac{r^2}{16\pi}\,\mathrm{Re}\left[\int_\Omega\left(\partial\phi\int_{-\infty}^{t}\psi_4\tilde{dt}\right)\left(\int_\infty^{t}\int_{-\infty}^{\tilde{t}}\psi_4\,\tilde{dt}\hat{dt}\right)d\Omega\right]\right\} \tag{200}$$

where

$$\ell_i = (-\sin\theta\cos\phi, -\sin\theta\sin\phi, -\cos\phi) \tag{201}$$

and can be simplified using Eq. (197):

$$\frac{dE}{dt} = \lim_{r\to\infty}\left[\frac{r^2}{16\pi}\left|\int_{-\infty}^{t}\sum_{lm}A_{lm}\tilde{dt}\right|^2\right] \tag{202}$$

In particular, from this formula, one can study the energy radiated away by an individual mode by using only one term inside the summation. The results of this analysis can be found in section 5.3.

4.2.3 Ejecta

The coalescence of compact binaries involving NSs is characterized by the emission of relativistic particles, whose energy is sufficient to leave the gravitational system (Li and Paczyński, 1998). The code identifies these particles as the fluid's elements that satisfy:

$$u_t < 1 \qquad \text{and} \qquad \bar{v}_r = v^i x_i > 0 \tag{203}$$

where $u_t = -W(\alpha - \beta_i v^i)$ is the first lower component of the fluid 4-velocity, and $x_i = (x, y, z)$ so that the first condition is obtained for fluid elements following geodesics and requires that the associated orbit is unbound, while the second requires that the material has an outward-pointing radial velocity. Integrating those fluid elements that satisfy this condition, one can calculate the unbound mass from the baryonic rest mass

$$M_{ej}^{\mathcal{V}} = \int_{\mathcal{U}} q^{(D)} d^3x \tag{204}$$

where the region of integration is defined as

$$\mathcal{U} = x_i = (x, y, z) : u_t < -1 \qquad \text{and} \qquad v_r > 0 \tag{205}$$

A possible draw-back is that the ejected material could decompress and obtain densities of the order of the artificial atmosphere. If this is the case, then the fluid particles will not be included in the computation of the dynamical ejecta any longer and their mass will be possibly underestimated. Another method implemented in `BAM` consists in computing the ejecta mass through the matter flux across a coordinate sphere. In this way this effect is reduced since the decompression of material outside the sphere does not impact the computation of the mass:

$$M_{ej}^{\mathcal{S}} = \int_0^t dt' \int_{r=r_s} [D_u(\alpha v^i + \beta^i) n_i] r^2 d\Omega \tag{206}$$

where $n_i = x_i/r$ with $r = \sqrt{x_i x^i}$ and D_u denotes the unbound fraction of conserved rest mass density D. The ejecta computed by `BAM` do not take into account the chemical composition, the presence of neutrinos, or magnetic pressure. Therefore, they can not be used to make assumptions related to the microphysics of the system or to the galactic abundances. The only two quantities typically described in the literature are their masses and velocities which can be therefore used to estimate the lightcurve of an EM radiation (Chaurasia et al., 2018).

4.3 Diagnostic

4.3.1 Waveform accuracy

The accuracy with which GWs are computed relies on a series of different factors. Among the most relevant sources of uncertainties, we have the truncation error of the numerical scheme and the fact GWs are extracted at a finite radius (Bernuzzi et al., 2012). There are other aspects that however could have an impact on the computation of the waveforms such as the number of orbits, and the presence of residual eccentricity in quasi-circular ID. This analysis has been performed by changing grid's parameters such as the resolution and the number of refinement levels on the BH. As typically done in literature, the waveforms are obtained by reconstructing the multipolar modes $h_{\ell m}$. Following Reisswig and Pollney (2011), it is possible to show that the strain and the ψ_4 are related by:

$$h = h_+ - i h_\times = \int_{-\infty}^{t} dt' \int_{-\infty}^{t'} dt'' \psi_4 \tag{207}$$

being $\ddot{h}_{\ell m} = \psi_{\ell m}$. Each mode $h_{\ell m}$ is then decomposed in amplitude $A_{\ell m}$ and phase $\phi_{\ell m}$ as:

$$h_{\ell m}(t) = A_{\ell m}(t) e^{-i\phi_{\ell m}(t} \tag{208}$$

Another relevant quantity in this analysis is the time at which the compact bodies merge, defined as the moment in which the maximum value of the amplitude $A_{22}(t)$ occurs. As

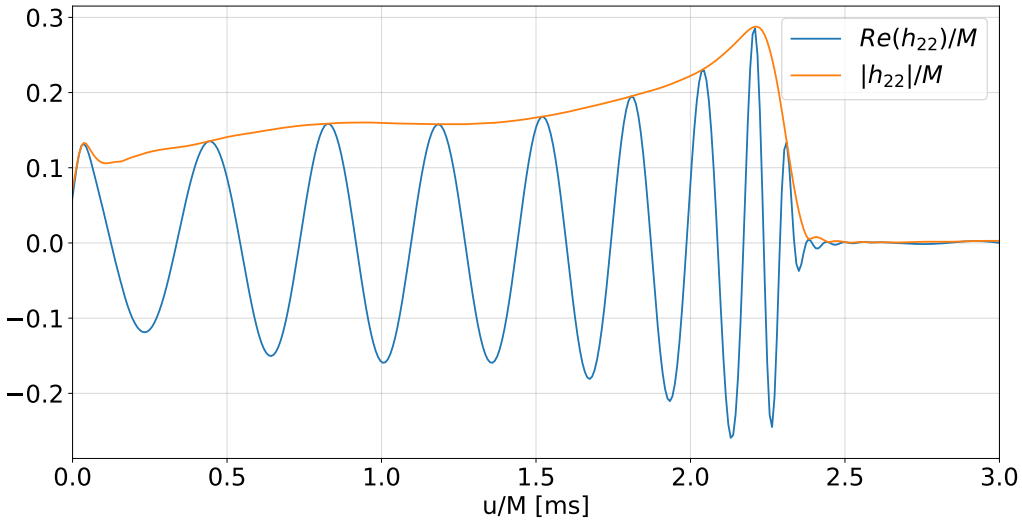

Figure 23: Real part (blue line) of the $\ell = 2, m = 2$ mode for a simulation with $Q = 2$, res=96 and 8 refinement levels. On top of it, the amplitude is represented as a yellow solid line. The presence of some eccentricity in the ID explains the non-perfectly monotonical behavior typical of chirp-like signals.

one can see from the plots (Fig. 24) its value is significantly dependent on the resolution of the simulation, meaning that the physics of the coalescence can vary with the value of n_{mv} for a not convergent series of simulations. All quantities in this section are expressed in terms of the retarded time u, defined as

$$u = t - \left[r_{ext} + 2M \ln\left(\frac{r_{ext}}{2M} - 1\right)\right] \tag{209}$$

where M is given by the sum of the gravitational masses of the two bodies. The expected waveform is characterized by the chirp-like shape typical of quasi-circular inspirals, followed by a ringdown. However, the presence of some leftover eccentricity in the data may affect the amplitude of the signal in the early time (see Fig. 23). This could lead to parameter biases if one uses the resulting waveform during a GW analysis, and should therefore be removed using an eccentricity reduction routine. However, this procedure was not performed during this project due to the restricted amount of time at disposal. The analysis of the waveform's accuracy is typically performed by considering both phase and amplitude plots at different resolutions and extraction radii using a minimum of three simulations at different grid resolutions. Using the data from `BAM`, several authors found second-order convergence e.g. Bernuzzi and Dietrich (2016), using $n_{mv} = 96, 128, 192$. However, performing simulations with this level of resolution exceeds the resources available for this project, therefore we restricted the maximal level of res-

olution using $n_{mv} = 64, 96, 128$ even though simulations with $n_{mv} = 64$ are known to be too low quality to show second-order convergence, and therefore should be discarded. The production of a convergence series is therefore left as a possible follow-up for this project. In this respect, the available data can be used to compare the cost and the quality of different configurations.

Once the data are available, the convergency rate p can be found experimentally by using a scaling factor SF (Bernuzzi et al. (2012))

$$SF = \frac{\Delta_L^p - \Delta_M^p}{\Delta_M^p - \Delta_H^p} \tag{210}$$

Where L, M, H stands for low, medium, and high resolution and Δ_x is the grid spacing at resolution x. These differences should decrease with increasing resolutions (as expected from convergent data), but should also increase for longer simulations, being the truncation error accumulated over multiple iterations. Once convergence has been proved, the error assigned to the highest resolution data is given by the difference between those data with the highest quality. However, with the best data available (n_{mv}=64, 96, 128 and 8 refinement levels on the BH) only a convergence rate $p = 7$ was found, corresponding to a scaling factor $SF(7) = 18.56$. These results can be seen in Fig. 25.

To determine the effects of extracting the waves at finite radii r_i, we can compare the differences in amplitude and phase between consecutive radii so that

$$\Delta\phi_{22}(r_i) = \phi_{22}(r_i) - \phi_{22}(r_i - 1) \tag{211}$$

and the same for the amplitudes. By plotting these quantities, it is possible to notice how these waveforms converge at spatial infinity. Moreover, the phase differences are larger at early times and decrease towards the merger, pointing out an opposite trend if compared to resolution effects where phase differences increase approaching the merging time (see Fig. 25). In Fig. 26, we can see the plot of these quantities, estimated for radii $r = 300, 400, 500, 600, 700, 800, 900 M_\odot$ for a simulation with $n_{mv} = 64$ and 6 refinement level. Even if this simulation has the lowest quality configuration, the convergence of these quantities is well visible, with relative differences in amplitude around 10^{-3} for the majority of the radii.

The total error budget can then be computed as the sum in quadrature of the truncation and finite extraction errors. As a closure note, it is important to mention that being the waveform detected at a very large distance from the production region, a subsequent procedure consists of extrapolating the simulated waveforms at null infinity (Lousto et al., 2010).

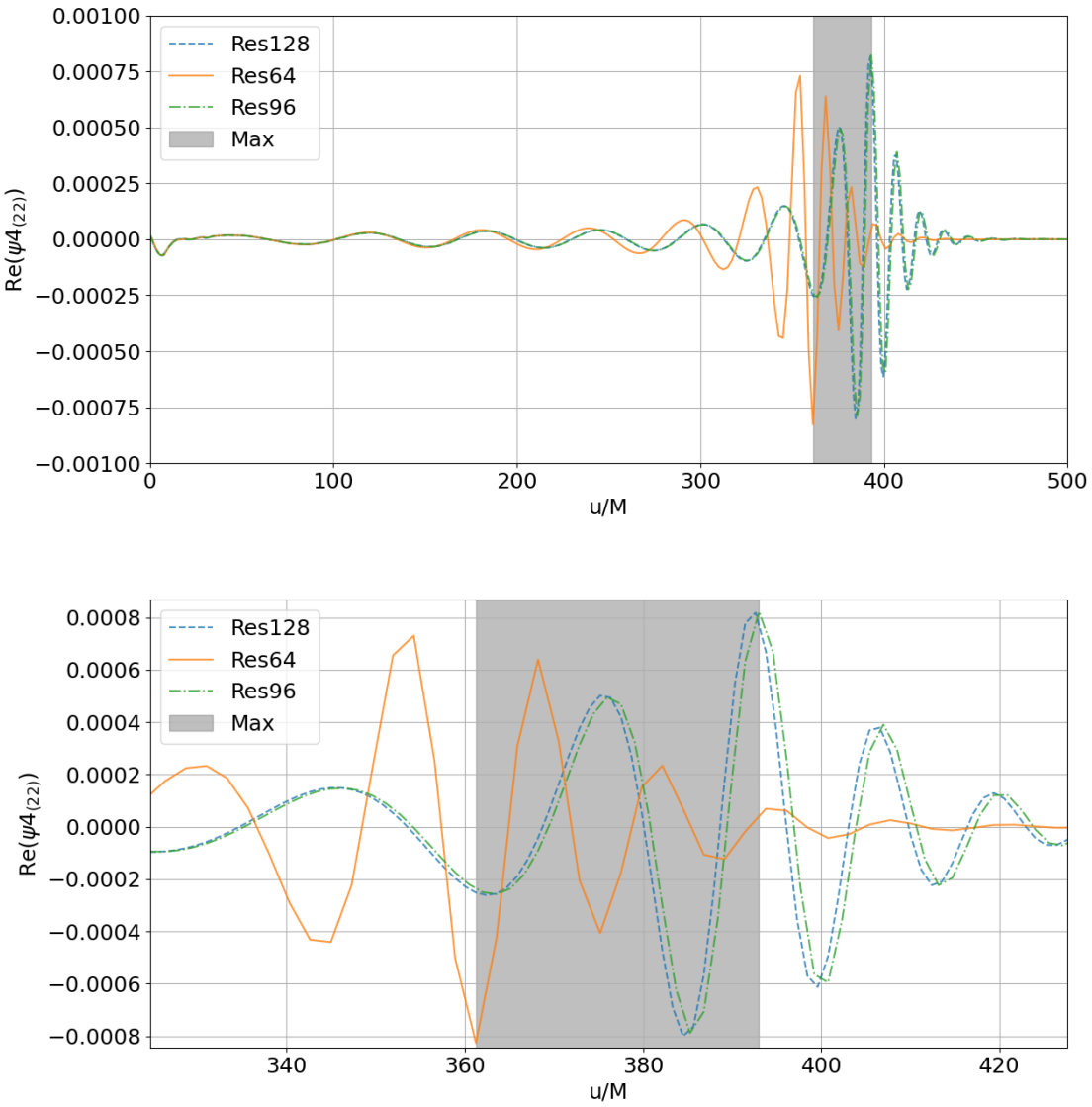

Figure 24: Waveform at resolution 64, 96, 128 and 6 refinement levels. The gray area includes the time difference at merging for the highest and the lowest resolution. Zooming in, it is possible to appreciate the big difference between resolution 64 and the other two.

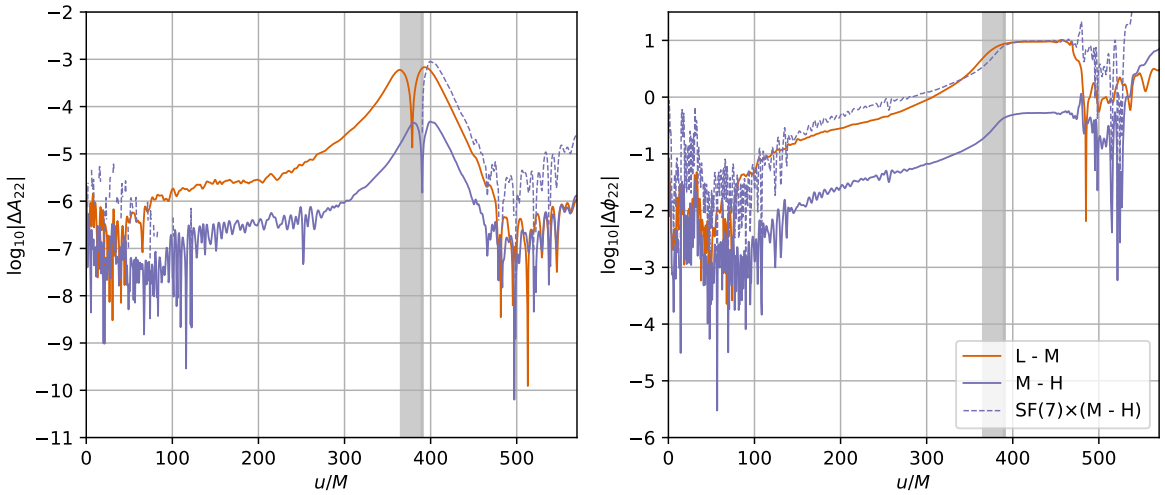

Figure 25: Self convergence test using resolutions 64, 96, 128 and 8 refinement levels. The gray area shows the time difference at merging for the highest and the lowest resolution. The dashed line represents the H-M difference, rescaled by a scaling factor SF(7). With these data it was therefore impossible to retrieve a second-order convergence.

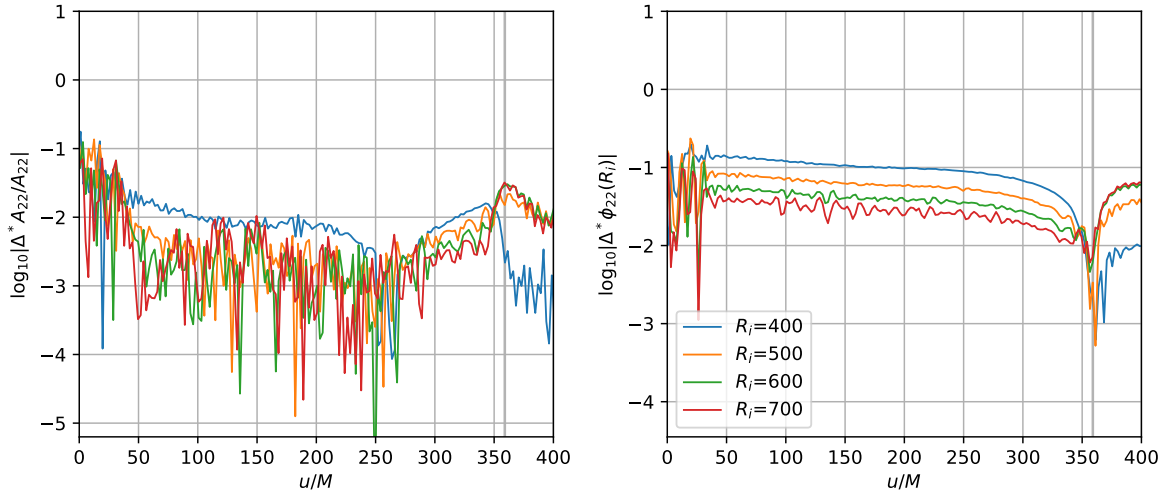

Figure 26: Amplitude (left) and phase (right) differences between $R\psi_{22}$ extracted at consecutive finite-radii $r_i = 400, 500, 600, 700\ M_\odot$ for a simulation with resolution 64 and 6 refinement levels.

4.3.2 Costs and quality of the data

In this section, a quantitative comparison of the different simulations will be provided. The first two simulations of Table 3 were performed on the HPC-cluster ARA using 6 CPUs per task, 4 tasks per node, and a total of 4 nodes per job. The remaining simulations were performed on the HPC-cluster DRACO[38] using the same configuration of CPUs, but working on 2 nodes only being their memory allocation sufficient to efficiently run the simulations for this project.

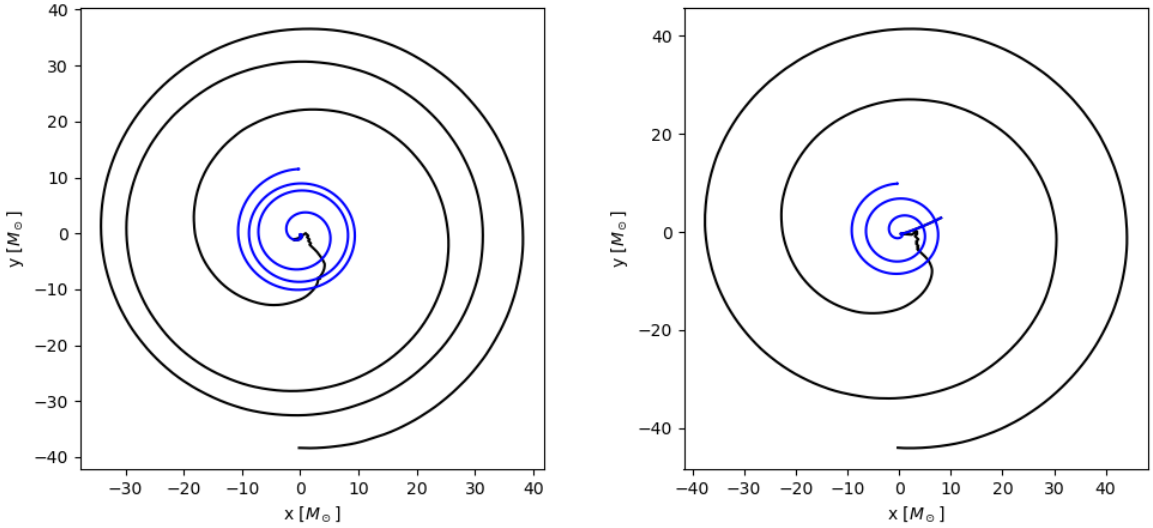

Figure 27: Visualization of the orbits for simulation with mass ratio $Q = 3$ (left panel) and $Q = 4$ (right panel).

The binary configurations evolved consisted of mass ratios $Q = 2, 3, 4$ and initial distance $s = 40, 50, 54$ (geometric units) respectively, to obtain simulations with enough orbits to generate a complete waveform with information from the late inspiral, merging, and ringdown phase. More specifically, three circular orbits were obtained for mass ratio $Q = 2, 3$ while for mass ratio $Q = 4$ only two orbits were considered as to reduce the computational costs, Fig. 27. However, looking at the values reported in Table 3 one could notice that, even considering a shorter simulation, the data obtained with the highest mass ratio are consistently the most challenging and difficult to compute. In terms of computational costs, one of the main tradeoffs is the one involving the resolution and the number of refinement levels. In particular, the amount of memory that the code

[38]More information on the cluster can be found at `https://confluence.uni-jena.de/display/URZ010SD/HPC-Cluster+Draco`, access date: 13 October 2023.

has to allocate per timestep scales like:

$$n_{tot} = \sum_{l=0}^{l_{max}} n_{var} \cdot n_l^3 \tag{212}$$

where $n_{var} = 229$ is the number of variables computed on the grid and n_l stands for the number of points on level l per dimension (so equal to n_{mv} or n if we consider moving or static levels). It is therefore fundamental to choose how many refinement levels to consider in order to have an accurate description of the physics behind the coalescence while saving on computational resources. During this project the analysis of the number of refinement levels to use was performed by changing the maximum number of refinement levels on the BH, where the violation of Hamiltonian and momenta constraint reach their maximum. As one can see from the bottom panel of Fig. 28, data obtained with 6 refinement levels shows too low-quality results to make quantitative assumptions on quantities such as the merging-time, the energy and momentum radiated away via GWs etc. This also means that the physics of the problem itself can change with the adopted resolution.

n_{mv}	n	l_{max}	$h_{lmax}[M_\odot]$	Q	speed[M/hr]	wall-clock time[hr]
64	128.0	6	0.23	2	53.0	90
64	128.0	8	0.06	2	22.0	200
64	76.8	9	0.03	2	30.0	144
96	124.8	6	0.15	2	32.6	141
96	124.8	8	0.04	2	17.0	288
128	166.4	6	0.12	2	18.0	294
64	115.2	6	0.22	3	87.5	42
64	115.2	8	0.05	3	47.4	120
64	83.2	9	0.03	3	30.3	213
96	124.8	6	0.15	3	30.5	147
96	124.8	8	0.04	3	16.7	386
128	166.4	6	0.11	3	19.0	144
128	166.4	8	0.03	3	12.5	410
64	83.2	6	0.22	4	105.0	72
64	83.2	8	0.05	4	35.0	144
96	124.8	6	0.15	4	30.7	119
96	124.8	8	0.04	4	17.0	265
128	166.4	6	0.11	4	18.0	239

Table 3: Performance of BHNS run. The data include `Elliptica` ID interpolation. The notation l_{max} refers to the BH finest refinement level and h_{lmax} to the grid spacing in that level.

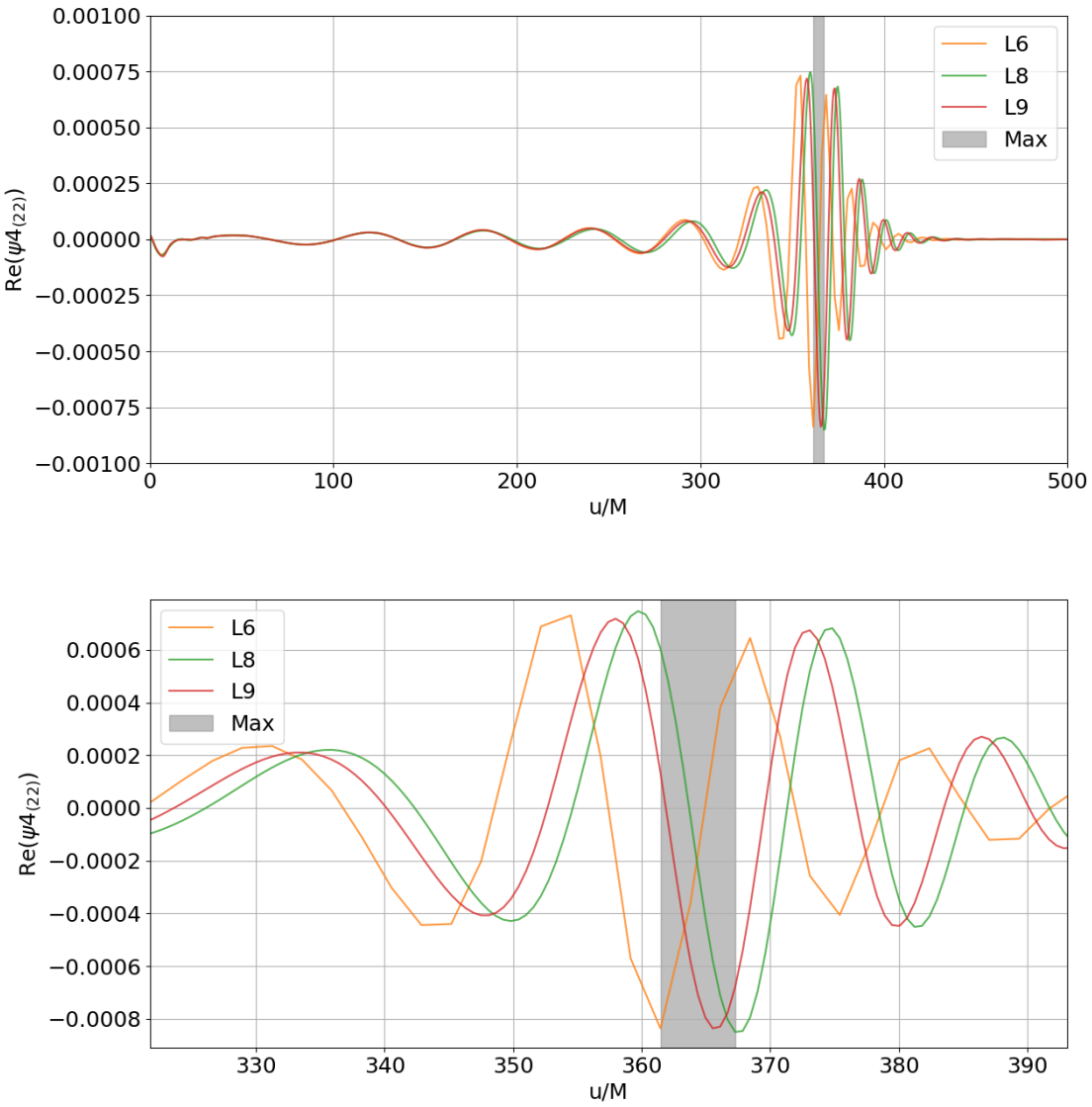

Figure 28: Waveform for a simulation with mass ratio 3, resolution 64, and refinement levels on the BH 6,8,9 respectively. In the bottom panel, a zoom of the waveform shows how the data with 6 refinement levels are insufficient to obtain quality simulations.

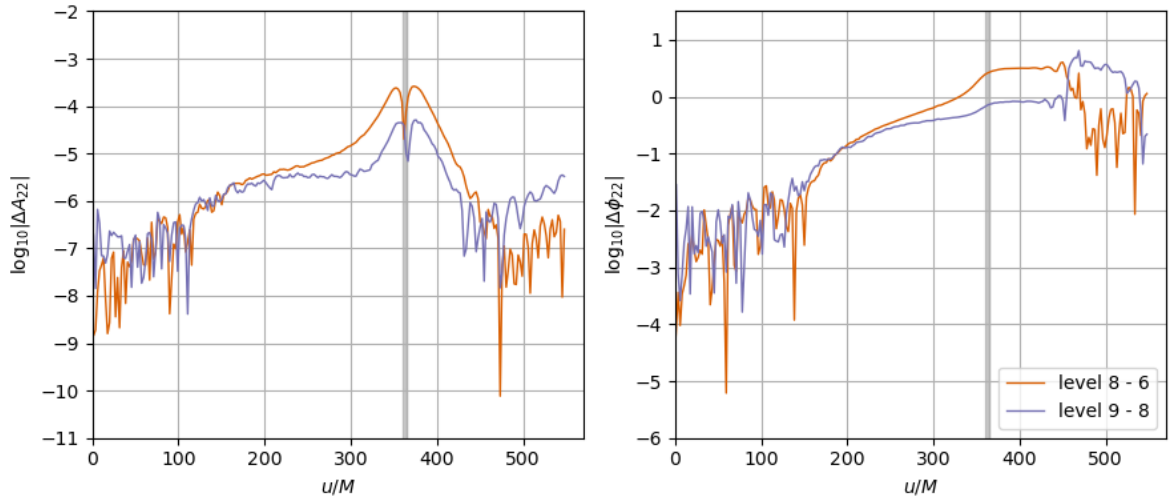

Figure 29: Amplitude (left) and phase (right) for a simulation with resolution 64 and 6, 8, 9 refinement levels on the BH respectively. The behavior shown by the phase differences is again the one seen before for resolution effects.

This aspect can be further appreciated when looking at the dynamical ejecta's mass computed using Eq. (206) (Fig. 30) on a sphere of radius $r_s = 200M_\odot \approx 295$ km where the effects of the resolution can impact the number of elements leaving the system. In this respect, exact quantitative statements can not be made and the discussion should be just considered as qualitative (Chaurasia et al., 2018)[39]. Moreover, the choice of r_s could result in an underestimation of the total ejecta mass by up to $\approx 20\%$ (Radice et al., 2016)

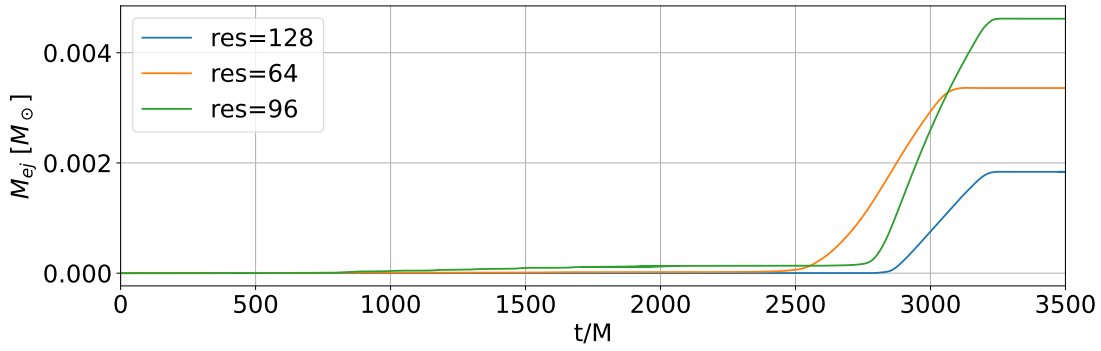

Figure 30: Cumulative ejected mass for a simulation with mass ratio $Q = 2$, resolutions 64, 96, 128 and 6 refinement levels.

[39]See also Dietrich and Ujevic (2017) for more details.

becoming more material unbound at larger radii. However, increasing the extension of the coordinate radius, one could obtain data potentially affected by unphysical artifacts related to the ejecta's density approaching the floor value assigned to the numerical atmosphere.

5 Results

We report in this chapter the results of this project. It will start with the construction and analysis of quasi-equilibrium sequences based on the simulated ID, and will continue with a section dedicated to the physics behind the evolutionary simulations, focused on the characteristics of the merger remnants, the complete waveforms, and the dynamical ejecta. As a reminder, the data simulated are based on nonrotational NSs with fixed ALF2 EOS and baryonic rest mass $M_b = 1.6$. The BH is taken with $M_{irr} = 3.2, 4.8, 6.4$ and non-dimensional spin aligned to the orbital plane with values of $\chi_z = 0, \pm 0.3$. We work therefore in the frame of comparable-mass binaries, expecting the NS to be tidally disrupted outside of the BH's ISCO. The dynamics and the emission of GWs of the nonspinning data are systematically compared.

5.1 Quasi-equilibrium sequences

The emission of gravitational radiation in GR prohibits exactly stationary equilibria of binaries. Still, it is possible to construct quasi-equilibrium states, assuming the emission of GWs during the inspiral as a quasi-adiabatic process. This assumption breaks only when the system approaches coalescence, when the radiation reaction time scale and the orbital period become comparable. For inspiral binaries, it is thus possible to obtain approximately stationary solutions to EFE, obtained by solving the constraints and hydrostationary equations. Series of quasi-equilibrium states are called quasi-equilibrium sequences: they can bring invaluable information about the tidal interaction in GR and can be used to check the quality of the simulated ID for a subsequent dynamical evolution. As seen in section 1.3, their possible ending are two: either a mass-shedding point is found, marking the end of the existence of quasi-equilibrium configurations, or an orbital instability is met. For these purposes, they are typically parameterized by the angular velocity $\boldsymbol{\Omega}$ or by the orbital angular momentum $\boldsymbol{J} = \boldsymbol{J_{ADM}} - \boldsymbol{S_{BH}} - \boldsymbol{S_{NS}}$, with $\boldsymbol{J_{ADM}}$ defined in Eq. (129), as to provide additional information related to the spatial separation of the two objects: while the first one will increase as the two bodies approach during the inspiral, the second is expected to decrease due to the emission of GWs. Therefore Figs. 32 and 33 can be considered as a time evolution of equilibrium states, reading the plots from left to right and from right to left, respectively. Quasi-equilibrium states are described by a specific value of the gauge-invariant binding energy, here defined as:

$$E_b = M_{ADM} - M \tag{213}$$

where M_{ADM} follows from Eq. (123), and M stands for the cumulative gravitational mass of the isolated compact bodies as if they were located at an infinite distance from each other (explicitly $M = M_{gr} + M_{Chr}$). E_b is therefore a quantity always negative, which would ideally remain constant during the inspiral in a Newtonian description, but that

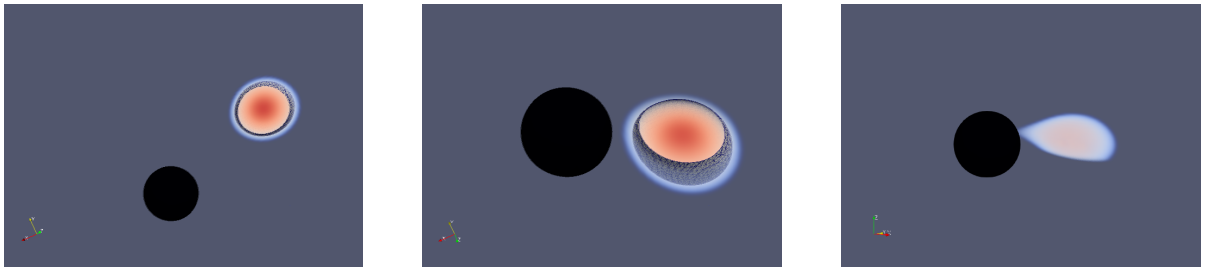

Figure 31: 3D volume rendering of the contour of the NS rest mass density for a simulation with $Q = 3$, res=128, l_{max}=8, snapshot taken on level 4. The AH of the BH is also reported. The camera rotates around the merging to fully describe the distortion of the NS after the mass-shedding limit is reached (first panel). The NS is sectioned to show the internal density gradient.

actually changes thanks to the emission of GWs in a GR framework. Data are normalized by the value[40] of M so to have $E_b/M[= E_b/(Mc^2)]$, $J/M^2[= cJ/GM^2]$, $\Omega M[= G\Omega M/c^3]$. As mentioned in section 3.5, we can study the dynamics of the inspiral by looking for those values for which the motion becomes unstable, searching for the presence of a plateau or a cusp in the E_b/M-ΩM or E_b/M-J/M^2 plane respectively for those curves computed with PN approximation. Interestingly enough, no cusp can be found in the E_b/M vs J/M^2 curves of the EOB model, being the dynamics of the system described correctly until the coalescence, while for the PN, which consists of approximations for point particles, the mass shedding point can not be identified and therefore the cusp is always present. From Fig. 32 we can see that no orbital instability is found along the simulated sequences, matching our expectation. However, in the case of mass ratio $Q = 3, 4$ the location of the ISCO (that one can identify from the cusp visible on the 3PN curves of Fig. 33), is too close to the mass-shedding limit to fully appreciate the post-merger phase. This result was expected from Eq. (4) where we can see how the ISCO is pushed outward as we consider more massive BHs. Moreover, Eq. (5) suggests that the ratio between the compact body separation at the mass-shedding point and the radius of the ISCO, decreases for larger values of Q: this means that for mass ratios sufficiently large, the presence of tidal effects will become irrelevant and the dynamics will reduce to the one of the two-point-particle problem in GR.

The analysis of the ID was performed over different steps, starting from the simplest scenario of nonspinning ID, we compare the equilibrium states computed with `Elliptica` to the binding energy from a third-order PN approximation (Eq. 3 from Blanchet (2002)), visible in the plots as a dashed black line. The results agree quantitatively with this theoretical model for point particles, with differences in the order of 10^{-4}, which are

[40]For NR data points we used the last calculated value of $M_{Chr}$for the BH, while for the NS mass we use the value obtained from the numerically solved TOV equation.

expected towards higher frequencies where tidal effects start to dominate. We introduced then the curves obtained from the EOB model `TEOBResumS`, which, as mentioned in section 2.6 includes tidal and spin-orbit effects. While for large separations none of these effects affect the dynamics, they become more relevant as the bodies get closer: therefore the associated curves, which initially converge, are expected to diverge toward the final part of the inspiral. Specifically, the spin-orbit contribution is by definition negative, consequently, when we introduce a positive spin this effect will be added to the nonspinning model, resulting in a curve with even more negative values. Conversely, when negative spins are considered, the spin-orbit contribution is going to be positive, leading to a less negative curve. This hierarchy can be appreciated by looking at the green and purple solid lines of Fig. 32 which lay respectively below and above the nonspinning red curve.

5.2 Analytical fits of the numerical data

A better description of the role played by spin and tidal interaction during the inspiral phase can be achieved by considering a binding energy that encompasses four distinct contributions at leading order, following Bernuzzi et al. (2014)

$$E_b \approx e_0 + e_{SO} + e_{SS} + e_T \tag{214}$$

which are respectively a nonspinning point mass term e_0, a spin-orbit (SO) term e_{SO}, a spin-spin (SS) term e_{SS} that we will not consider since only irrotational NSs were simulated, and a tidal term e_T. All of them have different PN contributions, starting from e_{SO} at 1.5 PN, followed by e_{SS} at 2 PN, and concluding with e_T at 5 PN. The spin-orbit term has values that scale with $\boldsymbol{\ell} \cdot \boldsymbol{S}$ (with $\boldsymbol{\ell}$ being the unit vector normal to the instantaneous orbital plane) and as said will play a pivotal role in altering the dynamics according to the spin's orientation. In particular, if $e_{SO} > 0$, the contribution to the binding energy will be repulsive, while if it is positive the contribution will be attractive. However, as mentioned in the previous section, the aligned spin configuration produces more negative binding energy at the merger than the anti-aligned one. We pose e_0, as the binding energy of a BBH system, which can be entirely described without considering finite size effects stemming from the presence of matter. To explore these effects, our approach involves devising a method for extracting them from the value of E_b. We start by creating a full BHNS quasi-equilibrium sequence as detailed as possible: this is done by creating twelve ID points for each value of the spin, and subsequently fitting them with a PN curve. To achieve this, we considered the expression for E_b^{3PN} seen in the previous section, with the additional contribution of spin-orbit, Eq. (415) from Blanchet (2014), and tidal effects, Eq. (6.5b) from Henry et al. (2020), and performed a Padé approximant with the addition of free parameters to fit the NR data. This technique consists in approximating a given analytical function near a specific point, by a rational

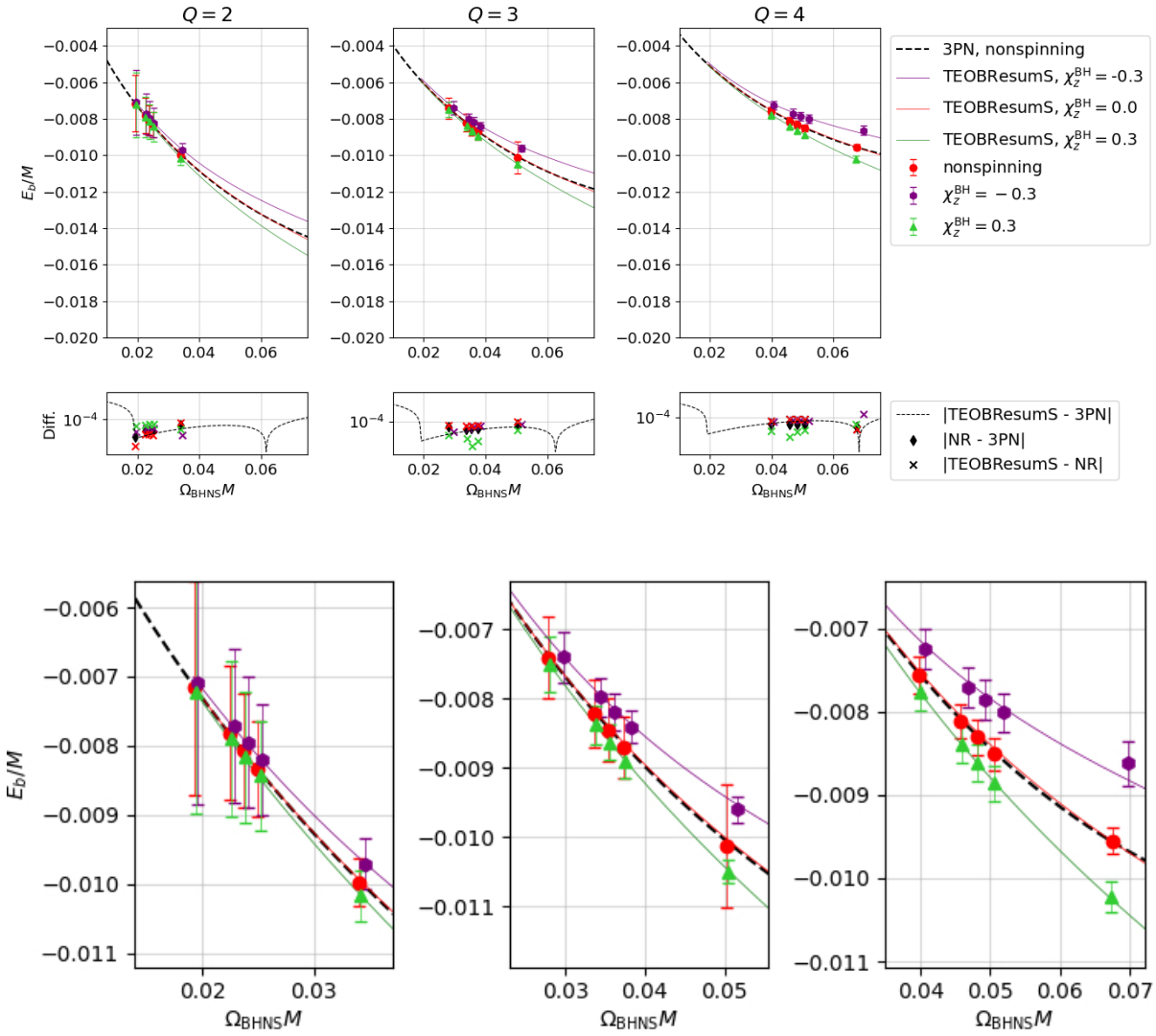

Figure 32: Binding energy as function of the angular velocity for binaries with mass ratio $Q = 2, 3, 4$, $M_b^{NS} = 1.6$ and dimensionless spin $\chi_z^{BH} = 0, \pm 0.3$. The black dashed curve denotes the result obtained in the 3PN approximation for point-particles in the nonspinning configuration. The colored solid lines are obtained using the EOB model `TEOBResumS` for various spin values. The points, marked with the same color code, represent the ID computed from `Elliptica`. The second panel shows the differences computed between the 3PN and the nonspinning EOB model (blacked dashed line), those computed between the NR data and the 3PN approximation (black diamonds), and those between NR data and the EOB model (colored crosses). The third and final graph is a magnified view of the initial plot, providing a closer examination of the data.

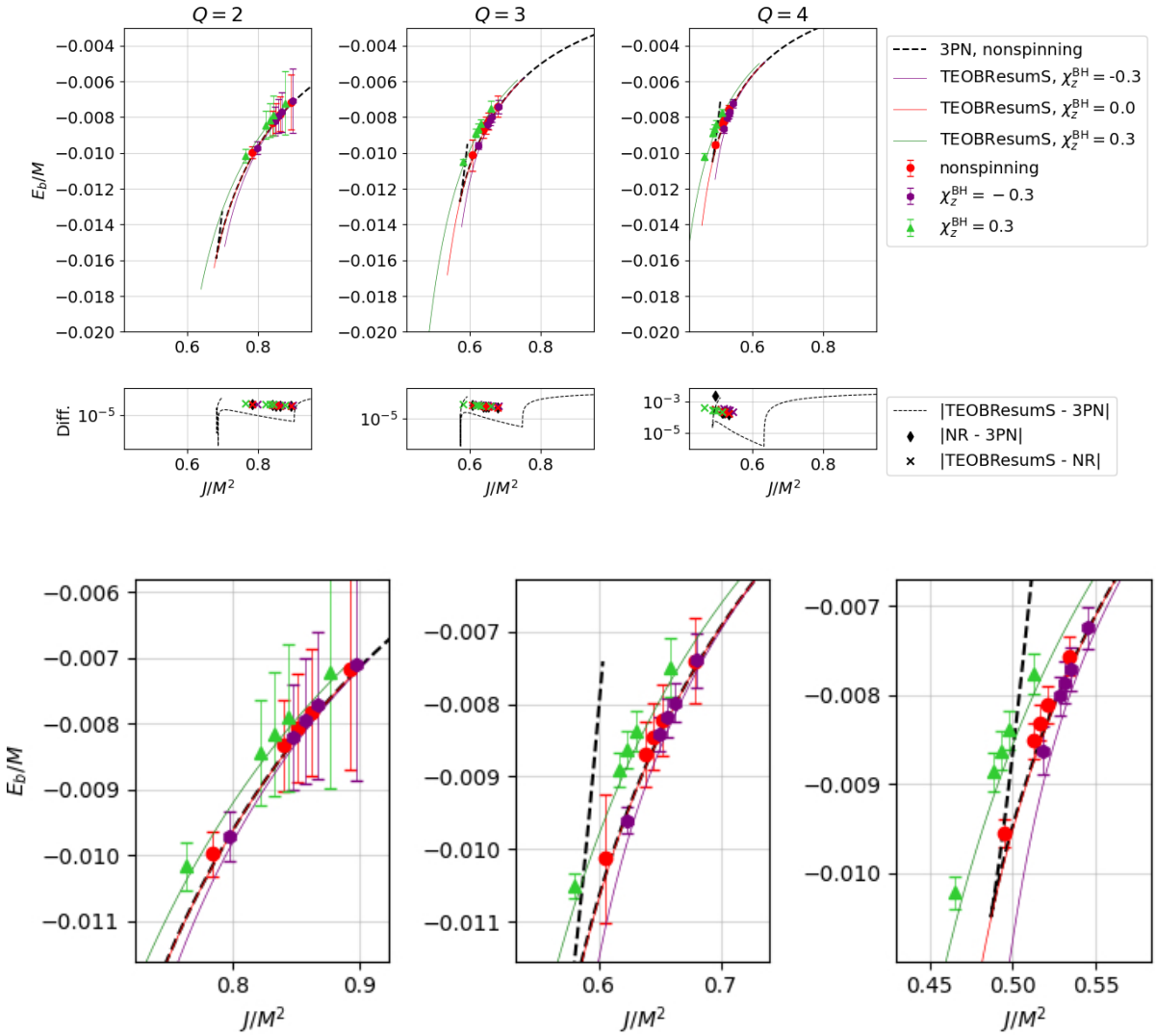

Figure 33: Binding energy as function of the orbital angular momentum, values are obtained using the same configuration of Fig. 32 and share the same color code. Points are computed at the same distances for the different mass-ratios, with values that decrease from right to left. Noteworthy is how the 3PN ISCO (denoted by the presence of a cusp in the black dashed line) is shifted toward larger distances for increasing BH's masses.

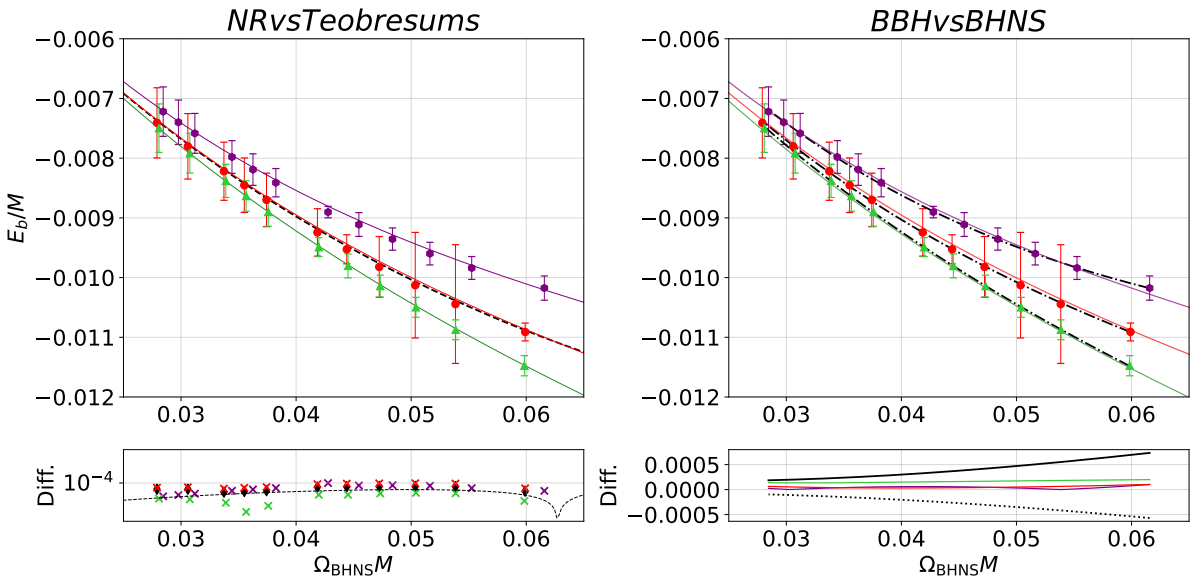

Figure 34: Left panel: Detailed quasi-equilibrium sequence for a simulation with mass ratio $Q = 3$. Points are obtained at coordinate distance d = (35, 38, 40, 42, 44, 46, 50, 52, 54, 58, 60, 62), values reported in geometric units. The error bars follow the behavior described in section 4.1.3, with the only exception of the nonspinning d = 35 ID (last red point on the right), whose resolution was increased to get a better description of the last stable configuration. All the points are in good agreement with the EOB model, with differences in the order of $10^{-4} - 10^{-5}$. Right panel - Top figure: Colored solid lines are plotted using a template for BBH with the same masses and spins of the BHNS configuration. Black dashed lines are obtained by fitting a Padè approximant of the PN binding energy obtained by summing the point-particle model together with a description of the spin-orbit and tidal effects. The bottom panel shows the spin-orbit contribution obtained by subtracting the nonspinning from the spinning Padé approximant. The value of e_{so} is defined as a negative term, therefore we obtain the black dashed line (increasing toward negative values) by considering the positive spin configuration and vice-versa for the black solid line. The green, purple, and red solid lines are a description of the tidal effects, obtained by subtracting the approximant from the BBH models.

function of a given order at the numerator and at the denominator (see appendix D for further information). In particular, a Padé [2,2] was used to approximate the point-particle contribution, and a Padé [3,2] and [6,3] were used respectively for the spin-orbit and tidal contributions based on their PN order. These approximated functions were then added together with the addition of some fitting parameters. We then calculated three sequences for BBH using `TEOBResumS` (one for each value of the spin considered) whose

binding energy will be characterized by the point mass term together with the spin-orbit contribution, where present. In this way it is possible to separate the tidal effects by subtracting the nonspinning BBH curve to the Padé approximant of the nonspinning BHNS; and the spin-orbit effects by subtracting the spinning BHNS curves from the nonspinning one.

$$e_T = E^0_{BHNS} - E^0_{BBH}; \qquad e_{SO} = E^{\pm 0.3}_{BHNS} - E^0_{BHNS} \tag{215}$$

In the right bottom panel of Fig. 34 we can see how the different contributions vary during the inspiral. In particular, the dominant effect is given by the spin-orbit effects which reach an absolute value $\approx 10^{-3}$ while the tidal ones remain in the order of 10^{-4}. As discussed, the sign of e_{so} will be negative for positive spins, and therefore the simulation with $\chi = 0.3$, which starts almost with the same binding energy of the $\chi = 0$ curve, will diverge towards negative values as the merger approaches (black-dashed line). Conversely, the opposite trend is observed for $\chi = -0.3$ (solid black line). As far as the tidal effects are concerned, we can appreciate how they grow progressively during the inspiral, however, their contribution is significantly smaller, reaching a maximal value almost one order of magnitude smaller than the SO effect. This was expected from PN theory, where these effects come into play only at fifth order ($\propto r^{-5}$).

5.3 Waveform

The gravitational waveforms that will be illustrated in this chapter are formed during three different phases. The first one, the inspiral, generates a signal where both amplitude and frequency increase progressively known as chirp signal; the second is the merger phase, characterized by strong GR effects including spin-orbit, tidal and spin-spin coupling; the third and last, is the postmerger phase, which is dominated by the ringdown signal coming from the resonating BH remnant. The latter is strongly correlated to the system's final stage: when the NS is not tidally disrupted, the final perturbation on the BH will be stronger and thus is the associated ringdown signal. This scenario is reproducing essentially the very same waveform produced by BBH mergers. On the other hand, if the NS is completely disrupted the perturbation will be negligible, and the ringdown will be almost completely suppressed. An example of this can be seen in Fig. 35, showing the waveform of our simulations with mass ratio $Q = 4$ (left panel) and $Q = 2$ (right panel). The tidal disruption scenario occurring for the $Q = 2$ simulation, leads to an almost complete suppression of the ringdown; on the other hand, the $Q = 4$ simulation shows a behavior extremely similar to the one of BBHs with a maximum amplitude that, just like in that case, is much larger. This phenomenon is due to the location of a tidal disruption limit too close to the ISCO, which produces an infall of the disrupted material that proceeds from a well-defined and narrow region, without spreading around the BH. Values for this comparison are reported in Table 5, where

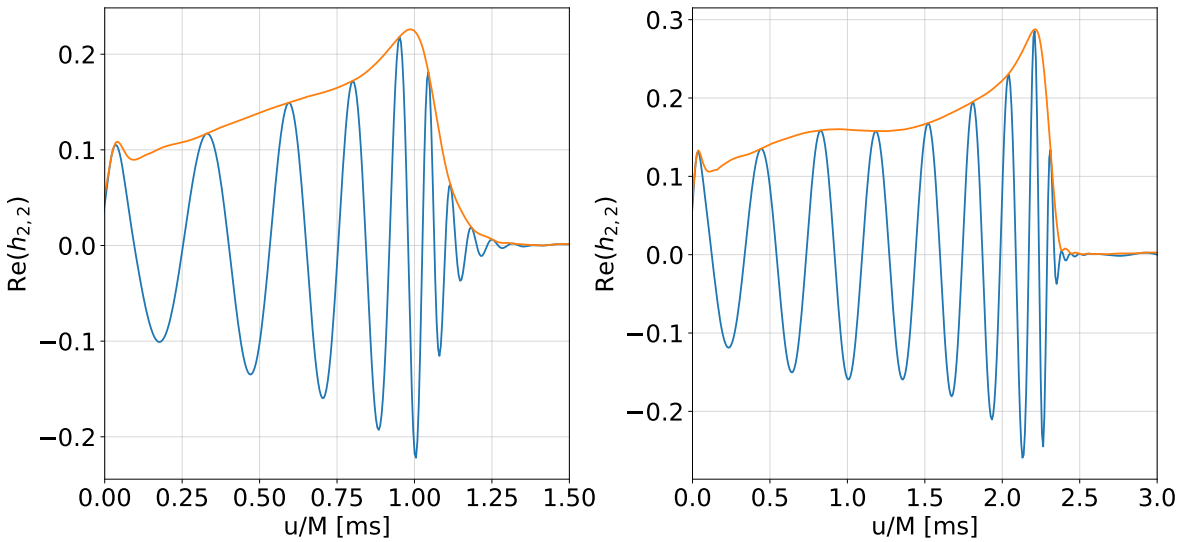

Figure 35: Waveform and amplitude obtained for the (2,2) mode obtained for $Q = 4$ (left panel) and $Q = 2$ (right panel) respectively. It is worth highlighting the presence of a clearly defined ringdown in the scenario with the largest mass ratio. In contrast, this part of the signal is significantly attenuated in the other case.

the simulations with the highest resolutions show a peak luminosity that is more than doubled moving from $Q = 2$ to $Q = 4$. However, the existence of a ringdown signal does not mean that those particular waveforms are going to be entirely identical to the one produced by BBH. To analyze more into detail this discrepancy, we take into account the full description of the multipolar spectrum. We analyze the amplitude associated with each mode and compare the result to the one predicted for BBH, following Nagar et al. (2022). Fig. 36 shows the multipolar structure of the waveform's amplitude at merger, where its highest value occurs. In the case of BBH this structure is hierarchical under a suitable normalization, with a universal shape described by the symmetric mass ratio $\nu = Q/(1+Q)^2$

$$A^{max}_{\ell m}/\nu \approx e^{c_1(\ell)m + c_2(\ell)\ell} \tag{216}$$

showing that the behavior of the maximum amplitude $A^{max}_{\ell m}$ is approximately exponential in m, as ℓ varies. The fitting coefficients $c_i(\ell)$ are taken from Table VI of Bernuzzi et al. (2011). However, in the case of BHNS, this hierarchy is not followed, exception made for the $\ell = 2$ modes. Modes with $m = 0$ show an amplitude at merger that is one order of magnitude larger than the associated m = 1, breaking the hierarchy. The reason for this unexpected trend is still not well known and will be a matter of investigation for further studies on the topic. Like in the case of other compact binaries, the dominant

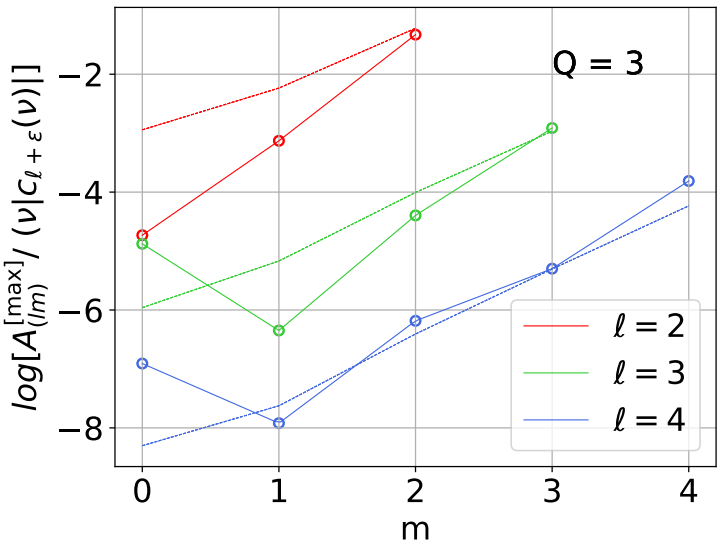

Figure 36: Multipolar hierarchy of merger amplitudes. The colored circles are obtained from our NR simulation, the dashed lines are the test-mass values obtained in the limit of extreme mass-ratio ($\nu \ll 1$). Just like in the case of BBH proposed in Nagar et al. (2022), the plot underlines the attended decrease of importance of the subdominant multipoles with $m < \ell$. A qualitative consistency is found between the test-mass and the comparable-mass cases, with the only caveat of the $m = 0$ modes.

modes are those with the same value of ℓ and m, with a modal amplitude that decreases for increasing values of ℓ and an energy emission dominated by the (2,2) mode. Fig. 37 provides a visualization of this phenomenon[41], showing the gravitational wave multipolar spectrum of a simulation with $Q = 4$, $n_{mv} = 128$, $l_{max} = 6$. In the bottom right panel, a cumulative plot of the modes is provided, with colors associated with the value of ℓ. The associated value of the amplitude can be found in Table 4, showing how the (2,2) mode dominates the expansions, with an amplitude almost four times larger than the second largest mode (3,2).

Lastly, one can analyze the GW luminosity of the simulations. The coalescence of compact binaries is one of the most luminous events in terms of emitted GWs, with typical values in the order of magnitude of $L^{peak} \approx 10^{55} - 10^{56}$ erg/s with the largest ones obtained for equal-masses BHs and spin aligned configurations which as discussed follow an enhancement of the GWs emission due to the spin-orbit effects. In the case of BNS and BHNS, tidal effects have also to be considered. In particular, larger emissions are connected to smaller values of the gravitoelectric quadrupolar tidal polarizability

[41]The burst of emission that one can see at early times, is a spurious numerical effect that affects puncture-type data known as "junk-radiation", see Higginbotham et al. (2019) for a more detailed description of this effect.

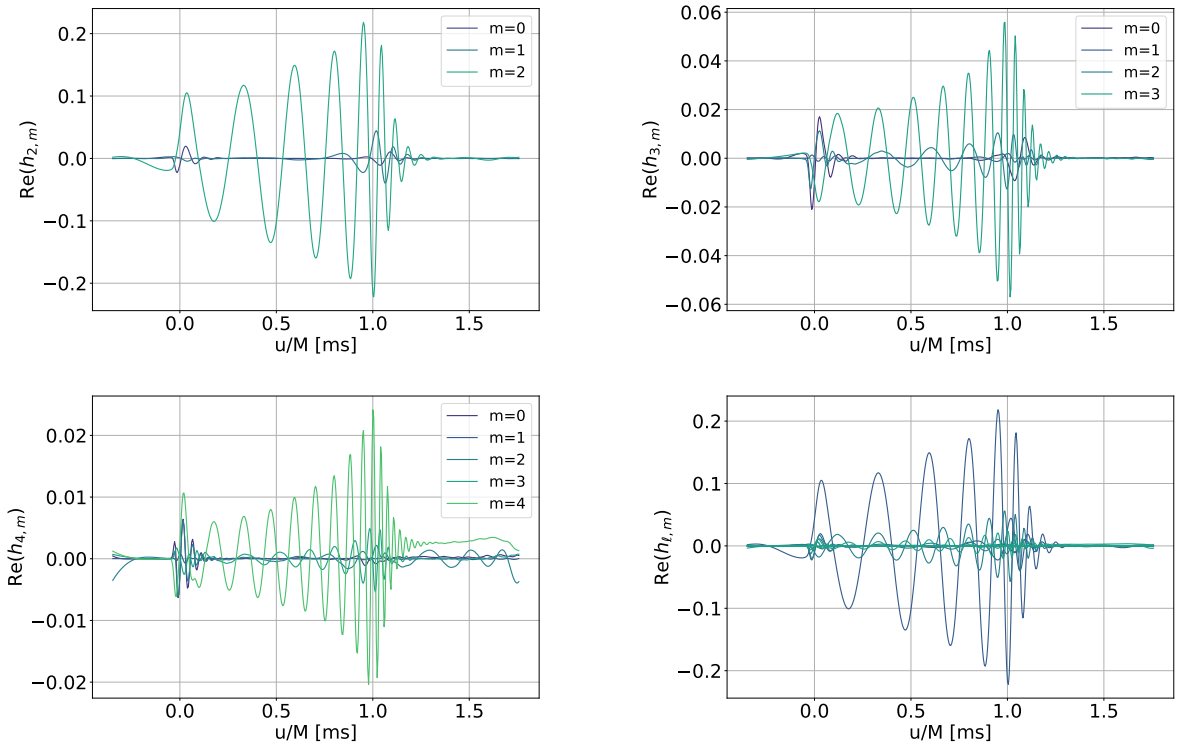

Figure 37: Multipolar waveform for a simulation with $Q = 4$. The top and bottom left panels represent modes with ℓ=2, 3, 4. Noteworthy are the differences on the y-axis. The bottom right panel is a cumulative representation of the modes, with colors associated with each value of ℓ. The (2,2) mode, dark-blue curve in the last plot, is the dominant one.

ℓ	m	$\lvert A_{mrg}\rvert$	$M\omega^{\ell,m}_{mrg}$
2	0	0.007	0.023
2	1	0.305	0.047
2	2	0.308	0.226
3	0	0.012	0.021
3	1	0.053	0.012
3	2	0.081	0.013
3	3	0.525	0.058
4	0	0.019	0.006
4	1	0.104	0.002
4	2	0.106	0.006
4	3	0.094	0.007
4	4	0.598	0.025

Table 4: Multipolar amplitude and frequency at merger for $Q = 4$, on a simulation with $n_{mv} = 128$, $l_{max} = 6$, values are reported in geometric units.

coefficients defined for BNS as

$$\kappa_2^T = \kappa_2^A + \kappa_2^B \tag{217}$$

and which reduces to $\kappa_2^T = \kappa_2^{NS}$ for BHNS. In particular,

$$\kappa_2^A = 2\frac{X_B}{X_A}\left(\frac{X_A}{\mathcal{C}_A}\right)^5 k_2^A \tag{218}$$

where k_2^A is the quadrupolar Love number, see Eq. (67), describing the static quadrupolar NS's deformation, $\mathcal{C}_A$ is the compactness, and $X_A = M_A/M$. Specifically, k_2^T parametrizes at leading-order the tidal interactions in the general relativistic 2-body Hamiltonian, together with the waveform's amplitude and phase. Larger emissions are obtained for smaller values of k_2^A, that one can find for those scenarios mimicking the dynamics of BBHs, i.e. for larger masses and more compact NSs. This behavior can be observed from the values of Table 5, showing how the GWs' emission and the associated peak luminosity scale as a function of the mass-ratio Q.

5.4 Merger remnant

The post-merger phase is characterized by the formation of a new BH, that in the tidal disruption scenario, can be surrounded by an accretion disk. The final value of the BH's mass and spin are typically related to the initial mass and spins of the isolated bodies, but since only irrotational configurations have been studied during the evolution, we will mainly focus on the mass-ratio dependencies. The expectations are again focused on the

Q	n_{mv}	l_{max}	u_{mrg}[ms]	f_{mrg}[kHz]	J^{tot}_{rad}[g · cm^2/s]	E^{tot}_{rad}[erg]	L^{peak}_{GW} [erg/s]
2	64	6	9.70	2.22	$2.57 \cdot 10^{49}$	$8.38 \cdot 10^{52}$	$2.91 \cdot 10^{56}$
2	64	8	9.64	2.28	$2.74 \cdot 10^{49}$	$9.99 \cdot 10^{52}$	$3.97 \cdot 10^{56}$
2	64	9	9.76	2.25	$2.71 \cdot 10^{49}$	$9.75 \cdot 10^{52}$	$3.76 \cdot 10^{56}$
2	96	6	10.52	2.24	$2.83 \cdot 10^{49}$	$9.62 \cdot 10^{52}$	$3.46 \cdot 10^{56}$
2	96	8	10.50	2.26	$2.90 \cdot 10^{49}$	$1.03 \cdot 10^{53}$	$3.99 \cdot 10^{56}$
2	128	6	10.50	2.26	$2.86 \cdot 10^{49}$	$9.96 \cdot 10^{52}$	$3.69 \cdot 10^{56}$
3	64	6	11.10	2.12	$4.18 \cdot 10^{49}$	$1.31 \cdot 10^{53}$	$5.90 \cdot 10^{56}$
3	64	8	11.30	2.08	$4.43 \cdot 10^{49}$	$1.56 \cdot 10^{53}$	$7.82 \cdot 10^{56}$
3	64	9	11.24	2.05	$4.42 \cdot 10^{49}$	$1.54 \cdot 10^{53}$	$7.52 \cdot 10^{56}$
3	96	6	12.08	2.10	$4.47 \cdot 10^{49}$	$1.48 \cdot 10^{53}$	$6.98 \cdot 10^{56}$
3	96	8	12.10	2.12	$4.56 \cdot 10^{49}$	$1.60 \cdot 10^{53}$	$7.91 \cdot 10^{56}$
3	128	6	12.07	2.13	$4.54 \cdot 10^{49}$	$1.54 \cdot 10^{53}$	$7.46 \cdot 10^{56}$
3	128	8	12.08	2.12	$4.61 \cdot 10^{49}$	$1.61 \cdot 10^{53}$	$8.00 \cdot 10^{56}$
4	64	6	7.90	1.75	$4.68 \cdot 10^{49}$	$1.40 \cdot 10^{53}$	$6.83 \cdot 10^{56}$
4	64	8	8.25	1.62	$4.92 \cdot 10^{49}$	$1.57 \cdot 10^{53}$	$8.28 \cdot 10^{56}$
4	96	6	8.20	1.70	$4.78 \cdot 10^{49}$	$1.50 \cdot 10^{53}$	$7.87 \cdot 10^{56}$
4	96	8	8.19	1.71	$4.87 \cdot 10^{49}$	$1.59 \cdot 10^{53}$	$8.78 \cdot 10^{56}$
4	128	6	8.18	1.71	$4.83 \cdot 10^{49}$	$1.55 \cdot 10^{53}$	$8.29 \cdot 10^{56}$

Table 5: Overview of the results obtained from the numerical simulation, reported in physical units. Values are taken from the largest common extraction radius $r_{ext} = 400$ to highlight the variation with the mass ratio. Merging times and merging frequencies are computed from the values of the (2,2) modes. As a reminder, let's recall that the number of orbits changes: while for $Q = 2, 3$ three orbits were simulated, only two were considered for $Q = 4$, this explains the smaller value of u_{mrg} in the latter case.

possibility of having a NS completely disrupted outside the ISCO, therefore two main possibilities are available:

1. the stellar material wraps around the BH, forming a disk, see Fig. 42. In this way, the NS's mass is not expected to contribute significantly to the final BH's mass. Moreover, as we saw, the ringdown emission is in this case almost completely suppressed, which means that the system will conserve a larger amount of energy and momentum. This allows the final BH to have a larger spin.

2. the NS plunges directly onto the BH: in this case almost no mass is ejected, and no disk is expected to form. Therefore, the final BH's mass will be significantly larger, as visible in Fig. 43. The ringdown phase this time can not be neglected: it will bring the system to relax toward an equilibrium configuration, hence, the final BH's spin is expected to be smaller, being a larger fraction of the angular

momentum dissipated.

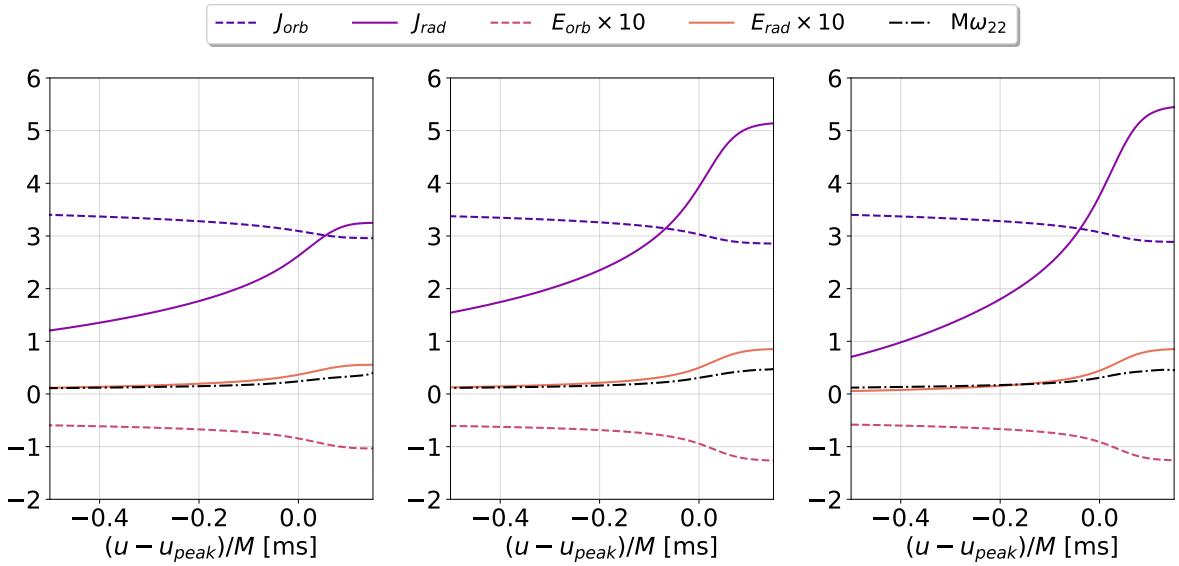

Figure 38: Orbital frequency ω estimated from the (2,2) GWs (black dash-dotted line) together with energy and orbital momentum evolution and loss through GWs. Mass ratios $Q = 2, 3, 4$ are reported in the left, central, and right panels respectively.

This difference in the quantity of momentum conserved by the system can be appreciated by looking at the left and central panels of Fig. 38, showing mass ratio $Q = 2$ and $Q = 3$ respectively. The central panel is characterized by a well-defined ringdown phase, with a significantly larger amount of momentum radiated via GWs (purple solid line). Table 6 shows how the largest remnant masses are found for our largest mass-ratios, while the opposite trend is observed for the dimensionless spin. We report in Fig. 39 the evolution of the AH mass and area for a $Q = 3$ simulation representing a plunge-like

Q	$M^{BH}[M_\odot]$	$M^{disk}[10^{-3}M_\odot]$	$M^{BH}_{rmn}[M_\odot]$	χ^{BH}_{rmn}
2	3.2	0.80	4.22	0.72
3	4.8	-	5.86	0.57
4	6.4	-	7.48	0.47

Table 6: Data reported for $n_{mv} = 128$ and $l_{max} = 6$, NS's gravitational mass $M_{NS} = 1.44$. Only the smallest mass ratio produces the suitable condition for the formation of a disk, due to the NS's disruption. Remnant mass and spin's value are related to the energy and momentum radiated away in the three different cases.

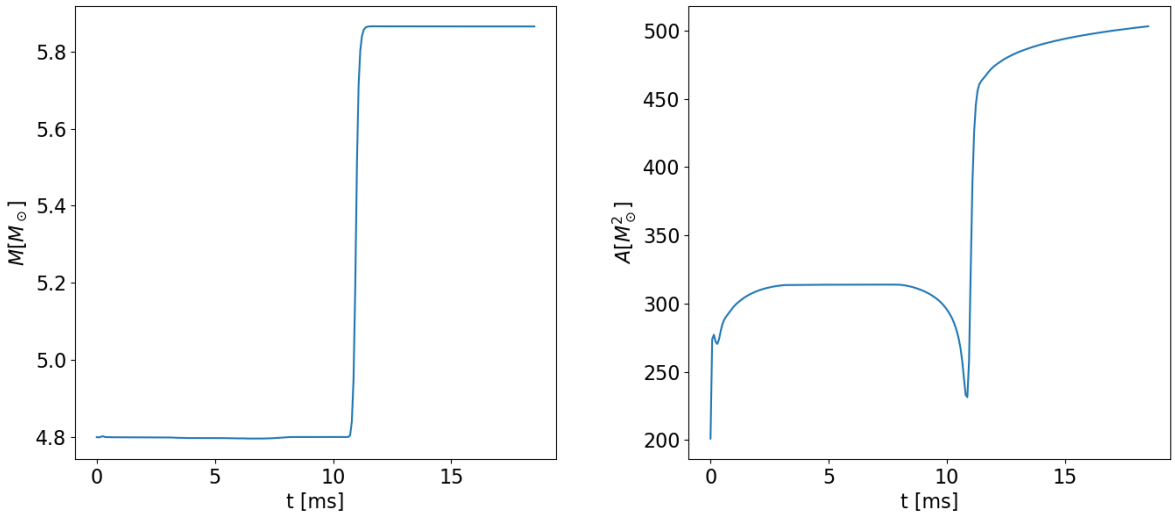

Figure 39: Evolution of the BH's mass and area (left and right panel respectively) for $Q = 3$. Little variation in the AH area can still happen due to the slow accretion of the stellar material onto the BH.

case. Following Zappa et al. (2019), one can approximate the remnant BH's mass scaled to M using a mass conservation formula:

$$\frac{M^{BH}_{rmn}}{M} = 1 - \frac{E^{tot}_{rad}}{M} - \frac{M^{disk}}{M} \tag{219}$$

with E^{tot}_{rad} being the total energy emitted via GWs and M^{disk} the baryonic mass of the disk. This equation shows how the final BH's mass will be the result of two opposite trends: the energy lost through gravitational radiation and the effect of tidal disruption leading to the disk's formation. Focusing on the differences between simulated BHNS and BBH (Zappa et al., 2019) it is again possible to notice how finite-mass-ratio effects lead to a similar trend. However, for BHNS systems, the value of the remnant BH's mass M^{BH}_{rmn}/M slightly increases with respect to the BBH case for a given mass-ratio if the tidal interactions are weak: this effect can be explained through a reduced gravitational energy radiated by the BHNS system. Focusing on the final spin, one can apply a similar reasoning, considering that a smaller amount of angular momentum is dissipated being NSs less compact than a companion BH, therefore also in the case of plunging the dimensionless spin is expected to be larger, and this tendency will increase in the case of strong tidal interactions.

5.5 Ejecta

The formation mechanism of BHNS' dynamical ejecta is to be found in the torque exerted on the tidal tail. This propagation of stellar material is typically characterized by high degree of nonsphericity with a crescent-like shape on the equatorial plane. This asymmetry is mainly due to the tidal torque efficiency, which is uneven, and with the highest values along the orbital plane. However, as the dynamical ejecta escape from the gravitational attraction of the remnant BH, their expansion becomes gradually homologous moving from a crescent-like shape to a half-disk-like shape. In the case of less massive ejecta ($M^{ej} < 0.01 M_{\odot}$), the first part of the evolution is skipped, and the shape is spiral-like from the beginning (Kawaguchi et al., 2015), see Fig. 42. This result is consistent with what we found for the chosen EOS, with results visible in Fig. 40 showing a three-dimensional rendering of a simulation with $Q = 3$ on refinement level $l = 4$. An additional aspect, not investigated during this project, is the possibility of having a modification of the morphology due to the radioactive decay heat of r-process elements[42]. We proceed to calculate the ejecta's mass using Eq. (206) (from now on $M^{\mathcal{S}}_{ej} = M^{ej}$) on a sphere of extraction radius $r = 200 M_{\odot} \approx 295$ km, and its velocity. The latter is reported in two different contributions: v_{ρ} as the velocity estimated on the orbital plane, and v_z as its perpendicular component. In this way, we expect to find values of v_{ρ} significantly larger than v_z being the ejecta mainly distributed on the orbital plane.

Fig. 41, shows how the dynamical mass ejection is concentrated in a single impulsive

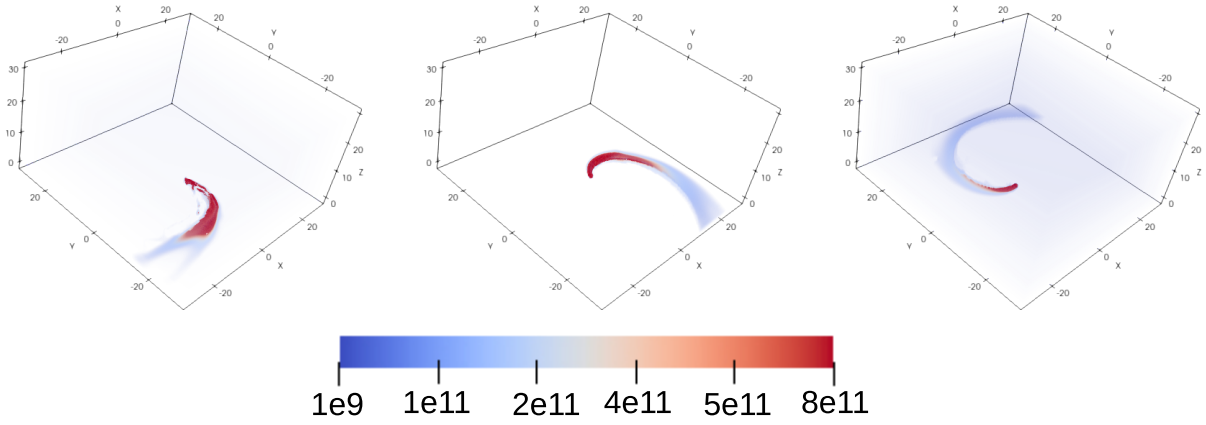

Figure 40: 3d plot showing the time evolution of the unbound material for $t - t_{mrg} = (-1.93, -1.62, -1.26)$ [ms], colors are reported in cgs units (g/cm^3).

[42]Heating coming from the r-process could inflate the ejecta into a more spherical shape, smoothing their small-scale structure (Darbha et al., 2021).

Q	n_{mv}	l_{max}	$M^{ej}[10^{-3}M_{\odot}]$	v_{ρ}^{ej}[c]	v_{z}^{ej}[c]
2	64	6	3.36	0.19	0.016
2	64	8	3.10	0.19	0.013
2	64	9	4.06	0.21	0.015
2	96	6	4.62	0.18	0.014
2	96	8	4.16	0.19	0.014
2	128	6	1.84	0.19	0.009
3	64	6	0.82	0.51	0.045
3	64	8	0.02	-	0.080
3	64	9	0.16	-	0.020
3	96	6	0.13	0.21	0.014
3	96	8	0.10	0.37	0.001
3	128	6	-	0.67	0.009
4	64	6	0.54	0.42	0.054
4	64	8	0.63	0.89	0.005
4	96	6	0.02	0.75	0.030
4	96	8	0.07	0.46	0.008
4	128	6	-	-	0.008

Table 7: Overview of the results obtained from the numerical simulation. The reported values of M^{ej} refer to the total amount of ejected material throughout the whole simulation.

event, lasting a few milliseconds: therefore we can assume a robust estimation of this quantity, being the phenomenon fully covered by the simulation. As expected, only the scenario covered by mass ratio $Q = 2$ provides a sufficient amount of unbound material, being the NS completely tidally disrupted. In this case, we obtain values for masses and velocities consistent with the available literature of BNS mergers, i.e. $M^{ej} \approx 10^{-2} - 10^{-3}\ M_{\odot}$ and $v^{ej} \approx 10^{-1}c$. However, by looking at the results reported in Table 7, finding a trend in the ejecta mass and velocity as function of Q can be complicated since the results can vary a lot with the resolution. In general, we report that the abundance of ejected material increases as the mass ratio decreases, while the velocity increases for increasing mass ratios. Similar results were obtained in Hayashi et al. (2021).

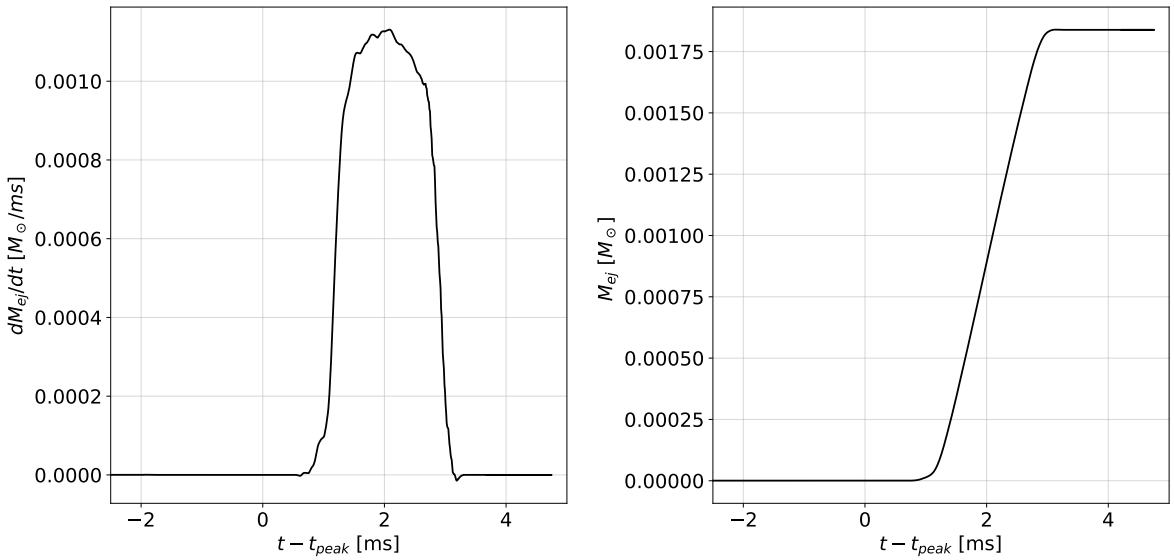

Figure 41: Ejected mass rate (left panel) and cumulative ejected mass (right panel) for a $Q = 2$ simulation, see Eq. (206). The ejection of the material is a single impulsive event. Mass values reported in Table 7 are obtained from the top values of the right panel.

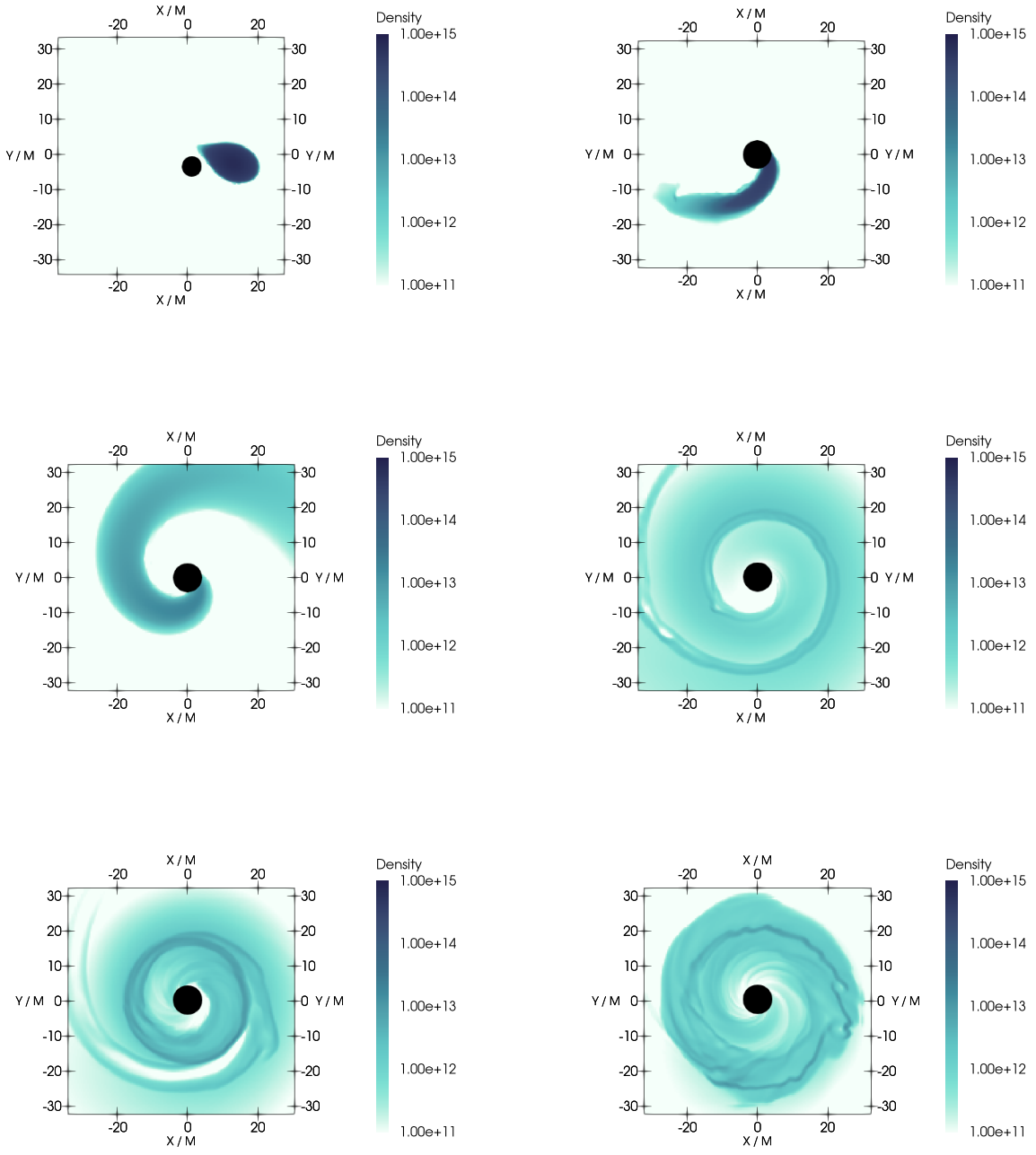

Figure 42: Evolution of the rest mass density for a simulation with $Q = 2$, snapshots from $l_{mv} = 4$, showing a tidal disruption scenario. The scalars bars report the values of the density in cgs units. The apparent horizon area of the BH is also reported.

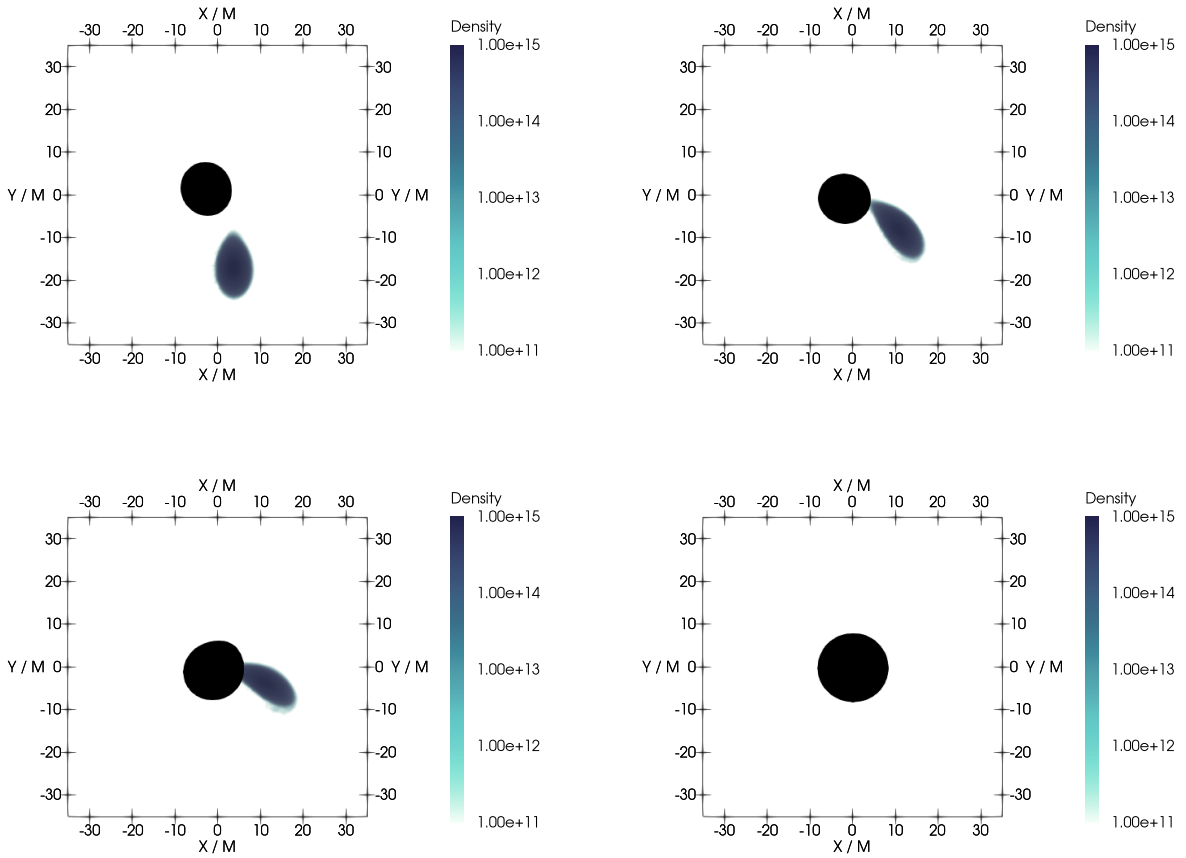

Figure 43: Evolution of the rest mass density for a simulation with $Q = 4$, snapshots from $l_{mv} = 4$. The NS is this time not tidally disrupted, the evolution of the stellar matter leads to a net increase of the AH area, visible in the bottom right panel, due to the increased remnant mass. Values reported in the scalar bar are in cgs units.

6 Summary, conclusions and future prospects

The NR simulations performed during this project were used to shed light on the dynamics behind BHNS binaries, analyzing the details of the emission of gravitational waves and the ejection of stellar material that characterizes this region of the parameter space for the chosen EOS. At the same time, they showed a good agreement with the considered EOB model as far as the inspiral phase was concerned. However, the final aim of the model is to describe efficiently all the different stages of the system's evolution from the inspiral to the post-merger phase. As we discussed in section 2.6, NR simulations can be used to inform EOB models, expanding the available parameter space and producing more accurate GW templates, describing the merger and the ringdown phase. A natural follow-up for this project involves using the data produced to inform `TEOBresumS`, refining its results as far as systems with mass-ratio $Q = 2, 3, 4$ are concerned, with a NS described by the ALF2 EOS, expanding the results presented in Gonzalez et al. (2023a) and Zappa et al. (2019). After this tuning procedure is performed, an analysis of the phase differences and of the faithfulness should be produced to analyze and compare the EOB and the NR waveforms. The former is typically done by defining a function $\Xi = (\delta t, \delta\phi)$ such that

$$\Xi = (\delta t, \delta\phi) = \int_{t_i}^{t_f} [\phi_{NR}(t) - \phi_{EOB}(t + \delta t) + \delta\phi]^2 dt \tag{220}$$

where ϕ_{NR} and ϕ_{EOB} stand for the phases of the NR and EOB waveform respectively, and t_i and t_f define the alignment window where the waveforms are compared. The phasing procedure consists of minimizing this function, finding optimal values for δt and $\delta\phi$. The latter is then used to shift the EOB waveform in order to compare it directly to the NR data. This initial step was partially done with our simulations, where the comparison was made using the untuned model (see Fig. 44). We found however good agreement for mass ratio $Q = 3$, with a difference at merger around $2 \cdot 10^{-3}$, while $Q = 2$ and $Q = 4$ introduced both larger dephasing, in the order of 10^{-2}. The following step consists of calculating the faithfulness $\mathcal{F}$ and its complementary, the unfaithfulness

$$\bar{\mathcal{F}} = 1 - \mathcal{F} = 1 - \max_{t_0,\phi_0} \frac{\langle h^{EOB}, h^{NR} \rangle}{||h^{EOB}||||h^{NR}||} \tag{221}$$

where t_0 and ϕ_0 denote the initial time and phase, and $||h|| = \sqrt{\langle h, h \rangle}$. The inner product is defined as

$$\langle h_1, h_2 \rangle = 4\Re \int \frac{\tilde{h}_1(f)\tilde{h}_2^*(f)}{S_n(f)} df \tag{222}$$

where $S_n(f)$ is the power spectral density of the detector and $\tilde{h}(f)$ is the Fourier transform of $h(t)$. If $\bar{\mathcal{F}}$ is small enough, and the simulations have a sufficiently large number of

orbits, the data can be considered suitable for parameter estimation up to signal with a certain signal-to-noise ratio related to $\mathcal{F}$. More details on this can be found in Gonzalez et al. (2023a) and Gonzalez et al. (2023b).

A subsequent study that could be performed, explores the possibility for the BH to absorb the GWs emitted by the NS during the inspiral phase. This effect, described in Alvi (2001) for BBHs, should be visible in the form of tiny fluctuations in the AH mass during the inspiral phase and should characterize those systems with high values of the spin. An initial attempt to capture this phenomenon was made through a simulation with parameters $Q = 3$ and $\chi = 0.6$. The observed features, visible in Fig. 45, were consistent with the anticipated effect. However, it's crucial to note that the resolution used in this initial attempt is insufficient for making robust and quantitative conclusions. A recommended course of action would be to conduct additional simulations, particularly focusing on high-spinning systems, and employing higher resolutions to more accurately investigate and characterize this absorption effect.

In terms of EM counterparts for BHNS systems, an important additional study involves the production of gamma-ray bursts and kilonovae signals. In fact, as mentioned in section 1.1, BNS and BHNS neutron-rich ejected material settles the right condition for the activation of rapid neutron capture processes, from which could originate elements with atomic mass number $A > 120$ and which have formation mechanisms excluded from the core-collapse supernovae scenario. This theoretical result, proposed for the first time in Lattimer and Schramm (1974), has been recently confirmed in Levan et al. (2023) using spectroscopic data from the James Webb Space Telescope. It is therefore fundamental to study whether or not our simulated binaries could be consistent with the emission of a Kilonova: the quasi-thermal transient powered by radioactive decays of r-process elements. Our results, especially in simulations with $Q = 2$, have shown good agreement with the conditions necessary for generating both of them. The available data, including ejecta masses and velocities, offers an opportunity to make order-of-magnitude estimations for the luminosity and color of the Kilonova, eventually useful to derive a complete lightcurve. In the presence of disks's formation, it could be also possible to study the emission of gamma-ray bursts which are fueled by the mass accretion processes on the BH's. In this respect, it could be however necessary to perform a different kind of simulation, introducing magneto-hydrodynamical effects to better describe the complex nature of the accretion disk, which are not included in `BAM`, to obtain better results.

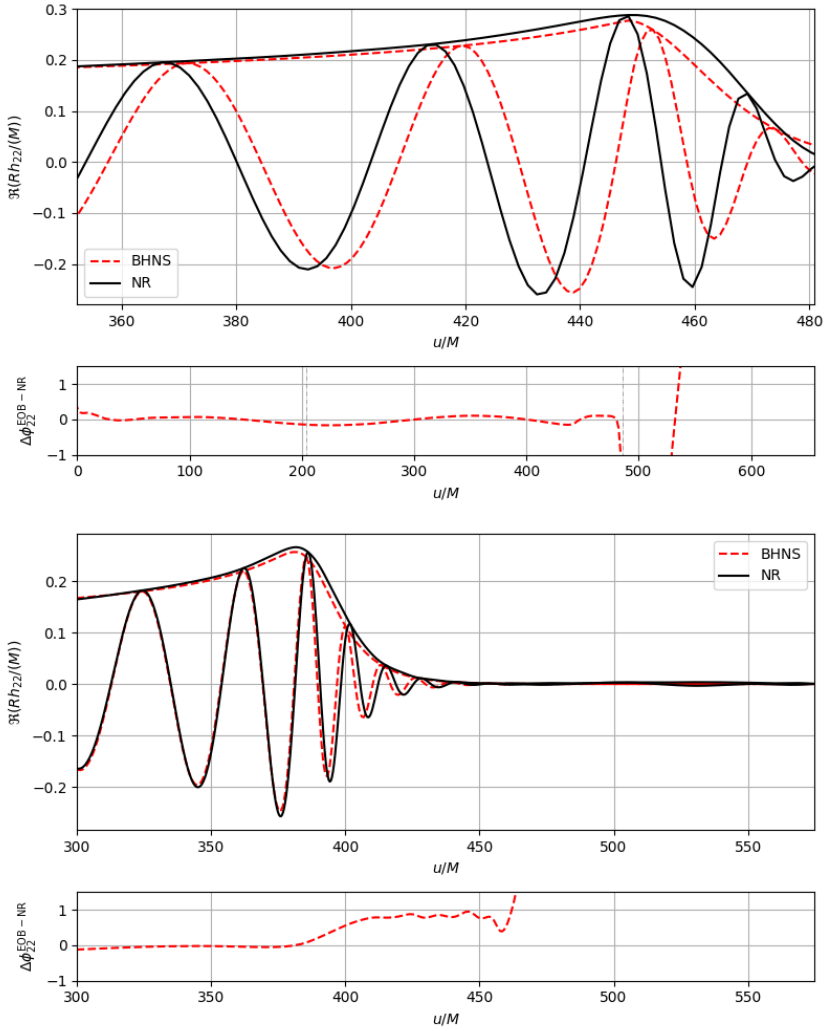

Figure 44: Phasing procedure for a simulation with $Q = 2$ (top panel) and $Q = 3$ (bottom panel), the differences between the EOB model and the NR waveform change significantly for different mass ratios. A dephasing closed to $2 \cdot 10^{-3}$ was found for $Q = 3$ at merger, while for $Q = 2$ we obtained values an order of magnitude larger, around $-3.6 \cdot 10^{-2}$.

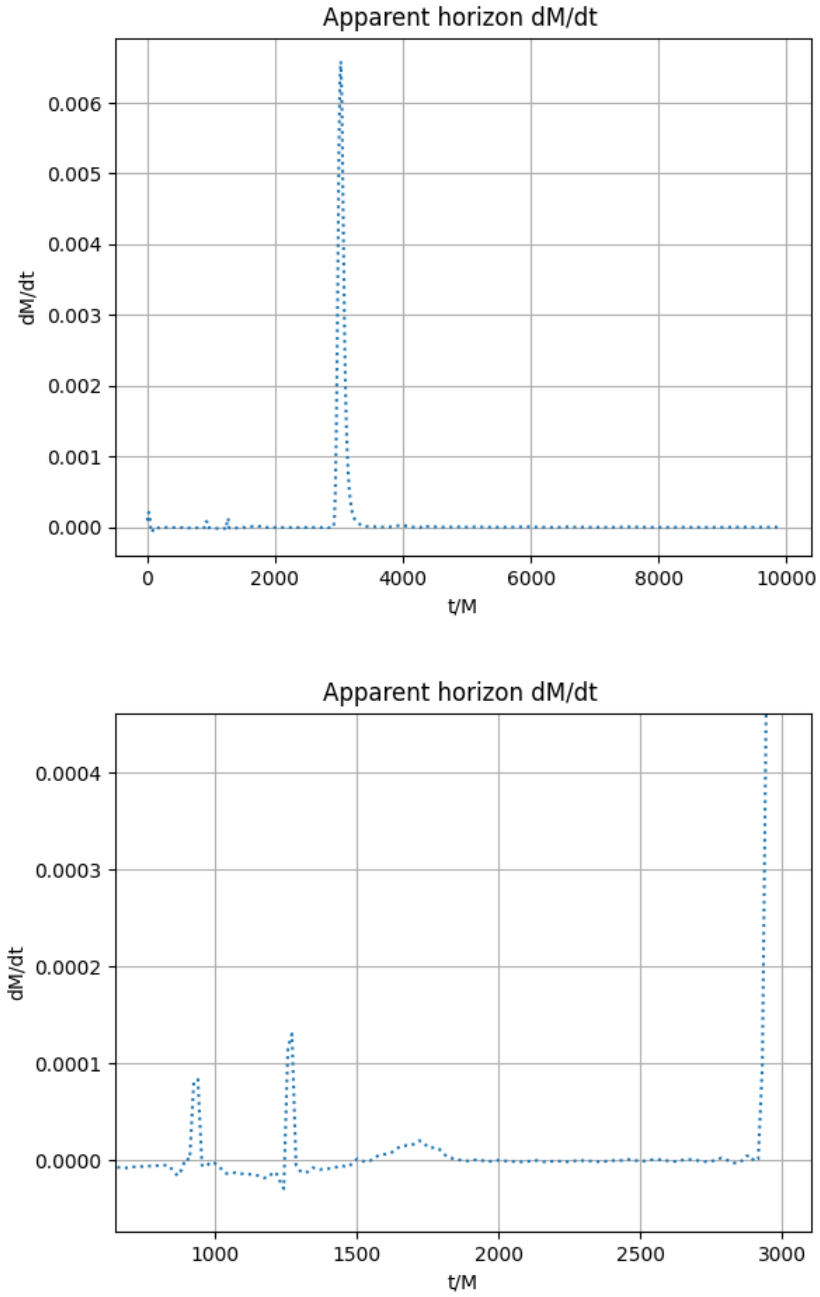

Figure 45: Time derivative of the AH's mass for a simulation with $Q = 3$, $\chi = 0.6$, $n_{mv} = 64$, $l_{max} = 6$. The tiny fluctuations visible before the coalescence (big central peak) could be adducible to energy flowing into the BH during the inspiral.

Appendices

A Acronyms and Abbreviations

AF	Asymptotically flat
AH	Apparent horizon
AMR	Adaptive mesh refinement
BBH	Binary black hole
BH	Black hole
BHNS	Black hole-neutron star
BNS	Binary neutron star
EFE	Einstein Field Equation
EM	Electromagnetic
EOS	Equation of state
GR	General Relativity
GRHD	General-relativistic hydrodynamics
GW	Gravitational-wave
ID	Initial data
ISCO	Innermost stable circular orbit
ISM	Interstellar medium
NR	Numerical Relativity
NS	Neutron star
PDE	Partial differential equation
SCDD	Schur complement domain decomposition
TOV	Tolman-Oppenheimer-Volkoff
XCTS	Extended conformal thin sandwich

B Conformal connection

Given $\tilde{\boldsymbol{\gamma}}$ a well-defined conformal metric on a Σ_t, and $\tilde{\boldsymbol{D}}$ the Levi-Civita connection associated to it, such that

$$\tilde{\boldsymbol{D}}\tilde{\boldsymbol{\gamma}} = 0 \tag{223}$$

We can define a Christoffel symbols $\tilde{\Gamma}^k{}_{ij}$ of $\tilde{\boldsymbol{D}}$, with respect to the coordintes (x^i):

$$\tilde{\Gamma}^k{}_{ij} = \frac{1}{2}\tilde{\gamma}^{kl}\left(\frac{\partial\tilde{\gamma}_{lj}}{\partial x^i} + \frac{\partial\tilde{\gamma}_{il}}{\partial x^j} - \frac{\partial\tilde{\gamma}_{ij}}{\partial x^l}\right) \tag{224}$$

Given a tensor field T of type $\binom{p}{q}$ on Σ_t, we can relate the physical and conformal covariant derivative with the formula

$$D_k T^{i_1\ldots i_p}{}_{j_1\ldots j_q} = \tilde{D}_k T^{i_1\ldots i_p}{}_{j_1\ldots j_q} + \sum_{r=1}^{p} C^{i_r}{}_{kl} T^{i_1\ldots l\ldots i_p}{}_{j_1\ldots j_q} - \sum_{r=1}^{q} C^{l}{}_{kj_r} T^{i_1\ldots i_p}{}_{j_1\ldots l\ldots j_q} \tag{225}$$

where

$$C^k_{ij} := \Gamma^k{}_{ij} - \tilde{\Gamma}^k{}_{ij} = \frac{1}{2}\gamma^{kl}(\tilde{D}_i\gamma_{lj} + \tilde{D}_j\gamma_{il} - \tilde{D}_l\gamma_{ij}) \tag{226}$$

This time $\Gamma^k{}_{ij}$ are the Christoffel symbols of the physical covariant derivative $\boldsymbol{D}$. We leave as reference appendix D of Wald (2010) for additional details on the topic of conformal transformations.

C Transformations

The majority of this project introduces results written in geometric units. However, such units system is not typically used by the astrophysics community. We introduced therefore some transformations useful to efficiently convert from geometric with $G = c = M_\odot = 1$, to cgs units with $G = 6.67 \cdot 10^{-8}$ [dyn $\cdot$ cm^2 $\cdot$ g^{-2}], $c = 2.99 \cdot 10^{10}$ [cm/s], $M_\odot = 1.99 \cdot 10^{33}$ [g].

- Length transformation:

$$d = d_{geom} \cdot \frac{GM_\odot}{c^2} \simeq d_{geom} \cdot 1.48 \cdot 10^5 \text{ [cm]} \tag{227}$$

- Time transformation:

$$t = t_{geom} \cdot \frac{GM_\odot}{c^3} \simeq t_{geom} \cdot 4.92 \cdot 10^{-6} \text{ [s]} \tag{228}$$

- Mass transformation:

$$M = M_{geom} \cdot M_\odot \simeq M_{geom} \cdot 1.99 \cdot 10^{33} \text{ [g]} \tag{229}$$

- Density transformation:

$$\rho = \rho_{geom} \cdot \frac{c^6}{M_\odot^2 G^3} \simeq \rho_{geom} \cdot 6.18 \cdot 10^{17} \text{ [g/cm}^3\text{]} \tag{230}$$

- Luminosity transformation:

$$L = L_{geom} \cdot \frac{c^5}{G} \simeq L_{geom} \cdot 3.63 \cdot 10^{59} \text{ [erg/s]} \tag{231}$$

D Padé approximant

The Padé approximants are a particular type of rational approximation. One can define a Padé of order L,M by

$$[L, M] = \frac{P_L(x)}{Q_M(x)} \tag{232}$$

with $P_L(x)$ and $Q_M(x)$ being polynomials of degree less than or equal to L and M respectively. If f(x) is the analytical function to approximate, the final expansion will be in the form

$$f(x) \approx R(x) = \frac{\sum_{i=0}^{L} a_i x^i}{1 + \sum_{j=1}^{M} b_k x^k} = \frac{a_0 + a_1 x + a_2 x^2 + a_3 x^3 \dots a_L x^L}{1 + b_1 x + b_2 x^2 + b_3 x^3 \dots b_M x^M} \tag{233}$$

If one considers the formal power series

$$f(x) = \sum_{j=0}^{\infty} f_j x^j \tag{234}$$

then, can determine the coefficient of the Padé approximant by imposing

$$f(x) - \frac{P_L(x)}{Q_M(x)} = O(x^{L+M+1}) \tag{235}$$

and finally obtain

$$f_0 = a_0 \tag{236}$$
$$f_1 + f_0 b_1 = a_1 \tag{237}$$
$$f_2 + f_1 b_1 + f_0 b_2 = a_2 \tag{238}$$
$$\vdots \tag{239}$$
$$f_L + f_{(L-1)} b_1 + \dots + f_0 b_L = a_L \tag{240}$$
$$f_{(L+1)} + f_L b_1 + \dots + f_{(L-M+1)} b_M = 0 \tag{241}$$
$$\vdots \tag{242}$$
$$f_{(L+M)} + f_{(L+M-1)} b_1 + \dots + f_L b_M = 0 \tag{243}$$

When this technique can be applied, the resulting function is unique and a formal power series of order M at the numerator and L at the denominator and corresponds to the Maclaurin series in the case of a (L,0) approximant. The real strength of this method becomes evident when approximating functions that contain poles, as the use of rational functions enables a more accurate and comprehensive description of such functions if compared to the Taylor expansion.

References

Abbott, B., Abbott, R., Abbott, T., Abernathy, M., Acernese, F., Ackley, K., Adams, C., Adams, T., Addesso, P., and et al., R. A. (2016a). Observation of gravitational waves from a binary black hole merger. *Phys. Rev. Lett.*, 116:061102.

Abbott, B., Abbott, R., Abbott, T., Abernathy, M., Acernese, F., Ackley, K., Adams, C., Adams, T., Addesso, P., and et al., R. A. (2016b). Tests of general relativity with GW150914. *Physical Review Letters*, 116(22).

Abbott, B., Abbott, R., Abbott, T., Acernese, F., Ackley, K., Adams, C., Adams, T., Addesso, P., Adhikari, R., and et al., V. A. (2017a). GW170817: Observation of gravitational waves from a binary neutron star inspiral. *Physical Review Letters*, 119(16).

Abbott, B. P., Abbott, R., Abbott, T. D., Acernese, F., Ackley, K., Adams, C., Adams, T., Addesso, P., Adhikari, R. X., and et al., V. B. A. (2017b). A gravitational-wave standard siren measurement of the hubble constant. *Nature*, 551(7678):85–88.

Abbott, B. P., Abbott, R., Abbott, T. D., Acernese, F., Ackley, K., Adams, C., Adams, T., Addesso, P., Adhikari, R. X., and et al., V. B. A. (2017c). Gravitational waves and gamma-rays from a binary neutron star merger: GW170817 and GRB 170817a. *The Astrophysical Journal*, 848(2):L13.

Abbott, R., Abbott, T. D., Abraham, S., Acernese, F., Ackley, K., Adams, A., Adams, C., and et al., R. X. A. (2021). Observation of gravitational waves from two neutron star–black hole coalescences. *The Astrophysical Journal Letters*, 915(1):L5.

Abbott, R., Abbott, T. D., Abraham, S., Acernese, F., Ackley, K., Adams, A., Adams, C., and et al., R. X. A. (2023). Population of merging compact binaries inferred using gravitational waves through gwtc-3. *Phys. Rev. X*, 13:011048.

Ajith, P., Babak, S., Chen, Y., Hewitson, M., Krishnan, B., Sintes, A. M., Whelan, J. T., Brügmann, B., Diener, P., Dorband, N., Gonzalez, J., Hannam, M., Husa, S., Pollney, D., Rezzolla, L., Santamaría, L., Sperhake, U., and Thornburg, J. (2008). Template bank for gravitational waveforms from coalescing binary black holes: Nonspinning binaries. *Phys. Rev. D*, 77:104017.

Akcay, S., Bernuzzi, S., Messina, F., Nagar, A., Ortiz, N., and Rettegno, P. (2019). Effective-one-body multipolar waveform for tidally interacting binary neutron stars up to merger. *Physical Review D*, 99(4).

Akmal, A., Pandharipande, V. R., and Ravenhall, D. G. (1998). Equation of state of nucleon matter and neutron star structure. *Phys. Rev. C*, 58:1804–1828.

Alford, M., Braby, M., Paris, M., and Reddy, S. (2005). Hybrid stars that masquerade as neutron stars. *The Astrophysical Journal*, 629(2):969–978.

Alvi, K. (2001). Energy and angular momentum flow into a black hole in a binary. *Physical Review D*, 64:104020.

Arnowitt R., Deser S., . M. C. W. (1962). Gravitation: An introduction to current research. 104(8).

Bardeen, J. M. and Petterson, J. A. (1975). The Lense-Thirring Effect and Accretion Disks around Kerr Black Holes. , 195:L65.

Bardeen, J. M., Press, W. H., and Teukolsky, S. A. (1972). Rotating Black Holes: Locally Nonrotating Frames, Energy Extraction, and Scalar Synchrotron Radiation. , 178:347–370.

Baumgarte, T. (2003). Numerical relativity and compact binaries. *Physics Reports*, 376(2):41–131.

Belczynski, K., Ryu, T., Perna, R., Berti, E., Tanaka, T. L., and Bulik, T. (2017). On the likelihood of detecting gravitational waves from Population III compact object binaries. *Monthly Notices of the Royal Astronomical Society*, 471(4):4702–4721.

Beradze, R., Gogberashvili, M., and Sakharov, A. S. (2020). Binary neutron star mergers with missing electromagnetic counterparts as manifestations of mirror world. *Physics Letters B*, 804:135402.

Berger, M. J. and Oliger, J. (1984). Adaptive mesh refinement for hyperbolic partial differential equations. *Journal of Computational Physics*, 53(3):484–512.

Bernuzzi, S. and Dietrich, T. (2016). Gravitational waveforms from binary neutron star mergers with high-order weighted-essentially-nonoscillatory schemes in numerical relativity. *Phys. Rev. D*, 94:064062.

Bernuzzi, S., Dietrich, T., Tichy, W., and Brügmann, B. (2014). Mergers of binary neutron stars with realistic spin. *Physical Review D*, 89(10).

Bernuzzi, S., Nagar, A., Dietrich, T., and Damour, T. (2015). Modeling the dynamics of tidally interacting binary neutron stars up to the merger. *Physical Review Letters*, 114(16).

Bernuzzi, S., Nagar, A., and Zenginoğ lu, A. (2011). Binary black hole coalescence in the extreme-mass-ratio limit: Testing and improving the effective-one-body multipolar waveform. *Physical Review D*, 83(6).

Bernuzzi, S., Thierfelder, M., and Brügmann, B. (2012). Accuracy of numerical relativity waveforms from binary neutron star mergers and their comparison with post-newtonian waveforms. *Phys. Rev. D*, 85:104030.

Blanchet, L. (2002). Innermost circular orbit of binary black holes at the third post-newtonian approximation. *Phys. Rev. D*, 65:124009.

Blanchet, L. (2014). Gravitational radiation from post-newtonian sources and inspiralling compact binaries. *Living Reviews in Relativity*, 17(1).

Blanchet, L. (2019). Analytic approximations in GR and gravitational waves. *International Journal of Modern Physics D*, 28(06):1930011.

Blandford, R. D. and Znajek, R. L. (1977). Electromagnetic extraction of energy from Kerr black holes. *Monthly Notices of the Royal Astronomical Society*, 179(3):433–456.

Borges, R., Carmona, M., Costa, B., and Don, W. S. (2008). An improved weighted essentially non-oscillatory scheme for hyperbolic conservation laws. *Journal of Computational Physics*, 227(6):3191–3211.

Boyd, J. (2001). *Chebyshev and Fourier Spectral Methods: Second Revised Edition*. Dover Books on Mathematics. Dover Publications.

Brandt, S. and Brügmann, B. (1997). A simple construction of initial data for multiple black holes. *Phys. Rev. Lett.*, 78:3606–3609.

Brill, D. R. and Lindquist, R. W. (1963). Interaction energy in geometrostatics. *Phys. Rev.*, 131:471–476.

Brown, D., Sarbach, O., Schnetter, E., Tiglio, M., Diener, P., Hawke, I., and Pollney, D. (2007). Excision without excision. *Physical Review D*, 76(8).

Brügmann, B., González, J. A., Hannam, M., Husa, S., Sperhake, U., and Tichy, W. (2008). Calibration of moving puncture simulations. *Physical Review D*, 77(2).

Brügmann, B., Tichy, W., and Jansen, N. (2004). Numerical simulation of orbiting black holes. *Physical Review Letters*, 92(21).

Buonanno, A. and Damour, T. (1999). Effective one-body approach to general relativistic two-body dynamics. *Physical Review D*, 59(8).

Capela, F., Pshirkov, M., and Tinyakov, P. (2013). Constraints on primordial black holes as dark matter candidates from capture by neutron stars. *Physical Review D*, 87(12).

Carrasco, F., Shibata, M., and Reula, O. (2021). Magnetospheres of black hole-neutron star binaries. *Physical Review D*, 104(6).

Chaurasia, S. V., Dietrich, T., Johnson-McDaniel, N. K., Ujevic, M., Tichy, W., and Brügmann, B. (2018). Gravitational waves and mass ejecta from binary neutron star mergers: Effect of large eccentricities. *Physical Review D*, 98(10).

Choquet-Bruhat, Y. (1971). New elliptic system and global solutions for the constraints equations in General relativity. *Communications in Mathematical Physics*, 21(3):211–218.

Cutler, C., Apostolatos, T. A., Bildsten, L., Finn, L. S., Flanagan, E. E., Kennefick, D., Markovic, D. M., Ori, A., Poisson, E., Sussman, G. J., and Thorne, K. S. (1993a). The last three minutes: Issues in gravitational-wave measurements of coalescing compact binaries. *Physical Review Letters*, 70(20):2984–2987.

Cutler, C., Finn, L. S., Poisson, E., and Sussman, G. J. (1993b). Gravitational radiation from a particle in circular orbit around a black hole. ii. numerical results for the nonrotating case. *Phys. Rev. D*, 47:1511–1518.

Damour, T. (1983). Gravitational radiation and the motion of compact bodies. In *Lecture Notes in Physics, Berlin Springer Verlag*, volume 124, pages 59–144.

Damour, T. and Nagar, A. (2009). Relativistic tidal properties of neutron stars. *Physical Review D*, 80(8).

Damour, T. and Nagar, A. (2010). Effective one body description of tidal effects in inspiralling compact binaries. *Physical Review D*, 81(8).

Darbha, S., Kasen, D., Foucart, F., and Price, D. J. (2021). Electromagnetic signatures from the tidal tail of a black hole—neutron star merger. *The Astrophysical Journal*, 915(1):69.

De, S., Finstad, D., Lattimer, J. M., Brown, D. A., Berger, E., and Biwer, C. M. (2018). Tidal deformabilities and radii of neutron stars from the observation of GW170817. *Physical Review Letters*, 121(9).

Dietrich, T., Bernuzzi, S., Ujevic, M., and Brügmann, B. (2015). Numerical relativity simulations of neutron star merger remnants using conservative mesh refinement. *Physical Review D*, 91(12).

Dietrich, T. and Ujevic, M. (2017). Modeling dynamical ejecta from binary neutron star mergers and implications for electromagnetic counterparts. *Classical and Quantum Gravity*, 34(10):105014.

Duez, M. D., Foucart, F., Kidder, L. E., Pfeiffer, H. P., Scheel, M. A., and Teukolsky, S. A. (2008). Evolving black hole-neutron star binaries in general relativity using pseudospectral and finite difference methods. *Physical Review D*, 78(10).

East, W. E., Pretorius, F., and Stephens, B. C. (2012). Eccentric black hole-neutron star mergers: Effects of black hole spin and equation of state. *Phys. Rev. D*, 85:124009.

Flanagan, É . É. and Hinderer, T. (2008). Constraining neutron-star tidal love numbers with gravitational-wave detectors. *Physical Review D*, 77(2).

Foucart, F. (2020). A brief overview of black hole-neutron star mergers. *Frontiers in Astronomy and Space Sciences*, 7.

Foucart, F., Deaton, M. B., Duez, M. D., Kidder, L. E., MacDonald, I., Ott, C. D., Pfeiffer, H. P., Scheel, M. A., Szilagyi, B., and Teukolsky, S. A. (2013). Black-hole–neutron-star mergers at realistic mass ratios: Equation of state and spin orientation effects. *Phys. Rev. D*, 87:084006.

Fragile, P. C., Blaes, O. M., Anninos, P., and Salmonson, J. D. (2007). Global general relativistic magnetohydrodynamic simulation of a tilted black hole accretion disk. *The Astrophysical Journal*, 668(1):417–429.

Gó mez, R., Lehner, L., Papadopoulos, P., and Winicour, J. (1997). The eth formalism in numerical relativity. *Classical and Quantum Gravity*, 14(4):977–990.

Gonzalez, A., Gamba, R., Breschi, M., Zappa, F., Carullo, G., Bernuzzi, S., and Nagar, A. (2023a). Numerical-relativity-informed effective-one-body model for black-hole–neutron-star mergers with higher modes and spin precession. *Physical Review D*, 107(8).

Gonzalez, A., Zappa, F., Breschi, M., Bernuzzi, S., Radice, D., Adhikari, A., Camilletti, A., Vivekanandji Chaurasia, S., Doulis, G., Padamata, S., Rashti, A., Ujevic, M., Brügmann, B., Cook, W., Dietrich, T., Perego, A., Poudel, A., and Tichy, W. (2023b). Second release of the core database of binary neutron star merger waveforms. *Classical and Quantum Gravity*, 40(8):085011.

Gourgoulhon, E. (2007). 3+1 formalism and bases of numerical relativity.

Harada, T. (2001). Reconstructing the equation of state for cold nuclear matter from the relationship of any two properties of neutron stars. *Physical Review C*, 64(4).

Hawking, S. W. and Ellis, G. F. R. (1973). *The Large Scale Structure of Space-Time*. Cambridge Monographs on Mathematical Physics. Cambridge University Press.

Hayashi, K., Kawaguchi, K., Kiuchi, K., Kyutoku, K., and Shibata, M. (2021). Properties of the remnant disk and the dynamical ejecta produced in low-mass black hole-neutron star mergers. *Physical Review D*, 103(4).

Henry, Q., Faye, G., and Blanchet, L. (2020). Tidal effects in the equations of motion of compact binary systems to next-to-next-to-leading post-newtonian order. *Physical Review D*, 101(6).

Higginbotham, K., Khamesra, B., McInerney, J. P., Jani, K., Shoemaker, D. M., and Laguna, P. (2019). Coping with spurious radiation in binary black hole simulations. *Physical Review D*, 100(8).

Hinderer, T., Lackey, B. D., Lang, R. N., and Read, J. S. (2010). Tidal deformability of neutron stars with realistic equations of state and their gravitational wave signatures in binary inspiral. *Physical Review D*, 81(12).

Jackson, J. D. (1975). *Classical electrodynamics*. Wiley, New York, NY, second edition.

Kawaguchi, K., Kyutoku, K., Nakano, H., Okawa, H., Shibata, M., and Taniguchi, K. (2015). Black hole-neutron star binary merger: Dependence on black hole spin orientation and equation of state. *Physical Review D*, 92(2).

Kidder, L. E. (1995). Coalescing binary systems of compact objects to $(\text{post})^{5/2}$-newtonian order. v. spin effects. *Phys. Rev. D*, 52:821–847.

Kyutoku, K., Shibata, M., and Taniguchi, K. (2010). Gravitational waves from non-spinning black hole-neutron star binaries: Dependence on equations of state. *Physical Review D*, 82(4).

Kyutoku, K., Shibata, M., and Taniguchi, K. (2021). Coalescence of black hole–neutron star binaries. *Living Reviews in Relativity*, 24(1).

Lattimer, J. M. and Schramm, D. N. (1974). Black-Hole-Neutron-Star Collisions. , 192:L145.

Levan, A., Gompertz, B., Salafia, O., Bulla, M., Burns, E., Hotokezaka, K., Izzo, L., Lamb, G., Malesani, D., Oates, S., Ravasio, M., Escorial, A., Schneider, B., Sarin, N., Schulze, S., Tanvir, N., Ackley, K., Anderson, G., Brammer, G., and Kann, D. (2023). Heavy element production in a compact object merger observed by jwst. *Nature*.

Li, L.-X. and Paczyński, B. (1998). Transient events from neutron star mergers. *The Astrophysical Journal*, 507(1):L59–L62.

Lichnerowicz, A. (1944). L'intégration des equations de la gravitation relativiste et le problème des n corps. *J. Math. Pures Appl*, 23(37).

Lichnerowicz, A. (1952). Sur les équations relativistes de la gravitation. *Bulletin de la Société Mathématique de France*, 80:237–251.

Lousto, C. O., Nakano, H., Zlochower, Y., and Campanelli, M. (2010). Intermediate-mass-ratio black hole binaries: Intertwining numerical and perturbative techniques. *Physical Review D*, 82(10).

Maggiore, M. (2008). *Gravitational Waves: Volume 1: Theory and Experiments*. Gravitational Waves. OUP Oxford.

Martí, J. M. and Müller, E. (1999). Numerical hydrodynamics in special relativity. *Living Reviews in Relativity*, 2(1).

Mashonkina, L., Christlieb, N., and Eriksson, K. (2014). The hamburg/eso r-process enhanced star survey (heres) - x. he 2252-4225, one more r-process enhanced and actinide-boost halo star. *A&A*, 569:A43.

McKinney, J. C., Tchekhovskoy, A., and Blandford, R. D. (2013). Alignment of magnetized accretion disks and relativistic jets with spinning black holes. *Science*, 339(6115):49–52.

Misner, C., Thorne, K., Wheeler, J., and Kaiser, D. (2017). *Gravitation*. Princeton University Press.

Mochkovitch, R., Hernanz, M., Isern, J., and Martin, X. (1993). Gamma-ray bursts as collimated jets from neutron star/black hole mergers. , 361(6409):236–238.

Nagar, A., Bernuzzi, S., Pozzo, W. D., Riemenschneider, G., Akcay, S., Carullo, G., Fleig, P., Babak, S., Tsang, K. W., Colleoni, M., Messina, F., Pratten, G., Radice, D., Rettegno, P., Agathos, M., Fauchon-Jones, E., Hannam, M., Husa, S., Dietrich, T., Cerdá -Duran, P., Font, J. A., Pannarale, F., Schmidt, P., and Damour, T. (2018). Time-domain effective-one-body gravitational waveforms for coalescing compact binaries with nonprecessing spins, tides, and self-spin effects. *Physical Review D*, 98(10).

Nagar, A., Healy, J., Lousto, C. O., Bernuzzi, S., and Albertini, A. (2022). Numerical-relativity validation of effective-one-body waveforms in the intermediate-mass-ratio regime. *Physical Review D*, 105(12).

O'Leary, R. M., Kocsis, B., and Loeb, A. (2009). Gravitational waves from scattering of stellar-mass black holes in galactic nuclei. *Monthly Notices of the Royal Astronomical Society*, 395(4):2127–2146.

Özel, F., Psaltis, D., Narayan, R., and McClintock, J. E. (2010). The Black Hole Mass Distribution in the Galaxy. , 725(2):1918–1927.

Özel, F., Psaltis, D., Narayan, R., and Santos Villarreal, A. (2012). On the Mass Distribution and Birth Masses of Neutron Stars. , 757(1):55.

Papenfort, L. J., Tootle, S. D., Grandclé ment, P., Most, E. R., and Rezzolla, L. (2021). New public code for initial data of unequal-mass, spinning compact-object binaries. *Physical Review D*, 104(2).

Peters, P. C. (1964). Gravitational radiation and the motion of two point masses. *Phys. Rev.*, 136:B1224–B1232.

Peters, P. C. and Mathews, J. (1963). Gravitational Radiation from Point Masses in a Keplerian Orbit. *Physical Review*, 131(1):435–440.

Pfeiffer, H. P. and York, J. W. (2003). Extrinsic curvature and the einstein constraints. *Phys. Rev. D*, 67:044022.

Poisson, E. and Will, C. M. (1995). Gravitational waves from inspiraling compact binaries: Parameter estimation using second-post-newtonian waveforms. *Physical Review D*, 52(2):848–855.

Radice, D., Galeazzi, F., Lippuner, J., Roberts, L. F., Ott, C. D., and Rezzolla, L. (2016). Dynamical mass ejection from binary neutron star mergers. *Monthly Notices of the Royal Astronomical Society*, 460(3):3255–3271.

Rashti, A., Fabbri, F. M., Brügmann, B., Chaurasia, S. V., Dietrich, T., Ujevic, M., and Tichy, W. (2022). New pseudospectral code for the construction of initial data. *Physical Review D*, 105(10).

Read, J. S., Lackey, B. D., Owen, B. J., and Friedman, J. L. (2009). Constraints on a phenomenologically parametrized neutron-star equation of state. *Phys. Rev. D*, 79:124032.

Rees, M. J. and Mészáros, P. (1992). Relativistic fireballs: energy conversion and time-scales. *Monthly Notices of the Royal Astronomical Society*, 258(1):41P–43P.

Reisswig, C. and Pollney, D. (2011). Notes on the integration of numerical relativity waveforms. *Classical and Quantum Gravity*, 28(19):195015.

Rezzolla, L. and Zanotti, O. (2013). *Relativistic Hydrodynamics*. Oxford University Press.

Riemenschneider, G., Rettegno, P., Breschi, M., Albertini, A., Gamba, R., Bernuzzi, S., and Nagar, A. (2021). Teobresums: assessment of consistent next-to-quasicircular corrections and post-adiabatic approximation in multipolar binary black holes waveforms.

Saad, Y. (2003). *Iterative Methods for Sparse Linear Systems*. Society for Industrial and Applied Mathematics, second edition.

Santoliquido, F., Mapelli, M., Giacobbo, N., Bouffanais, Y., and Artale, M. C. (2021). The cosmic merger rate density of compact objects: impact of star formation, metallicity, initial mass function, and binary evolution. *Monthly Notices of the Royal Astronomical Society*, 502(4):4877–4889.

Schoen, R. and Yau, S.-T. (1979). Positivity of the total mass of a general space-time. *Phys. Rev. Lett.*, 43:1457–1459.

Schoen, R. and Yau, S.-T. (1981). Proof of the positive mass theorem. ii. *Communications in Mathematical Physics*, 79:231,260.

Shibata, M. and Nakamura, T. (1995). Evolution of three-dimensional gravitational waves: Harmonic slicing case. *Phys. Rev. D*, 52:5428–5444.

Smarr, L. L. and Blandford, R. (1976). The binary pulsar: physical processes, possible companions, and evolutionary histories. , 207:574–588.

Staff, J. E., Jaikumar, P., Chan, V., and Ouyed, R. (2012). Spindown of isolated neutron stars: Gravitational waves or magnetic braking? *The Astrophysical Journal*, 751(1):24.

Takami, H., Kyutoku, K., and Ioka, K. (2014). High-energy radiation from remnants of neutron star binary mergers. *Phys. Rev. D*, 89:063006.

Thierfelder, M., Bernuzzi, S., and Brügmann, B. (2011). Numerical relativity simulations of binary neutron stars. *Physical Review D*, 84(4).

Thorne, K. S. (1980). Multipole expansions of gravitational radiation. *Rev. Mod. Phys.*, 52:299–339.

Tichy, W., Rashti, A., Dietrich, T., Dudi, R., and Brügmann, B. (2019). Constructing binary neutron star initial data with high spins, high compactnesses, and high mass ratios. *Physical Review D*, 100(12).

Tsang, D., Read, J. S., Hinderer, T., Piro, A. L., and Bondarescu, R. (2012). Resonant shattering of neutron star crusts. *Physical Review Letters*, 108(1).

Uryū, K. b. o. and Tsokaros, A. (2012). New code for equilibriums and quasiequilibrium initial data of compact objects. *Phys. Rev. D*, 85:064014.

Wald, R. (2010). *General Relativity*. University of Chicago Press.

Watson, D., Hansen, C. J., Selsing, J., Koch, A., Malesani, D. B., Andersen, A. C., Fynbo, J. P. U., Arcones, A., Bauswein, A., Covino, S., Grado, A., Heintz, K. E., Hunt, L., Kouveliotou, C., Leloudas, G., Levan, A. J., Mazzali, P., and Pian, E. (2019). Identification of strontium in the merger of two neutron stars. *Nature*, 574(7779):497–500.

Ye, C. S., fai Fong, W., Kremer, K., Rodriguez, C. L., Chatterjee, S., Fragione, G., and Rasio, F. A. (2019). On the rate of neutron star binary mergers from globular clusters. *The Astrophysical Journal*, 888(1):L10.

York, J. W., J. (1979). Kinematics and dynamics of general relativity. In Smarr, L. L., editor, *Sources of Gravitational Radiation*, pages 83–126.

York, J. W. (1999). Conformal "thin-sandwich" data for the initial-value problem of general relativity. *Phys. Rev. Lett.*, 82:1350–1353.

Yunes, N., Yagi, K., and Pretorius, F. (2016). Theoretical physics implications of the binary black-hole mergers GW150914 and GW151226. *Physical Review D*, 94(8).

Zanna, L. D. and Bucciantini, N. (2002). An efficient shock-capturing central-type scheme for multidimensional relativistic flows. *Astronomy &amp Astrophysics*, 390(3):1177–1186.

Zappa, F., Bernuzzi, S., Pannarale, F., Mapelli, M., and Giacobbo, N. (2019). Black-hole remnants from black-hole–neutron-star mergers. *Physical Review Letters*, 123(4).

Zhang, B. (2019). Charged compact binary coalescence signal and electromagnetic counterpart of plunging black hole–neutron star mergers. *The Astrophysical Journal*, 873(2):L9.

Zwart, S. F. P. and McMillan, S. L. W. (1999). Black hole mergers in the universe. *The Astrophysical Journal*, 528(1):L17.